

LOCALIZATION OF BILIARY TREE STRUCTURES  
BY USE OF PHOTON DIFFUSION MODELS

by

DHARMENDRA NADKAR

Presented to the Faculty of the Graduate School of  
The University of Texas at Arlington in Partial Fulfillment  
of the Requirements  
for the Degree of

MASTER OF SCIENCE IN BIOMEDICAL ENGINEERING

THE UNIVERSITY OF TEXAS AT ARLINGTON

DECEMBER 2007

Copyright © by Dharmendra Nadkar 2007

All Rights Reserved

## ACKNOWLEDGEMENTS

I would like to take this opportunity to express my sincere gratitude to all those people who have helped me throughout my thesis work.

First, I would like to thank my mentor Dr. George Alexandrakis, who continually and convincingly conveyed a spirit of adventure with regards to research in me. He has always been there to encourage and help me during research oriented challenges. It is because of him that I got an opportunity to work on such an exciting problem. Also, I would like to thank him for his assistance in the preparation of this thesis.

I would also like to thank Dr. Edward Livingston, MD, Chairman of GI/Endocrine Surgery at UTSW Medical Center for helping me understand better the problems faced during surgery and also for giving me valuable input during our meetings, which eventually helped me refine my work.

My special thanks are also due to Dr. Hanli Liu, Professor, Dept. of Bioengineering, UTA for her valuable input. I have learnt a lot of skills from her.

I would also like to thank UTA for giving me such a challenging, supportive and technical environment. I owe you a lot.

Finally, I am greatly indebted to my parents, Laxmi and Shantaram Nadkar without whose prayers and well wishes this work would not have shaped in a way as it stands today. For me they are an institution of love and inspiration.

NOVEMBER 21, 2007

## ABSTRACT

### LOCALIZATION OF BILIARY TREE STRUCTURES BY USE OF PHOTON DIFFUSION MODELS

Publication No. \_\_\_\_\_

Dharmendra Nadkar, M.S.  
The University of Texas at Arlington, 2007

Supervising Professor: Dr. George Alexandrakis

A novel computational methodology is proposed for the intraoperative localization of biliary tree structures by means of spectrally resolved near-infrared reflectance measurements. As these structures are embedded in fatty tissue, they cannot be visualized directly, which results in inadvertent injuries during a cholecystectomy operation. Localizing the biliary tree intraoperatively is therefore an important clinical problem. Successful clinical implementation of an imaging system which could attain this goal would reduce surgical time, improve patient safety, and minimize the risk of complications and expenses attributable to the current standard practice of intraoperative cholangiography. It is hoped that the work presented here will contribute to the attainment of this important clinical goal: We describe novel computational approaches that could be applied on existing spectrally resolved reflectance data to estimate the

location, both on the fatty tissue surface and depth-wise, of blood vessels and of the bile duct. The proposed localization methods have been tested and validated in simulation. The next step is to further test them in the lab and in the operating theater

## TABLE OF CONTENTS

|   |       |
|---|-------|
| ACKNOWLEDGEMENTS.....   | iii   |
| ABSTRACT .....  | iv    |
| LIST OF ILLUSTRATIONS.....  | ix    |
| LIST OF TABLES.....   | xviii |
| CHAPTER   |       |
| 1.INTRODUCTION .....  | 1     |
| 1.1 Biliary Tree Anatomy .....  | 1     |
| 1.2 Disorders of the Biliary Tree Structure.....  | 1     |
| 1.3 Complications Resulting from Cholecystectomy Procedures.....                            | 2     |
| 1.4 Clinical Imaging Modalities Currently in Use<br>During Cholecystectomy .....            | 3     |
| 1.5 Purpose of this Work: Use of Optical Imaging to<br>Improve Cholecystectomy Outcome..... | 4     |
| 2.METHODS .....   | 6     |
| 2.1 The Reflectance Probe Geometry .....  | 6     |
| 2.2 Tissue Geometry (Patient-Based and its Simplification<br>for the Simulations).....      | 7     |
| 2.3 Proposed Method for the Localization of Biliary Tree Structures.....                    | 8     |
| 2.3.1 Localization of Biliary Tree Structure on the<br>Fatty Tissue Surface.....            | 8     |
| 2.3.2 Tissue Depth Estimation of Biliary Tree Structures .....                              | 10    |

|   |    |
|---|----|
| 2.4 Tissue Optical Properties .....   | 11 |
| 2.5 Monte Carlo Simulation.....   | 13 |
| 2.6 Semi-Infinite, Spectrally Resolved Diffusion Model .....  | 15 |
| 2.7 Two-Layer, Spectrally Resolved Diffusion Model.....   | 16 |
| 2.7.1 Diffusion Equation (Forward Model) .....  | 16 |
| 2.7.2 Inverse Model .....   | 18 |
| 3.RESULTS AND ANALYSIS .....  | 21 |
| 3.1 Lateral Localization of Absorption Heterogeneities.....   | 22 |
| 3.1.1 Lateral Localization of a Single Absorbing<br>Heterogeneity (Artery).....   | 22 |
| 3.1.2 Lateral Localization of a Single Absorbing<br>Heterogeneity (Bile Duct).....  | 27 |
| 3.1.3 Lateral Localization of Two Absorbing Heterogeneities<br>(Artery and Bile Duct) Separated by<br>7 mm (Center-to-Center).....                          | 30 |
| 3.1.4 Lateral Localization of Two Absorbing Heterogeneities<br>(Artery and Bile Duct) Adjacent to Each Other.....   | 35 |
| 3.1.5 Lateral Localization of Two Absorbing Heterogeneities<br>Adjacent to Each Other (Artery and Bile Duct) in the<br>Presence of an Underlying Vein ..... | 40 |
| 3.2 Depth Localization of Absorbing Heterogeneities .....   | 46 |
| 3.2.1 Depth Localization of a Single Absorbing<br>Heterogeneity (Artery).....   | 46 |
| 3.2.2 Depth Localization of a Single Absorbing<br>Heterogeneity (Bile Duct).....  | 47 |

|   |    |
|---|----|
| 3.2.3 Depth Localization of Two Absorbing Heterogeneities<br>(Artery and Bile Duct) Separated by<br>7 mm (Center -to -Center).....                        | 48 |
| 3.2.4 Depth Localization of Two Absorbing Heterogeneities<br>(Artery and Bile Duct) Adjacent to Each Other.....   | 50 |
| 3.2.5 Depth Localization of Two Absorbing Heterogeneities<br>Adjacent to Each Other (Artery and Bile Duct) in the<br>presence of an Underlying Vein ..... | 52 |
| 3.2.6 Comparison of Depth-Wise Apparent Absorption of<br>Heterogeneities (Artery and Bile Duct) .....   | 54 |
| 3.3 Analysis of Depth versus Change in Apparent Absorption .....  | 55 |
| 3.3.1 Lateral Localization .....  | 55 |
| 3.3.2 Depth Localization.....   | 61 |
| 3.4 Effect of Background Scattering Value Errors on<br>Apparent Absorption.....   | 63 |
| 4.DISCUSSION AND CONCLUSIONS .....  | 65 |
| APPENDIX .....  | 69 |
| A.The Levenberg –Marquardt Fitting Algorithm.....   | 70 |
| REFERENCES .....  | 73 |
| BIOGRAPHICAL INFORMATION.....   | 76 |



## LIST OF ILLUSTRATIONS

| Figure   | Page |
|--|------|
| 1: Biliary tree anatomy.....   | 1    |
| 2: (a) Simulated probe geometry positioning on the tissue surface,<br>(b) Each fiber is bifurcated and can act both as a light source<br>(highlighted in red) and a detector. ....   | 6    |
| 3: (a) Patient-based geometry of the biliary tree. The geometrical plane<br>containing the probe intersects the biliary tree at right angles<br>(b) Simplified tissue geometry for the simulation. The red color<br>circle represents a cross-section of the artery, the green color<br>circle that of the bile duct and the blue circle that of the vein..... | 7    |
| 4: (a) The two-point probability density function attains highest values<br>in a tissue volume, connecting source and detector that is shaped<br>as a ‘banana’. (b) Lateral source-detector displacement results in<br>a displacement of the ‘banana’, i.e. of the tissue volume being probed .....  | 9    |
| 5 : Pictorial representation of the depth-localization strategy for an<br>absorption heterogeneity; the top layer thickness (a) touches the<br>top side of the artery, and (b) crosses through its center. ....  | 10   |
| 6: Plot of the transport scattering coefficient spectra for the tissue types<br>considered in this computational work. ....  | 13   |
| 7: Plot of the absorption coefficient spectra for the tissue types<br>considered in this computational work.. ....   | 13   |
| 8: Location of absorbing heterogeneities in the simulated tissue geometry. ....  | 21   |
| 9: Spectrally resolved reflectance from fatty tissue containing a single<br>absorbing heterogeneity with optical properties of 96% oxygenated<br>(arterial) blood, centered at -3.5 mm. Tissue optical properties are<br>plotted in figures 6 and 7. ....  | 22   |

|   |    |
|---|----|
| 10: Plot of spectrally resolved arterial $\mu_{a\_app}$ for fatty tissue containing a single absorbing heterogeneity (artery). The reflectance contribution from all 13 sources was added to each detector and the fit used absolute reflectance data. ....   | 23 |
| 11: Plot of spectrally resolved arterial $\mu_{a\_app}$ for fatty tissue containing a single absorbing heterogeneity (artery). The reflectance contribution from all 13 sources was added to each detector and the fit uses relative reflectance data. ....   | 24 |
| 12: Comparison of the reflectance from fatty tissue containing a single absorbing heterogeneity with optical properties of 96% oxygenated (arterial) blood, centered at -3.5 mm (dotted line) and without absorbing heterogeneity (solid line). Tissue optical properties are plotted in figures 6 and 7..... | 25 |
| 13: Plot of spectrally resolved arterial $\mu_{a\_app}$ for fatty tissue containing a single absorbing heterogeneity (artery). The reflectance contribution from only one source-detector pair at 3.5 mm separation was considered and the fit used absolute reflectance data. ....                           | 26 |
| 14: Plot of spectrally resolved arterial $\mu_{a\_app}$ for fatty tissue containing a single absorbing heterogeneity (artery). The reflectance contribution from only one source-detector pair at 7 mm separation was considered and the fit used absolute reflectance data. ....                             | 26 |
| 15: Spectrally resolved reflectance from fatty tissue containing a single absorbing heterogeneity having the optical properties of human bile, centered at 3.5 mm. Tissue optical properties are plotted in figures 6 and 7.....  | 27 |
| 16: Plot of spectrally resolved bile $\mu_{a\_app}$ for fatty tissue containing a single absorbing heterogeneity (bile duct). The reflectance contribution from all 13 sources was added to each detector and the fit used absolute reflectance data. ....  | 28 |
| 17: Plot of spectrally resolved bile $\mu_{a\_app}$ for fatty tissue containing a single absorbing heterogeneity (bile duct). The reflectance contribution from only one source-detector pair at a 3.5 mm separation was considered and the fit used absolute reflectance data. ....                          | 29 |
| 18: Plot of spectrally resolved bile $\mu_{a\_app}$ for fatty tissue containing a single absorbing heterogeneity (bile duct). The reflectance contribution from only one source-detector pair of 7 mm separation was considered and the fit used absolute reflectance data. ....                              | 29 |

|  |    |
|--|----|
| 19: Spectrally resolved reflectance from fatty tissue containing two absorbing heterogeneities with optical properties of arterial blood and bile, centered at -3.5 mm and 3.5 mm respectively. Tissue optical properties are plotted in figures 6 and 7.....  | 30 |
| 20: Plot of spectrally resolved arterial $\mu_{a\_app}$ for fatty tissue containing two absorbing heterogeneities (artery and bile duct) separated by a center-to-center distance of 7 mm. The reflectance contribution from all 13 sources was added to each detector and the fit uses absolute reflectance data. Both the arterial and bile absorption coefficients were varied in each fit simultaneously.....                          | 31 |
| 21: Plot of spectrally resolved bile $\mu_{a\_app}$ for fatty tissue containing two absorbing heterogeneities (artery and bile duct) separated by a center-to-center distance of 7 mm. The reflectance contribution from all 13 sources was added to each detector and the fit used absolute reflectance data. Both the arterial and bile absorption coefficients were varied in each fit simultaneously.....                              | 31 |
| 22: Plot of spectrally resolved arterial $\mu_{a\_app}$ for fatty tissue containing two absorbing heterogeneities (artery and bile duct) separated by a center-to-center distance of 7 mm. The reflectance contribution from only one source-detector pair at 3.5 mm separation was considered and the fit used absolute reflectance data. Both the arterial and bile absorption coefficients were varied in each fit simultaneously. .... | 32 |
| 23: Plot of spectrally resolved bile $\mu_{a\_app}$ for fatty tissue containing two absorbing heterogeneities (artery and bile duct) separated by a center-to-center distance of 7 mm. The reflectance contribution from only one source-detector pair at 3.5 mm separation was considered and the fit used absolute reflectance data. Both the arterial and bile absorption coefficients were varied in each fit simultaneously. ....     | 33 |
| 24: Plot of spectrally resolved arterial $\mu_{a\_app}$ for fatty tissue containing two absorbing heterogeneities (Artery and Bile) separated by a center-to-center distance of 7 mm. The reflectance contribution from only one source-detector pair at 7 mm separation was considered and the fit used absolute reflectance data. Both the arterial and bile absorption coefficients were varied in each fit simultaneously. ....        | 34 |

|  |    |
|--|----|
| 25: Plot of spectrally resolved bile $\mu_{a\_app}$ for fatty tissue containing two absorbing heterogeneities (artery and bile duct) separated by a center-to-center distance of 7 mm. The reflectance contribution from only one source-detector pair of 7 mm separation was considered and the fit used absolute reflectance data. Both the arterial and bile absorption coefficients were varied in each fit simultaneously. .... | 35 |
| 26: Spectrally resolved reflectance from fatty tissue containing two absorbing heterogeneities with optical properties of arterial blood and human bile, centered at -1 mm and 2 mm respectively. Tissue optical properties are plotted in figures 6 and 7. ....   | 36 |
| 27: Plot of spectrally resolved arterial $\mu_{a\_app}$ for fatty tissue containing two absorbing heterogeneities (artery and bile duct) adjacent to each other. The reflectance contribution from all 13 sources was added to each detector and the fit used absolute reflectance data. Both the arterial and bile absorption coefficients were varied in each fit simultaneously. ....   | 36 |
| 28: Plot of spectrally resolved bile $\mu_{a\_app}$ for fatty tissue containing two absorbing heterogeneities (artery and bile duct) placed adjacent to each other. The reflectance contribution from all 13 sources was added to each detector and the fit used absolute reflectance data. Both the arterial and bile absorption coefficients were varied in each fit simultaneously. ....  | 37 |
| 29: Plot of spectrally resolved arterial $\mu_{a\_app}$ for fatty tissue containing two absorbing heterogeneities (artery and bile duct) placed adjacent to each other. The reflectance contribution from only one source-detector pair at 3.5 mm separation was considered and the fit used absolute reflectance data. Both the arterial and bile absorption coefficients were varied in each fit simultaneously. ....              | 38 |
| 30: Plot of spectrally resolved bile $\mu_{a\_app}$ for fatty tissue containing two absorbing heterogeneities (artery and bile duct) placed adjacent to each other. The reflectance contribution from only one source-detector pair at 3.5 mm separation was considered and the fit used absolute reflectance data. Both the arterial and bile absorption coefficients were varied in each fit simultaneously. ....                  | 39 |
| 31: Plot of spectrally resolved arterial $\mu_{a\_app}$ for fatty tissue containing two absorbing heterogeneities (artery and bile duct) placed adjacent to each other. The reflectance contribution from only one source-   |    |

|   |    |
|---|----|
| detector pair of 7 mm separation was considered and the fit used absolute reflectance data. Both the arterial and bile absorption coefficients were varied in each fit simultaneously.....  | 39 |
| 32: Plot of spectrally resolved bile $\mu_{a\_app}$ for fatty tissue containing two absorbing heterogeneities (artery and bile duct) placed adjacent to each other. The reflectance contribution from only one source-detector pair at a 7 mm separation was considered and the fit used absolute reflectance data. Both the arterial and bile absorption coefficients were varied in each fit simultaneously.....  | 40 |
| 33: Location of three absorbing heterogeneities in the simulated tissue geometry. ....  | 41 |
| 34: Spectrally resolved reflectance from fatty tissue containing three absorbing heterogeneities with optical properties of arterial blood, human bile venous blood. Tissue optical properties are plotted in figures 6 and 7.....  | 42 |
| 35: Plot of spectrally resolved arterial $\mu_{a\_app}$ for fatty tissue containing three absorbing heterogeneities. Two absorbing heterogeneities (artery and bile duct) are adjacent to each other and the third one (vein) was placed immediately beneath the bile duct. The reflectance contributions from all 13 sources were added to each detector and the fit used absolute reflectance data. Both the arterial and bile absorption coefficients were varied in each fit simultaneously.....                        | 42 |
| 36: Plot of spectrally resolved bile $\mu_{a\_app}$ for fatty tissue containing three absorbing heterogeneities. Two absorbing heterogeneities (artery and bile duct) are adjacent to each other and the third one (vein) was placed immediately beneath the bile duct. The reflectance contributions from all 13 sources were added to each detector and the fit used absolute reflectance data. Both the arterial and bile absorption coefficients were varied in each fit simultaneously.....                            | 43 |
| 37: Plot of spectrally resolved arterial $\mu_{a\_app}$ for fatty tissue containing three absorbing heterogeneities. Two absorbing heterogeneities (artery and bile duct) are adjacent to each other and the third one (vein) was placed immediately beneath the bile duct. The reflectance contribution from only one source-detector pair at 3.5 mm separation was considered and the fit used absolute reflectance data. Both the arterial and bile absorption coefficients were varied in each fit simultaneously. .... | 44 |

|   |    |
|---|----|
| 38: Plot of spectrally resolved bile $\mu_{a\_app}$ for fatty tissue containing three absorbing heterogeneities. Two absorbing heterogeneities (artery and bile duct) are adjacent to each other and the third one (vein) was placed immediately beneath the bile duct. The reflectance contribution from only one source-detector pair at 3.5 mm separation was considered and the fit used absolute reflectance data. Both the arterial and bile absorption coefficients were varied in each fit simultaneously. .... | 44 |
| 39: Plot of spectrally resolved arterial $\mu_{a\_app}$ for fatty tissue containing three absorbing heterogeneities. Two absorbing heterogeneities (artery and bile duct) are adjacent to each other and the third one (vein) was placed immediately beneath the bile duct. The reflectance contribution from only one source-detector pair at 7 mm separation was considered and the fit used absolute reflectance data. ....  | 45 |
| 40: Plot of spectrally resolved bile $\mu_{a\_app}$ for fatty tissue containing three absorbing heterogeneities. Two absorbing heterogeneities (artery and bile duct) are adjacent to each other and the third one (vein) was placed immediately beneath the bile duct. The reflectance contribution from only one source-detector pair at 7 mm separation was considered and the fit used absolute reflectance data. ....  | 45 |
| 41: Depth-wise arterial $\mu_{a\_app}$ for a detector placed on the peak absorption surface location. Tissue geometry consisted of a single absorbing heterogeneity (artery centered at 4 mm depth); all sources were added to a single detector, reflectance data fitting was relative; only the arterial absorption of the top and bottom layers was varied in each fit. ....   | 46 |
| 42: Depth-wise bile $\mu_{a\_app}$ for a detector placed on the peak absorption surface location. Tissue geometry consisted of two absorbing heterogeneities (bile duct centered at 4 mm depth); all sources were added to a single detector, reflectance data fitting was relative; only the arterial absorption of the top and bottom layers was varied in each fit. ....   | 48 |
| 43: Depth-wise arterial $\mu_{a\_app}$ for a detector placed on the peak absorption surface location. Tissue geometry consisted of two absorbing heterogeneities (artery and bile duct both centered at 4 mm depth, center-to-center distance 7 mm); all sources were added to a single detector, reflectance data fitting was relative; only the arterial absorption of the top and bottom layers was varied in each fit. ....   | 49 |

|  |    |
|--|----|
| 44: Depth-wise bile $\mu_{a\_app}$ for a detector placed on the peak absorption surface location. Tissue geometry consisted of two absorbing heterogeneities (artery and bile duct both centered at 4 mm depth, center-to-center distance 7 mm); all sources were added to a single detector, reflectance data fitting was relative; only the arterial absorption of the top and bottom layers was varied in each fit.....   | 50 |
| 45: Depth-wise arterial $\mu_{a\_app}$ for a detector placed on the peak absorption surface location. Tissue geometry consisted of two absorbing heterogeneities (artery and bile duct both centered at 4 mm depth, adjacent to each other, center-to-center distance 3 mm); all sources were added to a single detector, reflectance data fitting was relative; only the arterial absorption of the top and bottom layers was varied in each fit.....                                   | 51 |
| 46: Depth-wise bile $\mu_{a\_app}$ for a detector placed on the peak absorption surface location. Tissue geometry consisted of two absorbing heterogeneities (artery and bile duct both centered at 4 mm depth, adjacent to each other); all sources were added to a single detector, reflectance data fitting was relative; only the arterial absorption of the top and bottom layers was varied in each fit.....   | 51 |
| 47: Depth-wise arterial $\mu_{a\_app}$ for a detector placed on the peak absorption surface location. Tissue geometry consisted of three absorbing heterogeneities (artery and bile duct both centered at 4 mm depth, adjacent to each other. The vein is centered at 8 mm and placed beneath the bile duct); all sources were added to a single detector, reflectance data fitting was relative; only the arterial absorption of the top and bottom layers was varied in each fit. .... | 52 |
| 48: Depth-wise bile $\mu_{a\_app}$ for a detector placed on the peak absorption surface location. Tissue geometry consisted of three absorbing heterogeneities (artery and bile duct both centered at 4 mm depth, adjacent to each other. The vein is centered at 8 mm and placed beneath bile duct); all sources were added to a single detector, reflectance data fitting was relative; only the arterial absorption of the top and bottom layers was varied in each fit. ....         | 53 |
| 49: Comparison of dept-wise arterial and bile $\mu_{a\_app}$ . In contrast to all other simulations artery and bile duct had the same size (2 mm diameter) so that the only difference is the absorption spectrum of the heterogeneity. Arterial $\mu_{a\_app}$ was scaled by factor of 5 for easier comparison.....   | 54 |

|  |    |
|--|----|
| 50: Plot of spectrally resolved arterial $\mu_{a\_app}$ for fatty tissue containing two absorbing heterogeneities (artery and bile duct) adjacent to each other at depth of 4 mm. The reflectance contributions from all 13 sources were added to each detector and the fit used absolute reflectance data. Both the arterial and bile absorption coefficients were varied in each fit simultaneously..... | 55 |
| 51: Plot of spectrally resolved bile $\mu_{a\_app}$ for fatty tissue containing two absorbing heterogeneities (artery and bile duct) adjacent to each other at depth of 4 mm. The reflectance contributions from all 13 sources were added to each detector and the fit used absolute reflectance data. Both the arterial and bile absorption coefficients were varied in each fit simultaneously.....     | 56 |
| 52: Plot of spectrally resolved arterial $\mu_{a\_app}$ for fatty tissue containing two absorbing heterogeneities (artery and bile duct) adjacent to each other at depth of 6 mm. The reflectance contributions from all 13 sources were added to each detector and the fit used absolute reflectance data. Both the arterial and bile absorption coefficients were varied in each fit simultaneously..... | 56 |
| 53: Plot of spectrally resolved bile $\mu_{a\_app}$ for fatty tissue containing two absorbing heterogeneities (artery and bile duct) adjacent to each other at depth of 6 mm. The reflectance contributions from all 13 sources were added to each detector and the fit used absolute reflectance data. Both the arterial and bile absorption coefficients were varied in each fit simultaneously.....     | 57 |
| 54: Plot of spectrally resolved arterial $\mu_{a\_app}$ for fatty tissue containing two absorbing heterogeneities (artery and bile duct) adjacent to each other at depth of 8 mm. The reflectance contributions from all 13 sources were added to each detector and the fit used absolute reflectance data. Both the arterial and bile absorption coefficients were varied in each fit simultaneously..... | 58 |
| 55: Plot of spectrally resolved bile $\mu_{a\_app}$ for fatty tissue containing two absorbing heterogeneities (artery and bile duct) adjacent to each other at depth of 8 mm. The reflectance contributions from all 13 sources were added to each detector and the fit used absolute reflectance data. Both the arterial and bile absorption coefficients were varied in each fit simultaneously.....     | 58 |



|  |    |
|--|----|
| 56: Comparison of arterial $\mu_{a\_app}$ at 650 nm for tissue containing two absorbing heterogeneities (artery and bile duct) placed adjacent to each other at depths of 4 mm, 6 mm and 8 mm.....   | 59 |
| 57: Comparison of bile $\mu_{a\_app}$ at 650 nm for tissue containing two absorbing heterogeneities (artery and bile duct) placed adjacent to each other at depths of 4 mm, 6 mm and 8 mm. ....  | 60 |
| 58: Depth-wise arterial $\mu_{a\_app}$ for a detector placed on the peak absorption surface location. Tissue geometry consisted of two absorbing heterogeneities (artery and bile duct both centered at 4 mm depth, adjacent to each other); all sources were added to a single detector, reflectance data fitting was relative; only the arterial absorption of the top and bottom layers was varied in each fit..... | 61 |
| 59: Depth-wise arterial $\mu_{a\_app}$ for a detector placed on the peak absorption surface location. Tissue geometry consisted of two absorbing heterogeneities (artery and bile duct both centered at 6 mm depth, adjacent to each other); all sources were added to a single detector, reflectance data fitting was relative; only the arterial absorption of the top and bottom layers was varied in each fit..... | 61 |
| 60: Depth-wise arterial $\mu_{a\_app}$ for a detector placed on the peak absorption surface location. Tissue geometry consisted of two absorbing heterogeneities (artery and bile duct both centered at 8 mm depth, adjacent to each other); all sources were added to a single detector, reflectance data fitting was relative; only the arterial absorption of the top and bottom layers was varied in each fit..... | 62 |
| 61: Comparison of depth-wise arterial $\mu_{a\_app}$ of 650 nm for tissue containing two absorbing heterogeneities (artery and bile duct) placed adjacent to each other at depths of 4 mm, 6 mm and 8 mm.....  | 63 |
| 62: Plot of arterial $\mu_{a\_app}$ comparing the effect of change in the background scattering coefficient on the apparent absorption of tissue containing a heterogeneity.....   | 64 |
| 63: Plot of depth-wise arterial $\mu_{a\_app}$ comparing the effect of change in the assumed background scattering coefficient on the apparent absorption of tissue containing a heterogeneity.....  | 64 |

## LIST OF TABLES

| Table |  | Page |
|-------|--|------|
| 1:    | Values for parameters $S_B$ , $x$ , and $S_W$ used in equation (2.4.1)<br>to estimate $\mu_a(\lambda)$ for each tissue. .... | 12   |
| 2:    | Values for parameters $a$ and $b$ used in equation (2.4.2)<br>to estimate $\mu_s'(\lambda)$ for each tissue. ....            | 12   |

## CHAPTER 1

### INTRODUCTION

#### 1.1 Biliary Tree Anatomy

The gallbladder is a thin-walled sac attached to the posterior surface of the liver. It is connected to the common bile duct (CBD) via the cystic duct. The CBD varies approximately from 7 cm to 9 cm in length and after converging with the pancreatic duct it connects into the small intestine. This tree-like structure of small channels and ducts that transport bile from the liver to the lumen of the small intestine is known as the biliary tree (Figure 1) [1]. The biliary tree is embedded in fat and other connective tissues [2, 3].

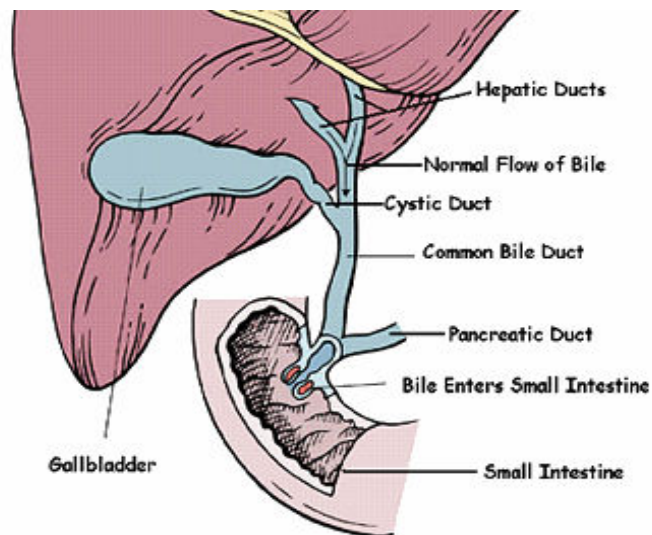


Figure 1: Biliary tree anatomy

#### 1.2 Disorders of the Biliary Tree Structure

Human health issues involving the biliary tree include disorders of the gallbladder, the extrahepatic bile duct and tumors of the gallbladder. However, the most

common (>95%) disorder encountered is cholelithiasis, or gallstones, and cholecystitis, or swelling of gallbladder. These stones may block the flow of bile out of the gallbladder, causing the organ to swell. The annual costs of managing these disorders are 6 billion dollars [4].

Surgical removal of the gallbladder (cholecystectomy) is the standard and permanent treatment for gallstones in the gallbladder. There are two ways of performing gallbladder surgeries; laparoscopic cholecystectomy and open cholecystectomy. Open surgery is done through a large abdominal incision while laparoscopic surgery is done through small punctures in the abdominal wall. Laparoscopic surgeries result in less pain and a faster patient recovery but have higher rates of bile duct injuries as they deprive the surgeon of tactile sensation. Occurrence of the bile duct injuries in laparoscopic surgeries is twice as compared to the open surgeries [5, 6] .

### 1.3 Complications Resulting from Cholecystectomy Procedures

Though cholecystectomy has a low rate of complications (0.4%) [7], serious complications such as injury to the bile ducts, blood vessels, or intestine might occur, requiring corrective surgery that has variable long term outcomes. An injured CBD can leak bile and cause a painful and potentially dangerous infection. Bile duct injuries can lead to high patient morbidity and treatment costs [8, 9]. Injury to the CBD is the most important complication of laparoscopic cholecystectomy (LC), affecting approximately 2000 patients annually in the United States [10].

As the biliary tree structure is embedded in fatty tissue, it can not be visualized directly. As such the main challenge for the surgeon is to guess the exact location and

orientation of the biliary tree structure. Recently, it has been demonstrated that for most cases injury of the biliary tree occurred because of surgeon's incorrect interpretation of the location and orientation of the biliary tree and not because of actual technical factors [5]. Usually the most common cause of bile duct injury is misjudging the location where the cystic duct converges into the CBD. The occurrence of such errors can be eliminated if actual visualization of the bile duct were possible.

#### 1.4 Clinical Imaging Modalities Currently in Use During Cholecystectomy

Various imaging modalities have been used to visualize stones in the CBD during laparoscopic cholecystectomy. The most commonly used techniques are intraoperative cholangiography (IOC), and intraoperative ultrasonography (IUS).

IOC is performed by injecting a contrast agent in the cystic duct and obtaining radiographic images. IOC provides a surgical road map of the CBD [11]. Thus the IOC might decrease the rate of bile duct injuries but cannot fully prevent them as this technique has its own limitations. In order to perform IOC, catheterization of the cystic duct is necessary. This invasive procedure is by itself prone to causing injuries and at a worst case scenario it could lead to severe inflammation [12]. It has also been demonstrated that IOC is costly and time inefficient in preventing bile duct injuries and therefore is not widely practiced during cholecystectomy procedures [4].

The other commonly used imaging modality for visualization of the biliary tree is IUS. Though IUS has greater sensitivity and accuracy than IOC, it is not widely practiced because of poor resolution and contrast that makes images difficult to interpret [13, 14].

### 1.5 Purpose of this Work: Use of Optical Imaging to Improve Cholecystectomy Outcome

As currently available technologies fail to provide safe, cost- and time-efficient solutions to overcome the complications arising from cholecystectomy, there is growing demand for better technologies that would help surgeons identify these structures rapidly and non-invasively. Recently, optical imaging modalities have been applied to the problem of localizing biliary tree structures non-invasively [15]. Photons at optical and near-infrared (NIR) wavelengths can penetrate tissues down to a depth of a few centimeters [16] and image contrast is derived from differences in the spectrally resolved absorbance of naturally occurring chromophores that exist in the tissues being probed, such as oxy- and deoxy-hemoglobin [17] and bile [18]. Optical and NIR photons are also scattered very strongly by tissues [15]. Multiple scattering causes a fraction of the incident photon flux to be deflected back towards a detector probe. This is known as a reflectance measurement and it is the only measurement type considered in this work. Even though multiple scattering makes reflectance measurements possible, it also causes severe blurring in the resulting images. Therefore, methodologies to process optical imaging measurements are necessary for improving the localization of biliary tree structures.

The purpose of this thesis work is to propose a new method for localizing biliary tree structures from spectrally resolved NIR reflectance measurements performed by a fiber-based linear probe that is compatible with laparoscopic procedures. Use of this probe is intended to enhance a surgeon's capacity to visualize biliary tree structures intraoperatively despite the lack of tactile sensation. The performance of the probe in

localizing biliary tree structures was tested in simulation for a variety of tissue geometries. The main feature of this newly proposed method is that reflectance data processing is model-based [19, 20], which (1) enables identification of individual biliary tree structures based on differences in their absorbance spectra even when their measured reflectance spectra are spatially overlapped and (2) enables a tissue depth estimate for each of these structures.

## CHAPTER 2

### METHODS

#### 2.1 The Reflectance Probe Geometry

The simulated probe geometry (Figure 2a) used for the computation of spectrally resolved reflectance measurements is a linear array of sources and detectors (Figure 2b). The probe consists of 13 channels placed adjacent to each other and are assumed to be in perfect contact with the tissue surface.

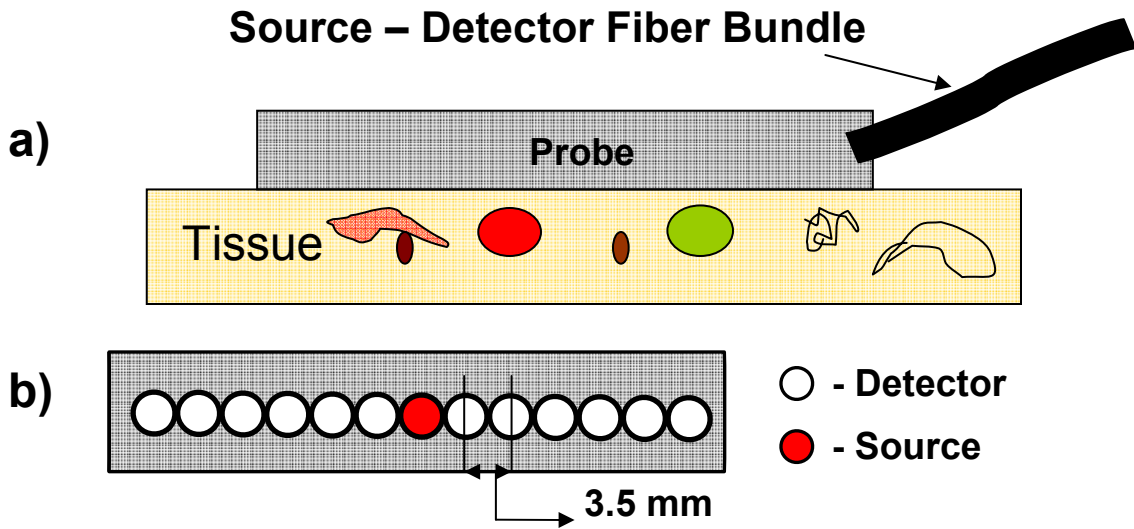


Figure 2: (a) Simulated probe geometry positioning on the tissue surface, (b) Each fiber is bifurcated and can act both as a light source (highlighted in red) and a detector.

Each channel has a diameter of 3.5 mm (Figure 2b) and can act both as a light source and a detector. While one of the channels injects light into tissue the remaining 12 channels collect the light being back-reflected from the tissue (source and detectors,



respectively in Figure 2b). Plane wave illumination is approximated by adding the contributions of all sources to each detector fiber.

## 2.2 Tissue Geometry (Patient-Based and its Simplification for the Simulations)

The biliary tree structure consists of the bile duct with the hepatic artery and portal vein running along it [3]. These structures are embedded into connective tissue and fat at a depth of 2-6 mm from the fatty tissue surface and therefore cannot be directly visualized by the surgeon. Clinical experience has shown that there can be significant variation in anatomical geometry and spatial orientation of biliary tree structures between patients.

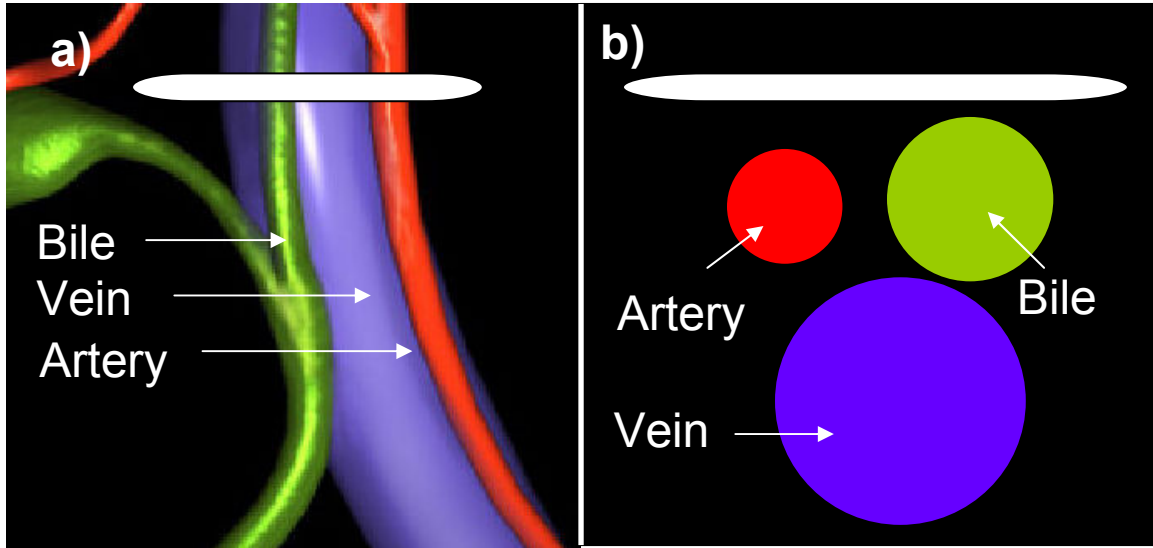


Figure 3: (a) Patient-based geometry of the biliary tree. The geometrical plane containing the probe intersects the biliary tree at right angles (b) Simplified tissue geometry for the simulation. The red color circle represents a cross-section of the artery, the green color circle that of the bile duct and the blue circle that of the vein.

Nevertheless, due to anatomical access constraints imposed by laparoscopic surgery the linear reflectance probe is expected to touch the fatty tissue surface at an approximately right angle orientation with respect to the head-to-toe orientation of the

biliary tree (Figure 3a). Therefore, in our simulations we have simplified the measurement geometry to that of three cylindrical tubes (hepatic artery, CBD, portal vein) running parallel to each other at various relative distances and depths from the tissue surface. The CBD will be henceforth referred to as the ‘bile duct’. The linear probe intersects these three parallel cylinders at right angles making these appear as circles at a face-on view of the intersection plane (Figure 3b).

### 2.3 Proposed Method for the Localization of Biliary Tree Structures

A novel way of applying previously reported computational models for diffuse photon propagation in the semi-infinite [19] and two-layer [20] geometries is proposed for the localization of biliary tree structures. This is a two-step model-based approach for localizing absorbing heterogeneities embedded in fatty tissue (e.g. a blood vessel and the bile duct). The first step attains lateral localization on the fatty tissue surface and the second step attains an estimate of their depth in tissue. In this work it is shown that differences in the absorption spectra of these heterogeneities form the basis for their spatial localization even when they are in close proximity.

#### 2.3.1 Localization of Biliary Tree Structure on the Fatty Tissue Surface

When light from a single source is injected into tissue the probability of any photon been detected at a given detector location is a function of source-detector separation. The two-point probability density function that a photon will sample a given tissue voxel and will subsequently reach a given detector [21] has a shape that is popularly referred to as a ‘banana’ (Figure 4a). The fat-embedded absorbing

heterogeneities (hepatic artery, portal vein and the bile duct) intersected by this banana-shaped volume will have an impact on the measured spectrally resolved reflectance. In the case of the fiber-based linear probe one can switch between different source-detector pairs, which effectively shifts the probe volume laterally and thus different heterogeneities are probed sequentially (Figure 4b).

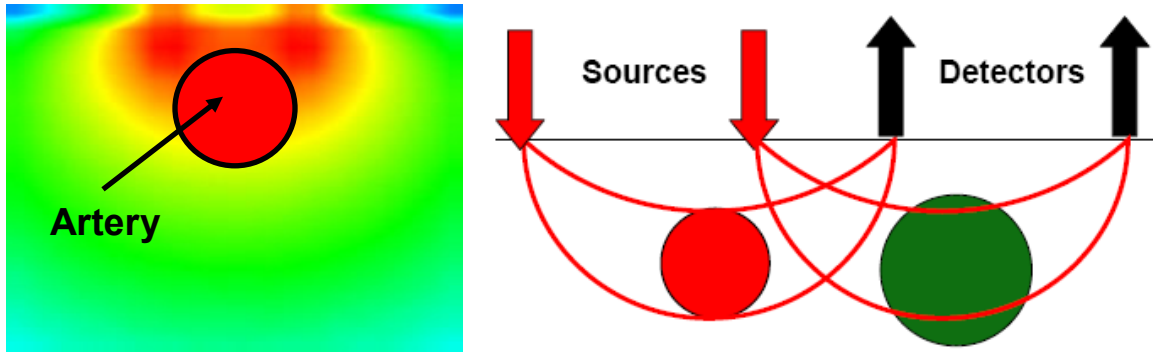


Figure 4: (a) The two-point probability density function attains highest values in a tissue volume, connecting source and detector that is shaped as a ‘banana’. (b) Lateral source-detector displacement results in a displacement of the ‘banana’, i.e. of the tissue volume being probed.

Clearly, the detected reflectance spectrum will be different for the case where the probed tissue volume intersects the hepatic artery versus when it intersects the bile duct as the corresponding absorbance spectra of oxy-, deoxy-hemoglobin and bile are known to be different (Figure 6).

These differences in detected spectrally resolved reflectance form the basis for identifying what types of biliary tree structures are being probed in each measurement. More specifically, reflectance data are fitted to the diffusion equation for a semi-infinite medium by a non-linear least squares code that expresses the estimated tissue optical

properties as a weighted sum of tissue chromophore absorbance spectra [22, 23]. This way the spectrally resolved optical properties of the tissue volume being probed are estimated for different source-detector separation combinations. It is important to note that the goal of this process is not to deduce quantitative tissue optical properties, but to simply detect if there is significant presence of any one of several known chromophores within the tissue volume being probed and thus help the surgeon localize major blood vessels and the bile duct.

### 2.3.2 Tissue Depth Estimation of Biliary Tree Structures

In the second step of our analysis method we fit the same spectrally resolved reflectance data to a two-layer model of diffuse photon propagation [20] and use the top layer thickness as a depth gauge for the absorbing heterogeneity. The logic of this approach is outlined in Figure 5: The top layer partitions the banana-shaped probe volume in two (the part covered by the light blue area and the one that is not).

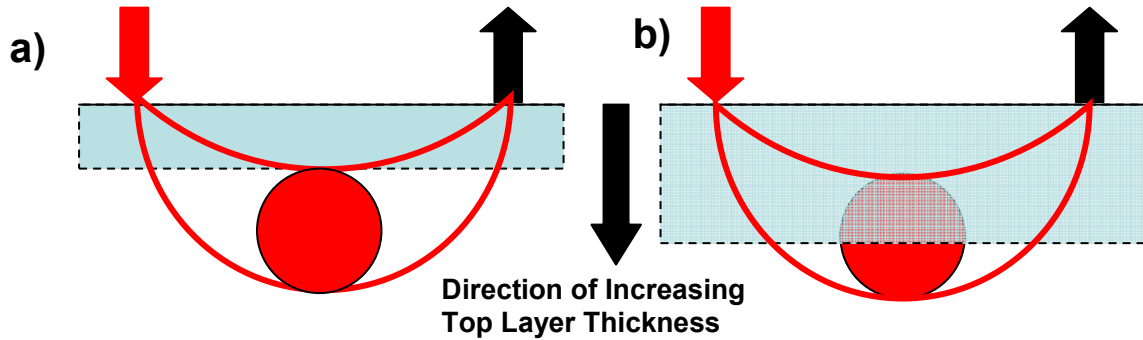


Figure 5: Pictorial representation of the depth-localization strategy for an absorption heterogeneity; the top layer thickness (a) touches the top side of the artery, and (b) crosses through its center.

If the top layer thickness is shallow the part of the ‘banana’ overlapping the top layer will not be sampling the absorption heterogeneity (as in Figure 5a) and the resulting fitted absorption coefficient for the top layer is similar to that of the background fatty tissue. As the top layer thickness is made incrementally larger, the portion of the ‘banana’ overlapping the top layer will eventually cover part of the absorbing heterogeneity (as in Figure 5b), which will result in a jump for the fitted top layer absorption coefficient.

The top layer thickness value where the absorption coefficient transitions from a low to a high value provides a reasonably accurate depth estimate for the location of the top side of the hepatic artery or of the bile duct. Knowledge of the depth of a vessel is very useful to surgeons as it informs them how deep to cut without damaging that vessel.

## 2.4 Tissue Optical Properties

Light-tissue interactions are characterized by the strength of absorption and scattering that light experiences as it propagates through tissue. Tissue absorption depends on the resident chromophore concentrations, such as oxy- and deoxy-hemoglobin, and scattering depends on tissue structure [24]. These tissue-specific optical properties enable us to probe the physiology and structure of tissues.

The spectral absorption coefficient ( $\mu_a(\lambda)$ ) of tissues was defined as a weighted sum of the absorption coefficient of the oxy-hemoglobin ( $\mu_{aHbO_2}$ ), deoxy-hemoglobin ( $\mu_{aHb}$ ), water ( $\mu_{aW}$ ) [25] and bile ( $\mu_{aBile}$ ) as function of wavelength ( $\lambda$ ) (Equation 2.4.1) [26].

$$\mu_a(\lambda) = S_B(x\mu_{aHb}(\lambda) + (1-x)\mu_{aHbO_2}(\lambda)) + S_W\mu_{aW}(\lambda) + S_{Bile}\mu_{aBile}(\lambda) \quad (2.4.1)$$

where  $x = (HbO_2 + Hb)/Hb$  and  $S_B$ ,  $S_W$  and  $S_{Bile}$  were heuristic scaling factors adjusted to match the absorption data currently available in the literature for each tissue type [26].

The spectral scattering coefficient was defined by an empirical formula based on Mie scattering theory (Equation 2.4.2) [26].

$$\mu_s'(\lambda) = a \times \lambda^{-b} mm^{-1}, \lambda \text{ in nm} \quad (2.4.2)$$

where  $a$  and  $b$  are constants controlling the spectral variation in each tissue [26].

The parameters involved in the calculation of tissue optical properties are shown with their wavelength-independent tissue-specific values in Tables 1 and 2.

Table 1: Values for parameters  $S_B$ ,  $x$ , and  $S_W$  used in equation (2.4.1) to estimate  $\mu_a(\lambda)$  for each tissue type.

| Tissue Type | $S_B$  | $x$  | $S_W$ | References   |
|-------------|--------|------|-------|--|
| Adipose     | 0.0033 | 0.7  | 0.5   | (Mitic <i>et al.</i> 1994, Kienle <i>et al.</i> 1996, Holboke <i>et al.</i> 2000, Srinivasan <i>et al.</i> 2003) |
| Whole blood | 1      | 0.75 | 0     | (Enejder <i>et al.</i> 2003)   |

Table 2: Values for parameters  $a$  and  $b$  used in equation (2.4.2) to estimate  $\mu_s'(\lambda)$  for each tissue type.

| Tissue Type | $a$ (mm <sup>-1</sup> ) | $b$ (no units) | References   |
|-------------|-------------------------|----------------|--|
| Adipose     | 38                      | 0.53           | (Mitic <i>et al.</i> 1994, Kienle <i>et al.</i> 1996, Holboke <i>et al.</i> 2000, Srinivasan <i>et al.</i> 2003) |
| Whole blood | 1.33                    | 0.66           | (Enejder <i>et al.</i> 2003)   |

The tissue optical properties relevant to this work are shown in Figures 6 and 7.

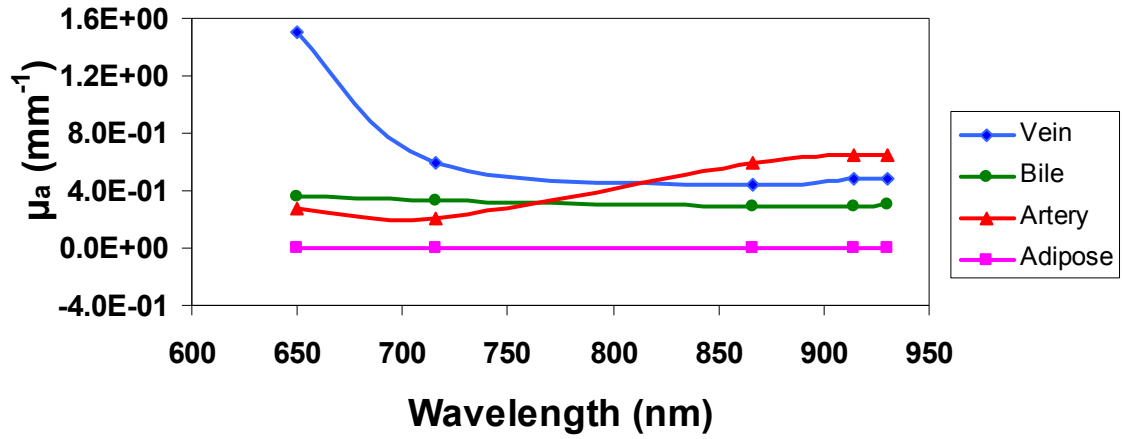


Figure 6: Plot of the absorption coefficient spectra for the tissue types considered in this computational work.

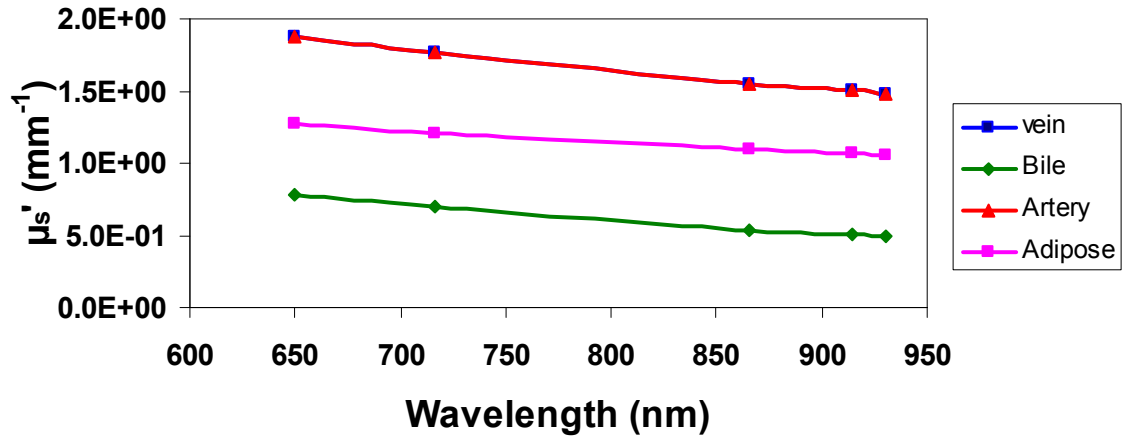


Figure 7 : Plot of the transport scattering coefficient spectra for the tissue types considered in this computational work.

## 2.5 Monte Carlo Simulation

Light-tissue interactions have historically been simulated by Monte Carlo [27], which is a stochastic method to model photon propagation in tissues. Monte Carlo can in principle simulate the physical process of photon transport without making any

approximations. In reality Monte Carlo codes often simulate approximate transport models because the details of the photon-tissue interaction processes are too complicated and/or are not accurately known. Approximations are also often made to reduce computation times. We used the tMCimg [28] code to simulate the transport of optical and near-infrared photons through the biliary tree tissue geometry described above (figure 3b) and scored photons into a linear array of detectors (figure 2). The tMCimg code allows to model photon transport in arbitrarily complex tissue geometries under the constraint that these can be represented as a cubic voxel image volume.

At the beginning of each simulation the position, direction and radius of the photon source are defined [28]. The photon is launched into tissue within the output cone of the source optical fiber (of finite numerical aperture). Once launched, most photons undergo multiple scattering events before they exit tissue. Photons of a defined light wavelength are propagated through the predefined tissue volume geometry that has been assigned appropriate optical properties for each tissue type and photon wavelength. The size of steps that photons take between scattering events in each tissue are determined by appropriate stochastic sampling of the light scattering probability distribution for that tissue. In a similar fashion the angular probability distribution for single scatter events is also sampled so as to determine the new photon direction after each scattering event. These probability distributions need to be specified *a priori* by the Monte Carlo user. In this code the step length choice is based on a negative exponential probability function and the new scatter direction is based on the Henyey-Greenstein phase function [29]. Photons are propagated until they reach an air-tissue boundary, whereupon a decision is



made on whether they will be totally internally reflected and continue to propagate in tissue, or exit into air or into a detector fiber. To reduce computation times, if a photon is trapped in tissue for a time that is much longer ( $\sim 10$  ns) than typical tissue escape times ( $< 1$  ns), the simulation gives up on that photon and starts a new photon history.

When photons exiting tissue hit predefined detector locations some information about their history in tissue (how many times they scattered and how long they spent in each tissue type) is recorded into a history file. At the end of each Monte Carlo run the history information for all scored photons is processed for tissue absorption by applying Beer's law [29] to the pathlength traveled in each tissue type. After applying this absorption correction the simulated reflectance at each linear probe detector is attained. In addition to reflectance calculations, the tMCimg code can simultaneously compute the two-point probability density function [21] for any source-detector pair.

## 2.6 Semi-Infinite, Spectrally Resolved Diffusion Model

The diffusion equation solution for a medium in the semi-infinite geometry was implemented in C on a Linux platform [30]. The diffusion equation was solved for an extrapolated boundary condition and a 1.4/1 refractive index mismatch at the boundary. The tissue-simulating semi-infinite medium was characterized by its optical properties, namely the absorption ( $\mu_a(\lambda)$ ) and transport scattering ( $\mu_s'(\lambda)$ ) coefficients at each photon wavelength  $\lambda$ . The transport scattering coefficient was calculated from the scattering coefficient ( $\mu_s$ ) and an anisotropy factor  $g$  (mean cosine of the scattering angle) by using  $\mu_s' = \mu_s(1 - g)$  and  $g = 0.9$ . The illumination beam originating from each fiber bundle of the

linear probe was approximated as an isotropic photon source placed at a tissue depth of one transport mean free path,  $z_0 = l/(\mu_s' + \mu_a)$ .

Following the semi-infinite medium solution by Haskell et al [30] fluence rate is given by:

$$REAL = \frac{\exp(-k_{real}r_0)}{r_0} - \cos[k_{imag}(r_{0b} - r_0)] \times \frac{\exp(-k_{real}r_{0b})}{r_{0b}} \quad 2.6.1$$

$$IMAG = \sin[k_{imag}(r_{0b} - r_0)] \frac{\exp(-k_{real}r_{0b})}{r_{0b}} \quad 2.6.2$$

$$k_{real} = \sqrt{\frac{3}{2} \beta \sigma_{tr}} \left[ \sqrt{1 + (\omega\tau)^2} + 1 \right]^{1/2} \text{ and } k_{imag} = \sqrt{\frac{3}{2} \beta \sigma_{tr}} \left[ \sqrt{1 + (\omega\tau)^2} - 1 \right]^{1/2}$$

$$r_0 = (\lambda_{tr}^2 + \rho^2)^{1/2}, r_{0b} = [(2zb + \lambda_{tr})^2 + \rho^2]^{1/2}, \text{ and } z_b = 2D_1(1 + R_{eff})/(1 - R_{eff})$$

In our case imaginary part was zero as we made CW measurements.

The optical properties used in the semi-infinite, spectrally resolved diffusion model are discussed in Section 2.4

## 2.7 Two-Layer, Spectrally Resolved Diffusion Model

### 2.7.1 Diffusion Equation (Forward Model)

A solution of the diffusion equation in the two-layer geometry for steady-state illumination was implemented in C on a Linux platform [31]. The first layer of the two-layer medium has a thickness  $l$  and the second layer is semi-infinite with  $\mu_{ai}, \mu_{si}'$  being the absorption and transport scattering coefficients of layers  $i=1$  and 2, respectively. As in the case of the semi-infinite medium geometry the optical fiber based light source is

approximated by an isotropic source at depth  $z_0$ , where  $z_0$  is assumed to be smaller than the top-layer thickness  $l$ . The  $z$  coordinate defines the vertical position, or depth into the medium;  $x$  and  $y$  coordinates define locations on the medium's surface and  $\rho = (x^2 + y^2)^{1/2}$ .

Using this notation the steady-state two-layer medium diffusion equation is stated as:

$$D_1 \Delta \Phi_1(r) - \mu_{a1} \Phi_1(r) = -\delta(x, y, z), \quad 0 \leq z < 1 \quad (2.7.1.1)$$

$$D_2 \Delta \Phi_2(r) - \mu_{a2} \Phi_2(r) = 0, \quad z \leq 1 \quad (2.7.1.2)$$

Where  $r = (x, y, z)$ ,  $D_i = 1/3(\mu'_{si} + \mu_{ai})$  and  $\Phi_i$  are the diffusion constant and the fluence rate of layer  $i$ , respectively [31]. The fluence rates in layers 1 and 2 ( $\Phi_1$  and  $\Phi_2$ ) are given by:

$$\Phi_1(z, s) = \frac{\sinh[\alpha_1(z_b + z_0)]}{D_1 \alpha_1} \times \frac{D_1 \alpha_1 \cosh[\alpha_1(\lambda - z)] + D_2 \alpha_2 \sinh[\alpha_1(\lambda - z)]}{D_1 \alpha_1 \cosh[\alpha_1(\lambda + z_b)] + D_2 \alpha_2 \sinh[\alpha_1(\lambda + z_b)]} - \frac{\sinh[\alpha_1(z_0 - z)]}{D_1 \alpha_1}, \quad 0 \leq z < z_0, \quad (2.7.1.3)$$

$$\Phi_1(z, s) = \frac{\sinh[\alpha_1(z_b + z_0)]}{D_1 \alpha_1} \times \frac{D_1 \alpha_1 \cosh[\alpha_1(\lambda - z)] + D_2 \alpha_2 \sinh[\alpha_1(\lambda - z)]}{D_1 \alpha_1 \cosh[\alpha_1(\lambda + z_b)] + D_2 \alpha_2 \sinh[\alpha_1(\lambda + z_b)]}, \quad 0 < z < \lambda \quad (2.7.1.4)$$

$$\Phi_2(z, s) = \frac{\sinh[\alpha_1(z_b + z_0)] \exp[\alpha_2(\lambda - z)]}{D_1 \alpha_1 \cosh[\alpha_1(\lambda + z_b)] + D_2 \alpha_2 \sinh[\alpha_1(\lambda + z_b)]} \quad (2.7.1.5)$$

Where  $\alpha_i^2 = \frac{(D_i s^2 + \mu_{ai})}{D_i}$  and  $s^2 = s_1^2 + s_2^2$ .

The steady-state diffusion equations (2.7.1.1) and (2.7.1.2) are solved for a 1.4/1 refractive index mismatch occurring at the tissue/air interface and using the extrapolated boundary condition for the tissue-air boundary,  $\Phi_1(-z_b, s) = 0$ , where

$z_b = 2D_1(1 + R_{eff})/(1 - R_{eff})$  and  $R_{eff}$  is the fraction of the internally diffusely reflected photons at the boundary which equals 0.493 for a refractive index  $n$  of 1.4 [29].

The spatially and spectrally resolved steady-state diffuse reflectance then reads:

$$R(\rho, \lambda) = 0.118\Phi_1(\rho, \lambda, z)|_{z=0} + 0.306D_1 \frac{\partial}{\partial z}\Phi_1(\rho, \lambda, z)|_{z=0} \quad (2.7.1.6)$$

The solution to equations (2.7.1.1) and (2.7.1.2) [31] was implemented in C code to compute the steady-state reflectance at a given wavelength ( $\lambda$ ) and source-detector separation ( $\rho$ ).

### 2.7.2 Inverse Model

The inverse two-layer diffusion model was based on the Levenberg-Marquardt optimization method, which is a standard non-linear least squares parameter estimation code [32, 33]. The algorithm uses the inverse Hessian and steepest descent methods to determine the minimum of a specified penalty function which we define as  $\chi^2$  [34]. This method has been described in detail in the Numerical Recipes Book [34] and its C code implementation is attached in Appendix A.

The input to the Levenberg-Marquardt code was the Monte Carlo simulated spectrally resolved reflectance data. For each tissue geometry reflectance measurements in the linear probe geometry were simulated at five wavelengths [35]. Monte Carlo reflectance data were fit to semi-infinite [19] and two-layer [20] diffusion models. Unless stated otherwise, it can be assumed that all fits minimized the differences between Monte Carlo and diffusion model based reflectance seen at a single detector for all five wavelengths simultaneously. All source fibers illuminated tissue simultaneously and the

reflectance seen at the single detector location was computed as the sum of the reflectance contributions from each source-detector separation. The Levenberg-Marquardt code minimized the  $\chi^2$  difference between Monte Carlo and diffusion theory in an iterative fashion. The uncertainties used for each data point in the  $\chi^2$  calculation were estimated as a constant % (2%) of the sum of the reflectance contributions from each source-detector separation. This standard deviation value was substantially higher than the Monte Carlo related statistical noise, as it originated from the spatial heterogeneity of underlying tissues.

The semi-infinite geometry fit produced an estimated location on the fatty tissue surface for each absorbing heterogeneity. The fit assumed the background  $\mu_s'(\lambda)$  values and fitted for  $\mu_a(\lambda)$  or, more specifically, the  $S_B$  values (equation 2.3.1) for arterial blood and bile. We refer to the resulting fitted parameters as the spectrally resolved apparent absorption coefficients ( $\mu_{a\_app}$ ) for blood and bile, as these represent a spatially averaged value of the absorption experienced within the tissue volume probed. The latter was defined by the sum of all ‘bananas’ of the source-detector separations included in each summed reflectance calculation.

The two-layer geometry fit produced an estimate of the tissue depth for each heterogeneity type. Each fit included only reflectance measurements made at the detector location that was previously found, through the semi-infinite fit analysis, to have the maximum absorption on the tissue surface for each heterogeneity type. These locations were approximately on top of the artery and bile duct respectively, as deduced from the semi-infinite fitting step above. The two-layer geometry (equations 2.4.1 and 2.4.2) is

described by five optical property parameters: the absorption and transport scattering coefficients of the top and bottom layers ( $\mu_{a1}, \mu_{s1}', \mu_{a2}, \mu_{s2}'$ ) and the top layer thickness  $l$ . In this case, fitting results represent a spatial average of the apparent absorption coefficients of blood or bile ( $\mu_{a\_app1}, \mu_{a\_app2}$ ) in each layer. Evaluation of  $\mu_{a\_appi}$  in the inverse model requires initial guesses for all parameter values. The initial guesses for the absorption and transport scattering coefficients were set to those of fatty tissue as this was the uniform background tissue in which all heterogeneities were embedded. In all data fitting procedures only absorption coefficients were varied while transport scattering ones were kept constant at the initial guess values. In contrast to the semi-infinite medium case, where the arterial blood and bile absorption spectra were fitted simultaneously, the increased number of unknowns in the two-layer geometry allowed for fitting only a single absorption spectrum at a time. This means that even though the spectrally resolved reflectance at each detector possibly contained absorption contributions from both arterial blood and bile, we nevertheless fitted results as if there was only blood or only bile in the probe tissue volume. It should be reminded that the purpose of this exercise was not to deduce quantitative absorption values but rather locate a peak in absorption as function of depth. As we see in the following Sections, does produce promising results despite the crude approximations made.

The robustness of fitting results was also tested, both for the semi-infinite and two-layer geometries, against false initial guesses for the background transport scattering coefficients, as these are likely to occur in experimental reality.

## CHAPTER 3

### RESULTS AND ANALYSIS

The spectrally resolved reflectance MC data was used as input to semi-infinite and two-layer diffusion theory based inverse models to evaluate the apparent absorption coefficient for each heterogeneity type. Reflectance measurements were simulated for a variety of biliary tree spatial configurations and tissue depths. Section 3.1 describes how the semi-infinite diffusion inverse model was used for lateral localization of these heterogeneities on the fatty tissue surface. Section 3.2 describes how the two-layer diffusion inverse model was used to estimate the tissue depth of these absorption heterogeneities.

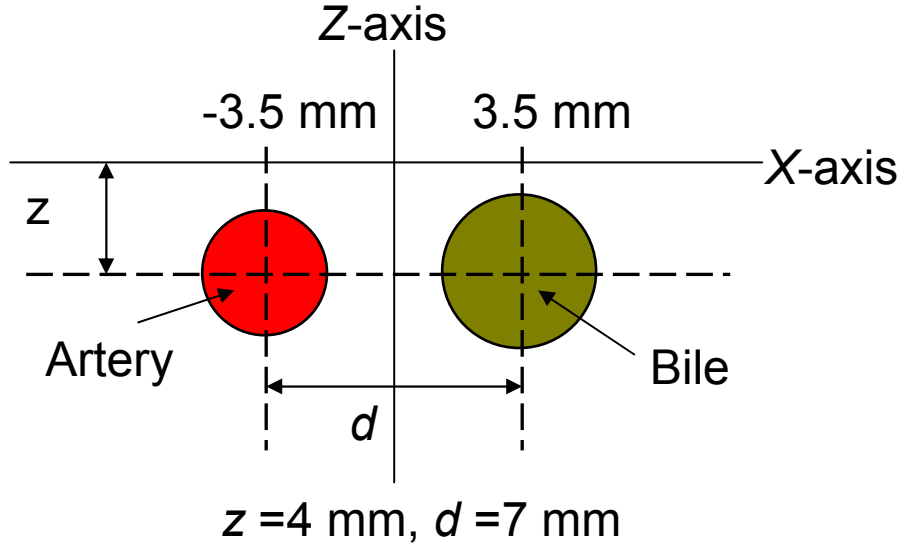


Figure 8: Location of absorbing heterogeneities in the simulated tissue geometry.

### 3.1 Lateral Localization of Absorption Heterogeneities

#### 3.1.1 Lateral Localization of a Single Absorbing Heterogeneity (Artery)

The spectrally resolved MC reflectance data was acquired with 13 sources and 13 detectors with a single source being on at a time and all detectors collecting data simultaneously. While adding contributions from all the sources to one detector, the detector coinciding with the source location was not taken into consideration as it would not probe the depths of interest for this application.

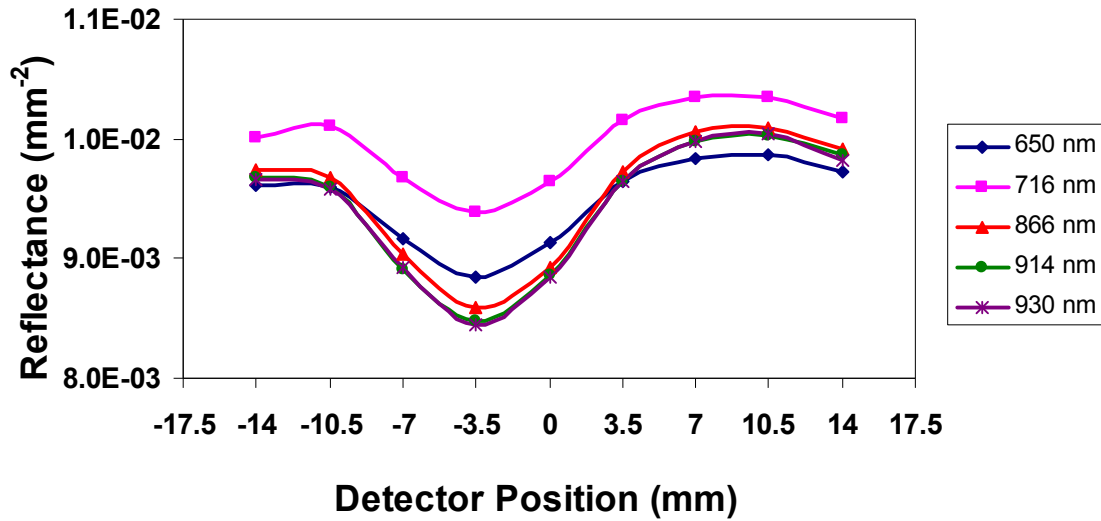


Figure 9: Spectrally resolved reflectance from fatty tissue containing a single absorbing heterogeneity with optical properties of 96% oxygenated (arterial) blood, centered at -3.5 mm. Tissue optical properties are plotted in Figures 6 and 7.

The Figure 9 shows spectral reflectance for fatty tissue with an absorbing heterogeneity located at -3.5 mm laterally (please refer to artery position in Figure 8 for relative placement). The point of minimum reflectance is centered at -3.5 mm because of the presence of the absorbing heterogeneity at that location and because we are using planar illumination (all sources on simultaneously). The absorbing heterogeneity has



optical properties of highly oxygenated arterial blood (Table 1) and the background tissue has optical properties of fat (Tables 1 and 2). For arterial blood, an absorbance minimum is found in the vicinity of 716 nm, which results in higher reflectance relative to other illumination wavelengths.

The apparent absorption coefficient of tissue,  $\mu_{a\_app}$ , was obtained by fitting the spectrally resolved reflectance data to the semi-infinite medium inverse model. Fitting for the absorption coefficient was done by giving the initial guess for the different parameters in equation 2.3.1 and varying only one parameter, which was  $S_B$  in this case.

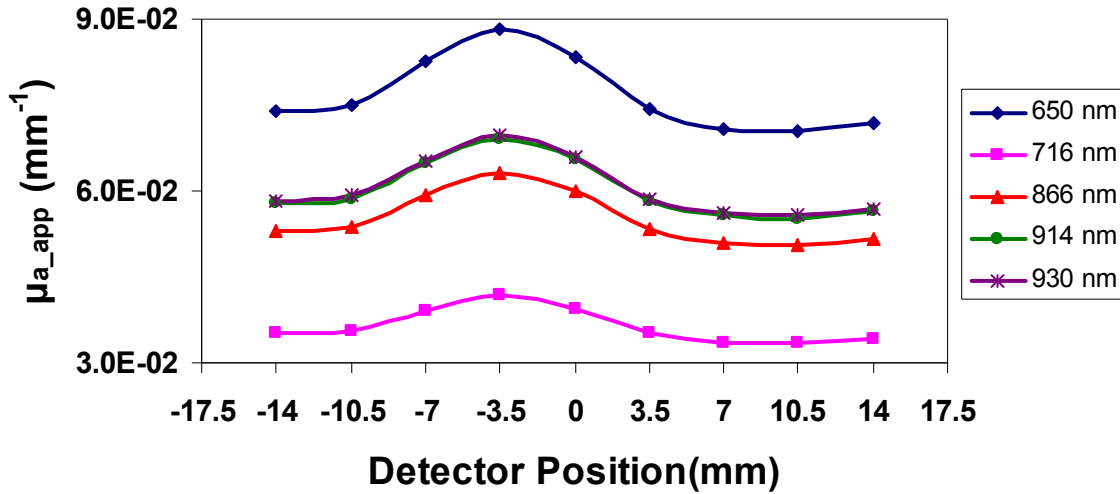


Figure 10: Plot of spectrally resolved arterial  $\mu_{a\_app}$  for fatty tissue containing a single absorbing heterogeneity (artery). The reflectance contribution from all 13 sources was added to each detector and the fit used absolute reflectance data.

Data fitting was performed by having the inverse model either (a) compute a scaling factor that minimizes  $\chi^2$  in every fit iteration [23] (relative fitting), or (b) fit reflectance data to the diffusion model predictions without scaling the former (absolute fitting).

Figure 10 shows  $\mu_{a\_app}$  for fatty tissue containing an absorbing heterogeneity as obtained by absolute reflectance fitting. The point of maximum absorption at -3.5 mm shows the presence of an absorbing heterogeneity at that location. A comparison between Figures 9 and 10 indicates that the spatial variation of the spectrally resolved MC data and the fitted  $\mu_{a\_app}$  values are quantitatively mirror images of each other.

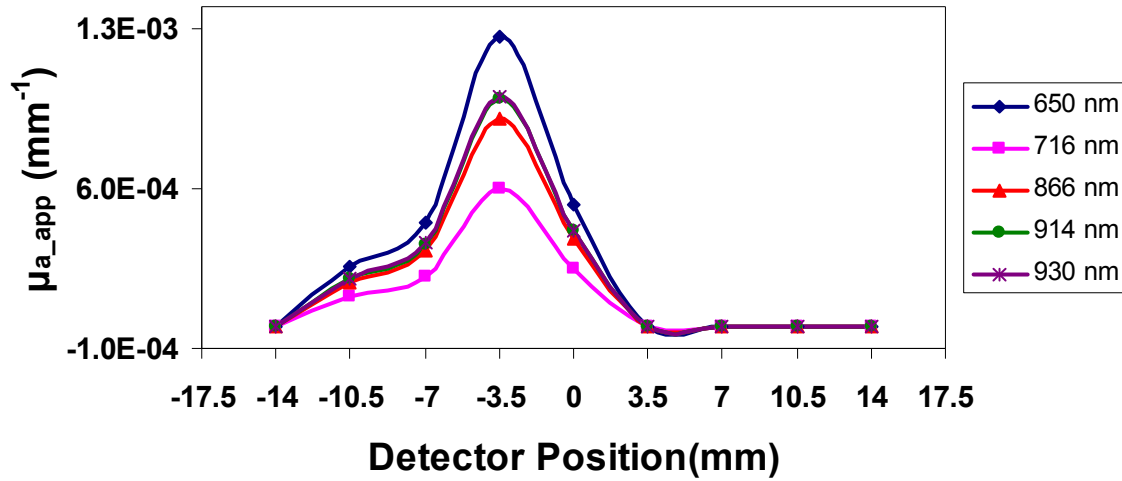


Figure 11: Plot of spectrally resolved arterial  $\mu_{a\_app}$  for fatty tissue containing a single absorbing heterogeneity (artery). The reflectance contribution from all 13 sources was added to each detector and the fit uses relative reflectance data.

Figure 11 shows  $\mu_{a\_app}$  for fatty tissue containing an absorbing heterogeneity as obtained by relative reflectance fitting. Comparison between Figures 10 and 11 indicates that lower apparent absorption values are obtained for relative reflectance fitting (1.27e-03 at 650 nm ) versus absolute fitting (8.82e-02 at 650 nm). The lower apparent absorption translates to a loss of detection sensitivity; relative reflectance fitting introduces an extra degree of freedom in the fitting procedure (Figure 12), which makes the inverse problem less well-posed.

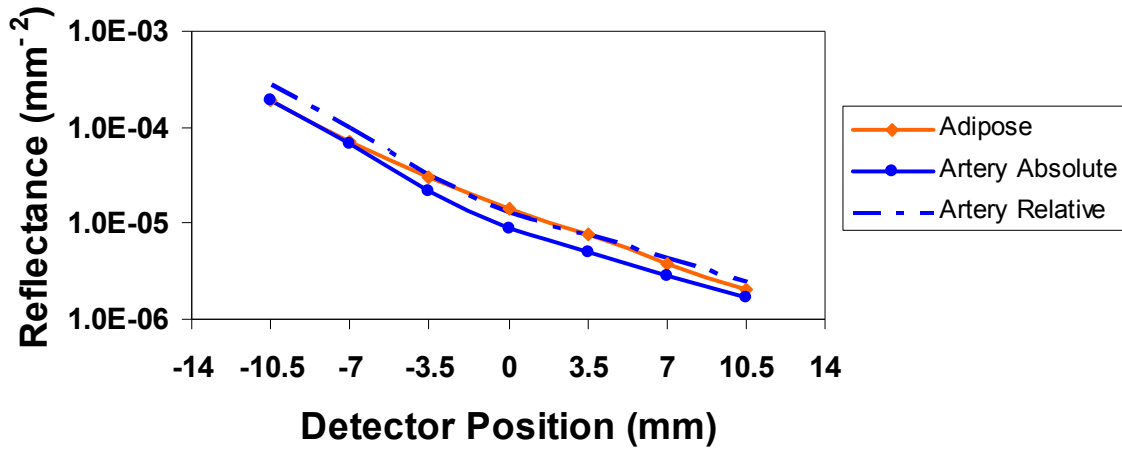


Figure 12: Comparison of the reflectance from fatty tissue containing a single absorbing heterogeneity with optical properties of 96% oxygenated (arterial) blood, centered at -3.5 mm (dotted line) and without absorbing heterogeneity (solid line). Tissue optical properties are plotted in Figure 6 and 7.

Figures 13 and 14 show  $\mu_{a\_app}$  values obtained from reflectance measurements on fatty tissue containing a single absorbing heterogeneity (artery) with reflectance data from only one source-detector pair being included in the fit. As that source-detector pair was moved along the tissue surface the point of maximum absorption shifted from 0 mm to -3.5 mm, which was the true location of the absorbing heterogeneity. This forward shift can be attributed to the parabolic (‘banana’) shape of the photon density function, which projects the photon absorption experienced by light injected into tissue from the source onto the detector (e.g. Figure 4b). As source-detector separation increases the point of maximum absorption shifts with detector location – one can approximately correct for that by assuming that the point of maximum absorption was at the source-detector separation midpoint.

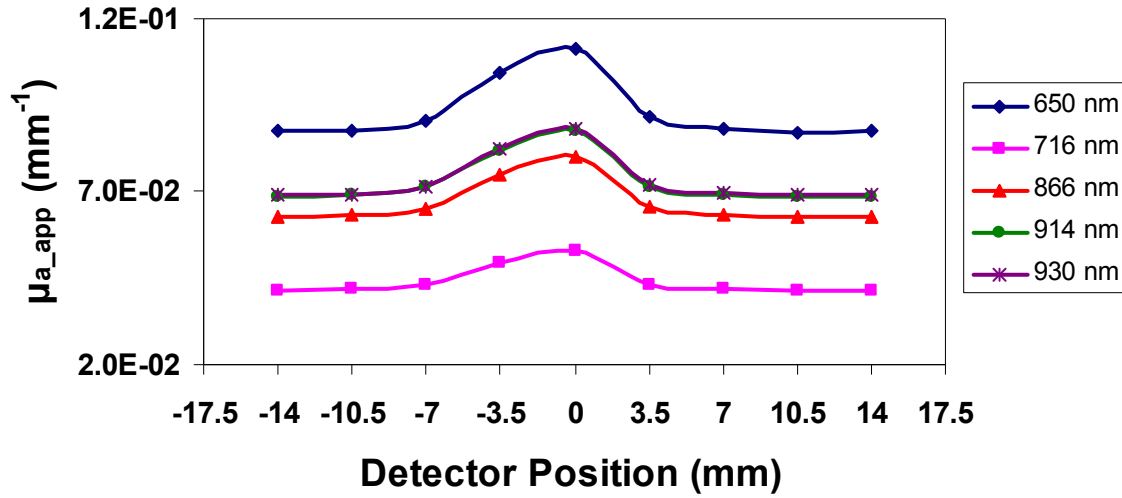


Figure 13: Plot of spectrally resolved arterial  $\mu_{a\_app}$  for fatty tissue containing a single absorbing heterogeneity (artery). The reflectance contribution from only one source-detector pair at 3.5 mm separation was considered and the fit used absolute reflectance data.

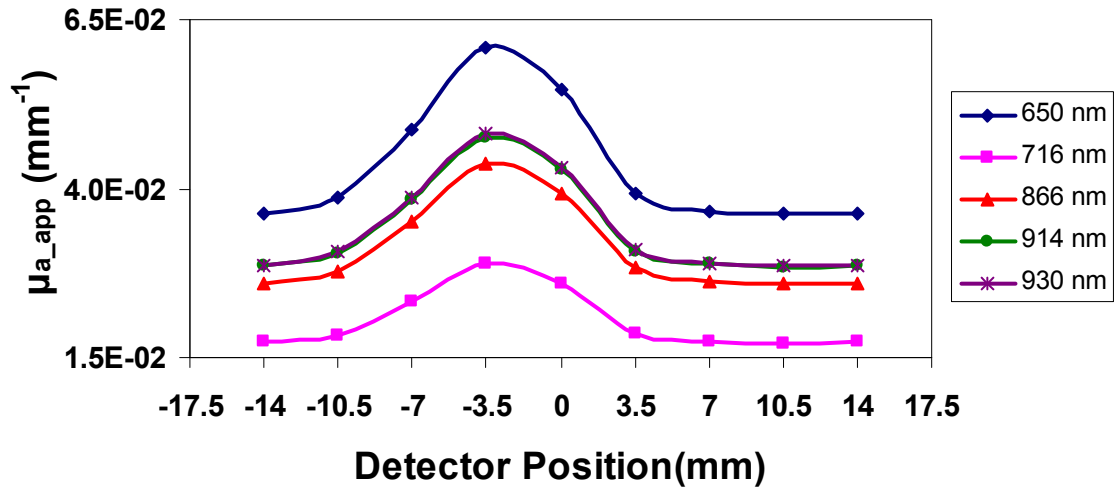


Figure 14: Plot of spectrally resolved arterial  $\mu_{a\_app}$  for fatty tissue containing a single absorbing heterogeneity (artery). The reflectance contribution from only one source-detector pair at 7 mm separation was considered and the fit used absolute reflectance data.

Comparison between Figures 10 and 13 shows that adding the reflectance contribution from all the sources to each detector results in lower  $\mu_{a\_app}$  values ( $8.82\text{e-}02$

at 650 nm at the point of maximum absorption when all sources are on versus  $1.12 \times 10^{-1}$  at 650 nm for a single source–detector pair).

### 3.1.2 Lateral Localization of a Single Absorbing Heterogeneity (Bile Duct)

The spectrally resolved reflectance from fatty tissue containing a single absorbing heterogeneity with the optical properties of human bile, centered at 3.5 mm (please refer to bile position in Figure 8 for relative placement) is shown in Figure 15. As seen from this Figure the point of minimum reflectance is at 3.5 mm, which coincide with the center location of that heterogeneity. Reflectance curves are less well separated compared to the artery (Figure 9) case because of the lesser variation of bile optical properties with light wavelength.

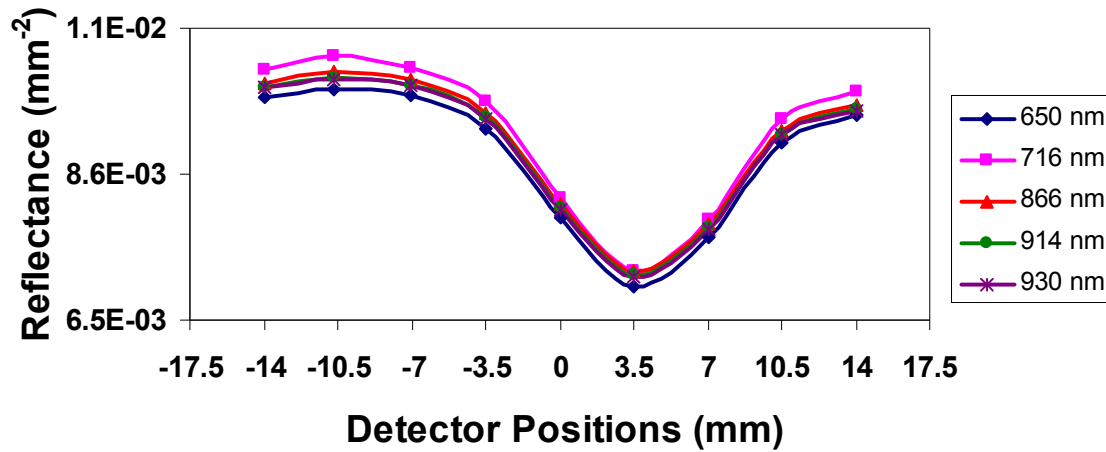


Figure 15: Spectrally resolved reflectance from fatty tissue containing a single absorbing heterogeneity having the optical properties of human bile, centered at 3.5 mm. Tissue optical properties are plotted in Figures 6 and 7.

First, the spectrally resolved reflectance data was fit as absolute. The spectrally resolved apparent absorption for tissue containing an absorbing heterogeneity (bile duct) is shown in Figure 16. The point of maximum absorption is at 3.5 mm which is the true

location of that heterogeneity. The  $\mu_{a\_app}$  value at the point of maximum absorption is  $9.33\text{e-}02$  at 650 nm.

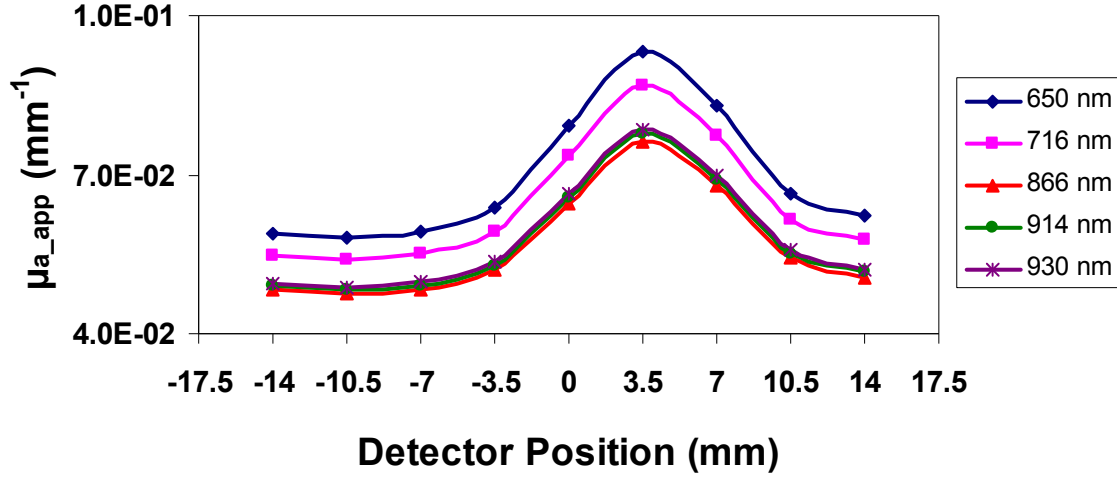


Figure 16: Plot of spectrally resolved bile  $\mu_{a\_app}$  for fatty tissue containing a single absorbing heterogeneity (bile duct). The reflectance contribution from all 13 sources was added to each detector and the fit used absolute reflectance data.

The spectrally resolved  $\mu_{a\_app}$  deduced from moving a single source-detector pair is shown in Figures 17 and 18 for source-detector separations of 3.5 mm and 7 mm, respectively. In case of a 3.5 mm separation the point of maximum absorption is shifted from the true heterogeneity center location. On the other hand, the true heterogeneity center was attained for the 7 mm separation.

In case of 7 mm source-detector separation the point of maximum absorption is observed at 3.5 mm which is the true heterogeneity center location. The value of  $\mu_{a\_app}$  at the point of maximum absorption is  $7.56\text{e-}02$  at 650 nm which is lower than the value  $\mu_{a\_app}$  at point of maximum absorption for 3.5 mm, which was  $1.19\text{e-}01$  at 650 nm. The lower peak amplitude translates into a lack of detection sensitivity. This occurs because the size of the ‘banana’ is larger for the larger source-detector separation and as a result a

higher fraction of photons that have only traveled through adipose tissue reaches the detectors.

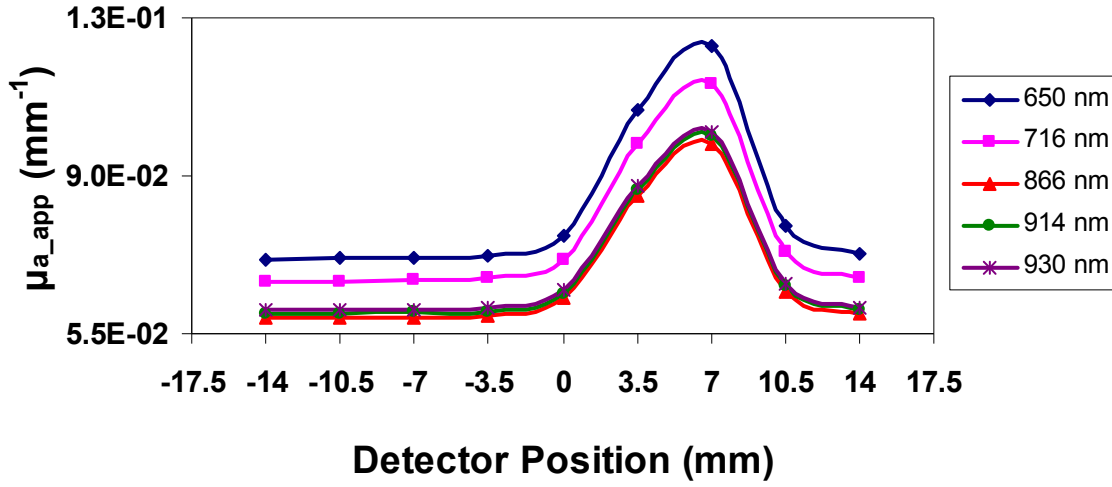


Figure 17: Plot of spectrally resolved bile  $\mu_{a\_app}$  for fatty tissue containing a single absorbing heterogeneity (bile duct). The reflectance contribution from only one source-detector pair at a 3.5 mm separation was considered and the fit used absolute reflectance data.

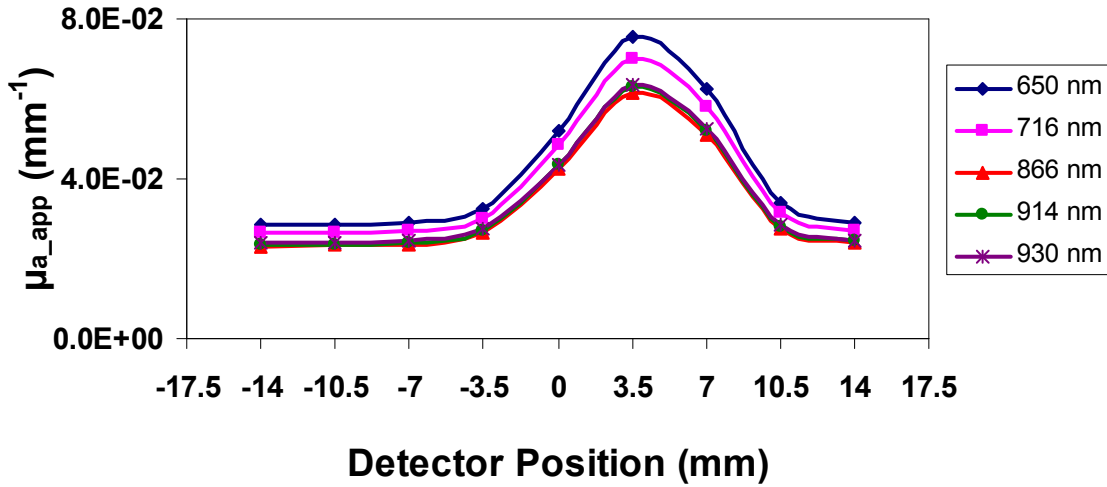


Figure 18: Plot of spectrally resolved bile  $\mu_{a\_app}$  for fatty tissue containing a single absorbing heterogeneity (bile duct). The reflectance contribution from only one source-detector pair of 7 mm separation was considered and the fit used absolute reflectance data.

### 3.1.3 Lateral Localization of Two Absorbing Heterogeneities (Artery and Bile Duct) Separated by 7 mm (Center-to-Center)

The spectrally resolved MC reflectance from fatty tissue containing two absorbing heterogeneities is shown in Figure 19. The simulated tissue geometry contains two absorbing heterogeneities having the optical properties of artery and bile respectively. Artery and bile duct are laterally located at -3.5 mm and 3.5 mm, respectively, resulting in a 7 mm center-to-center (please refer to Figure 8 for their relative placement). The artery and bile duct diameters were 2 mm and 4 mm, respectively. The reflectance contribution from all the sources was added to each detector.

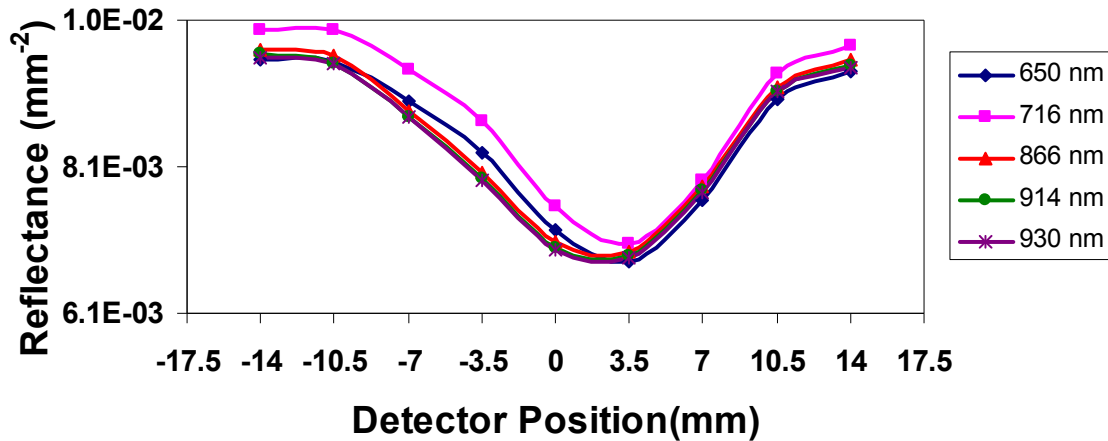


Figure 19: Spectrally resolved reflectance from fatty tissue containing two absorbing heterogeneities with optical properties of arterial blood and bile, centered at -3.5 mm and 3.5 mm respectively. Tissue optical properties are plotted in Figures 6 and 7.

The spectrally resolved reflectance in Figure 19 shows the point of minimum reflectance at 3.5 mm indicating the presence of an absorbing heterogeneity at that point. The left half of Figure 19 (-17.5 to 0 mm) shows a more distinct separation of spectrally resolved distinct reflectance spectra relative to the right half (0 to -17.5 mm). This



observation is consistent with the fact that the spectral variation of arterial optical properties (left) is larger than that of bile (right).

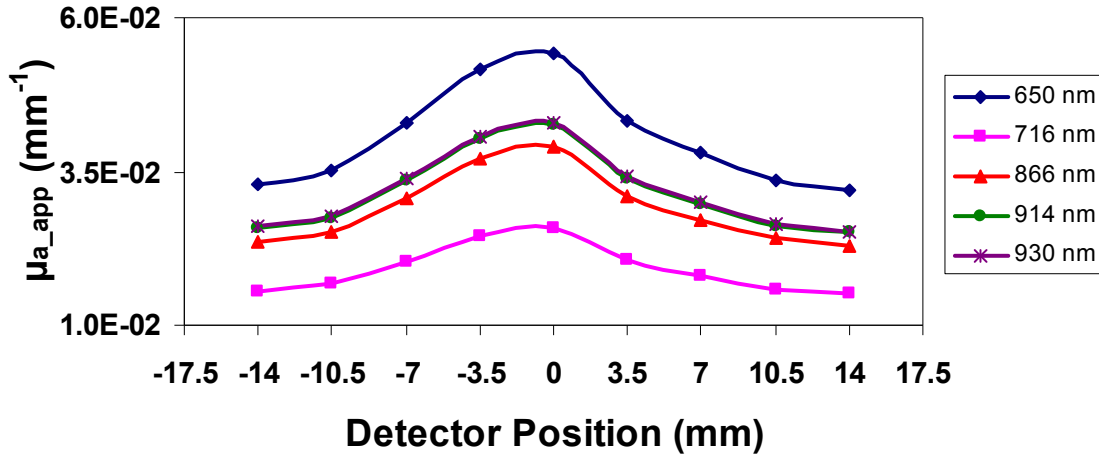


Figure 20: Plot of spectrally resolved arterial  $\mu_{a\_app}$  for fatty tissue containing two absorbing heterogeneities (artery and bile duct) separated by a center-to-center distance of 7 mm. The reflectance contribution from all 13 sources was added to each detector and the fit uses absolute reflectance data. Both the arterial and bile absorption coefficients were varied in each fit simultaneously.

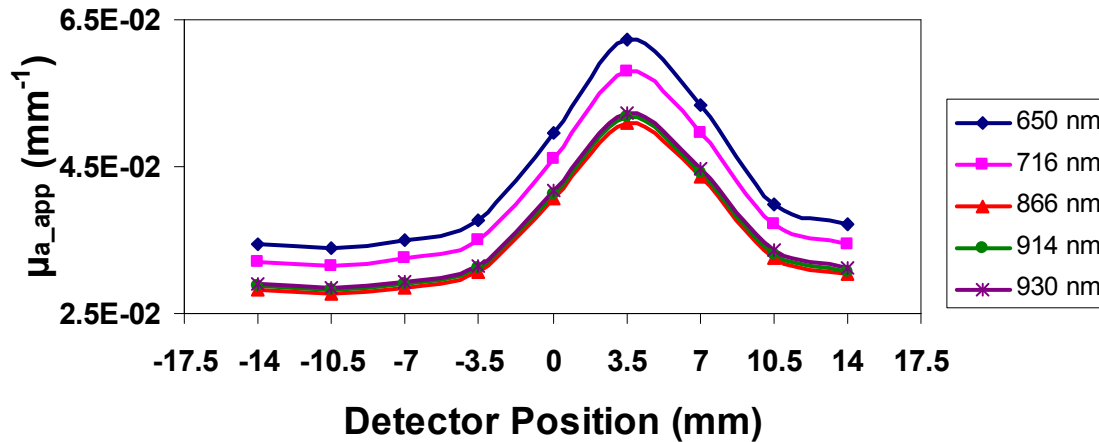


Figure 21: Plot of spectrally resolved bile  $\mu_{a\_app}$  for fatty tissue containing two absorbing heterogeneities (artery and bile duct) separated by a center-to-center distance of 7 mm. The reflectance contribution from all 13 sources was added to each detector and the fit used absolute reflectance data. Both the arterial and bile absorption coefficients were varied in each fit simultaneously.

The  $\mu_{a\_app}$  obtained by fitting reflectance data (Figure 19) is shown in Figures 20 and 21 for the arterial and bile absorption contributions, respectively, where these absorbing heterogeneities were separated by a center-to-center distance of 7 mm. As seen in Figure 20 the point of maximum absorption is at 0 mm indicating the presence of the artery center at that point.

In Figure 20 the point of maximum absorption is at 3.5 mm indicating the presence of the bile duct center at that point. Comparing the deduced artery location in Figure 20 (center at ~1 mm) versus Figure 10 (center at -3.5 mm) we see that the presence of an additional absorption heterogeneity (bile duct) in the vicinity of the artery has affected its localization by a few mm.

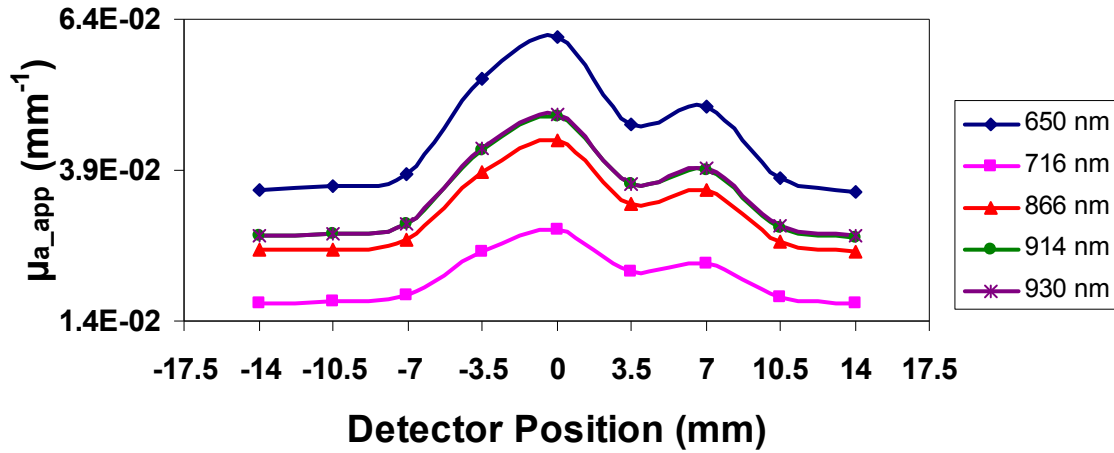


Figure 22: Plot of spectrally resolved arterial  $\mu_{a\_app}$  for fatty tissue containing two absorbing heterogeneities (artery and bile duct) separated by a center-to-center distance of 7 mm. The reflectance contribution from only one source-detector pair at 3.5 mm separation was considered and the fit used absolute reflectance data. Both the arterial and bile absorption coefficients were varied in each fit simultaneously.

The  $\mu_{a\_app}$  obtained by fitting reflectance data for a moving single source-detector pair along the tissue surface is shown in Figures 22 and 23. In Figure 22 the plot of arterial  $\mu_{a\_app}$  for a single source-detector pair at 3.5 mm separation, moving along tissue surface. The point of maximum absorption is observed at 0 mm, which is shifted from the true location of the absorbing heterogeneity (artery, -3.5 mm). The increase in  $\mu_{a\_app}$  at 7 mm is also seen in Figure 22.

Figure 23 shows the plot for bile  $\mu_{a\_app}$  obtained from a single source-detector pair of 3.5 mm separation, moving along tissue surface. The point of maximum absorption can be seen at 7 mm, shifted from the true location of the absorbing heterogeneity (bile, 3.5 mm). In this instance we see some cross-talk in the  $\mu_{a\_app}$  values for the artery.

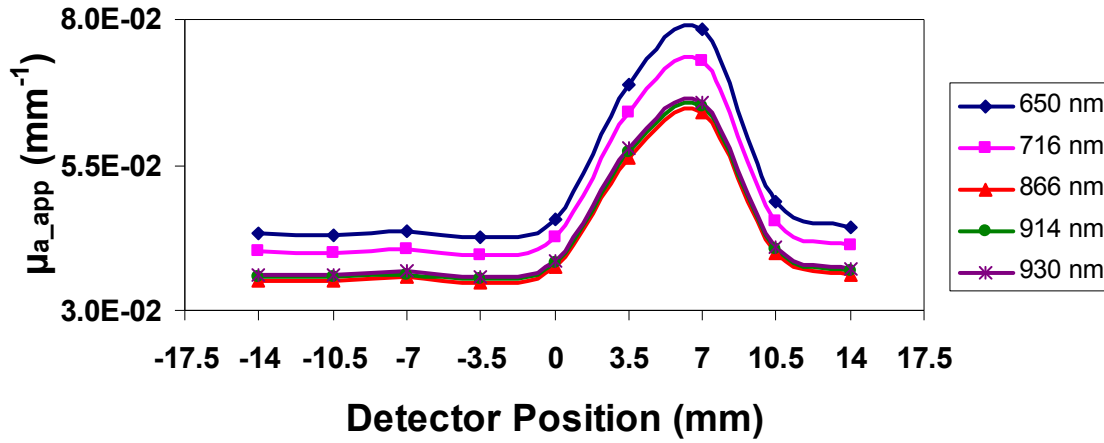


Figure 23: Plot of spectrally resolved bile  $\mu_{a\_app}$  for fatty tissue containing two absorbing heterogeneities (artery and bile duct) separated by a center-to-center distance of 7 mm. The reflectance contribution from only one source-detector pair at 3.5 mm separation was considered and the fit used absolute reflectance data. Both the arterial and bile absorption coefficients were varied in each fit simultaneously.

Figures 24 and 25 show spectrally resolved  $\mu_{a\_app}$  for fatty tissue containing two absorbing heterogeneities (artery and bile) for a source-detector separation of 7 mm. The

point of maximum absorption is shifted from the true location of the absorbing heterogeneities in both figures. In the case of Figure 24, the artery is located at -3.5 mm and the point of maximum absorption is seen at 0 mm.

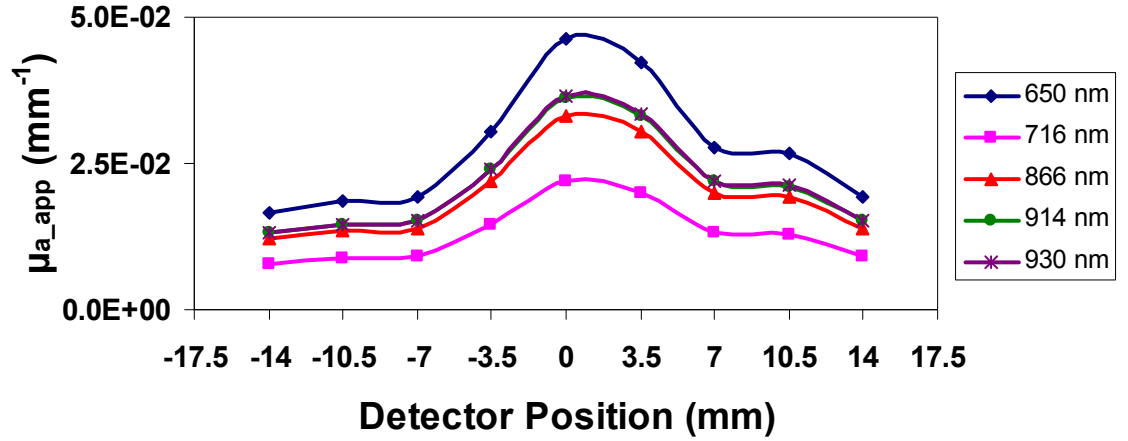


Figure 24: Plot of spectrally resolved arterial  $\mu_{a\_app}$  for fatty tissue containing two absorbing heterogeneities (Artery and Bile) separated by a center-to-center distance of 7 mm. The reflectance contribution from only one source-detector pair at 7 mm separation was considered and the fit used absolute reflectance data. Both the arterial and bile absorption coefficients were varied in each fit simultaneously.

In case of Figure 25, the bile duct is located at 3.5 mm and the point of maximum absorption is seen at 7 mm. As discussed for the case of a single absorbing heterogeneity, above, use of a single source-detector separation induces this apparent shift, which however can be corrected by shifting the absorption peak by half the distance between source and detector (3.5 mm in this case).

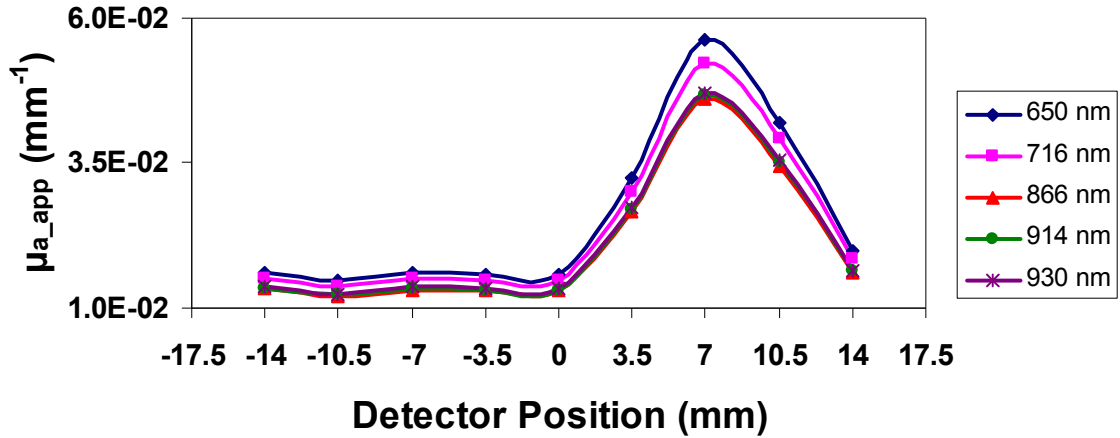


Figure 25: Plot of spectrally resolved bile  $\mu_{a\_app}$  for fatty tissue containing two absorbing heterogeneities (artery and bile duct) separated by a center-to-center distance of 7 mm. The reflectance contribution from only one source-detector pair of 7 mm separation was considered and the fit used absolute reflectance data. Both the arterial and bile absorption coefficients were varied in each fit simultaneously.

#### 3.1.4 Lateral Localization of Two Absorbing Heterogeneities (Artery and Bile Duct) Adjacent to Each Other

The spectrally resolved MC reflectance from fatty tissue containing two absorbing heterogeneities is shown in Figure 26. The simulated tissue geometry contains two absorbing heterogeneities having optical properties of artery and bile and laterally located at -1 mm and 2 mm, respectively. As artery and bile duct have diameters of 2 mm and 4 mm, respectively, they will now be exactly adjacent to each other. In these simulated reflectance measurements the reflectance contribution from all the sources was added to each detector.

As seen from in Figure 26 the point of minimum reflectance is at 0 mm. The reflectance spectra of the two heterogeneities thus appear to be overlapped making it difficult to distinguish between them even though the higher spectral separation between

curves to the left of the graph gives an indication that there may be more than one heterogeneity within the probed tissue volume.

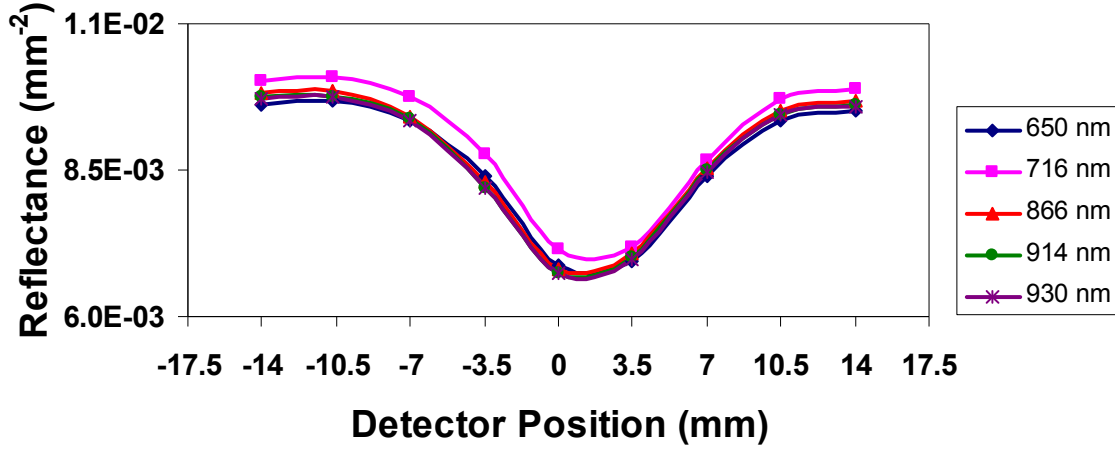


Figure 26: Spectrally resolved reflectance from fatty tissue containing two absorbing heterogeneities with optical properties of arterial blood and human bile, centered at -1 mm and 2 mm respectively. Tissue optical properties are plotted in Figures 6 and 7.

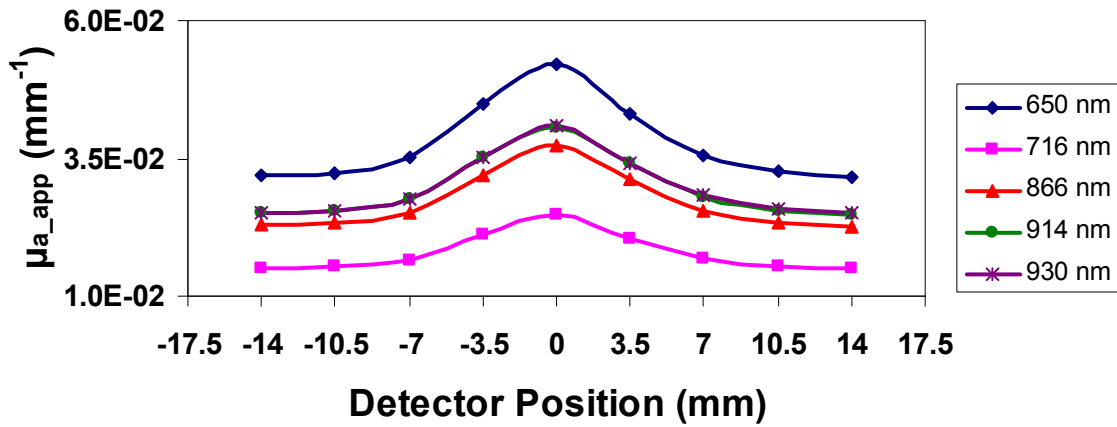


Figure 27: Plot of spectrally resolved arterial  $\mu_{a\_app}$  for fatty tissue containing two absorbing heterogeneities (artery and bile duct) adjacent to each other. The reflectance contribution from all 13 sources was added to each detector and the fit used absolute reflectance data. Both the arterial and bile absorption coefficients were varied in each fit simultaneously.

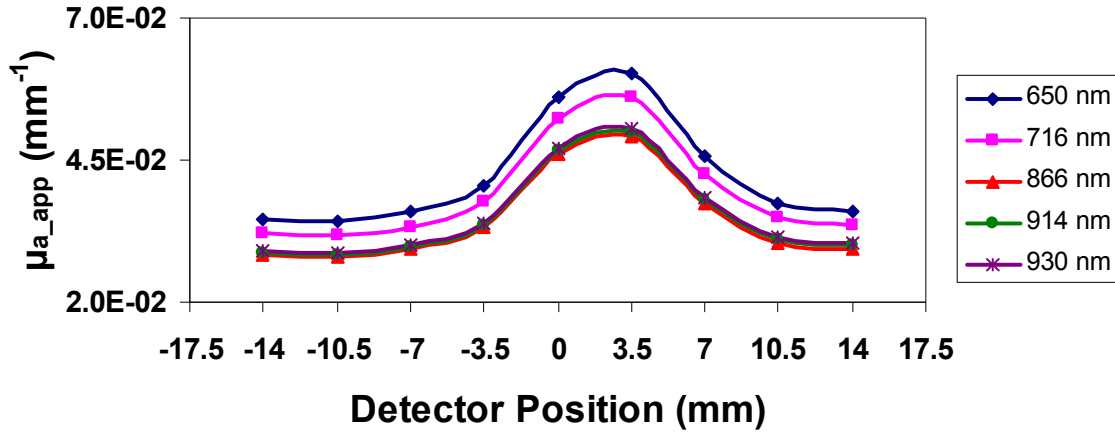


Figure 28: Plot of spectrally resolved bile  $\mu_{a\_app}$  for fatty tissue containing two absorbing heterogeneities (artery and bile duct) placed adjacent to each other. The reflectance contribution from all 13 sources was added to each detector and the fit used absolute reflectance data. Both the arterial and bile absorption coefficients were varied in each fit simultaneously.

Figures 27 and 28 show  $\mu_{a\_app}$  for spectrally resolved reflectance measurements on fatty tissue containing two absorbing heterogeneities (artery and bile) placed exactly adjacent to each other. In Figure 27 the arterial  $\mu_{a\_app}$  value is plotted for each detector position. As seen from Figure 27 the point of maximum absorption is at 0 mm, which is slightly shifted from the true location of the artery (-1 mm). In Figure 28 the bile  $\mu_{a\_app}$  value is plotted for each detector position. In this case the point of maximum absorption is at ~3 mm, which is slightly shifted from the true location of the absorbing heterogeneity (2 mm).

Comparison of Figures 27 and 28 with Figure 26 indicates that despite the high spatial overlap seeing in the reflectance profiles of neighboring absorption heterogeneities, processing of that data with the semi-infinite medium model results in good spatial separation between the artery and bile duct locations. In addition, the

difference between arterial and bile absorbance spectra is reflected in the  $\mu_{a\_app}$  profiles for arterial blood and bile: the relative magnitude of absorption at 716 nm and 930 nm is swapped between Figures 27 and 28.

Figures 29 and 30 show  $\mu_{a\_app}$  for spectrally resolved reflectance measurements on fatty tissue containing two absorbing heterogeneities (artery and bile) placed exactly adjacent to each other. The single source-detector pair at 3.5 mm separation was moved along the tissue surface. Figure 29 shows the arterial  $\mu_{a\_app}$  with point of maximum absorption at 3.5 mm, which is shifted from the true location (-1 mm) of artery. Figure 30 shows the bile  $\mu_{a\_app}$  with point of maximum absorption at 3.5 mm, which is shifted from the true location (-2 mm) of the bile duct.

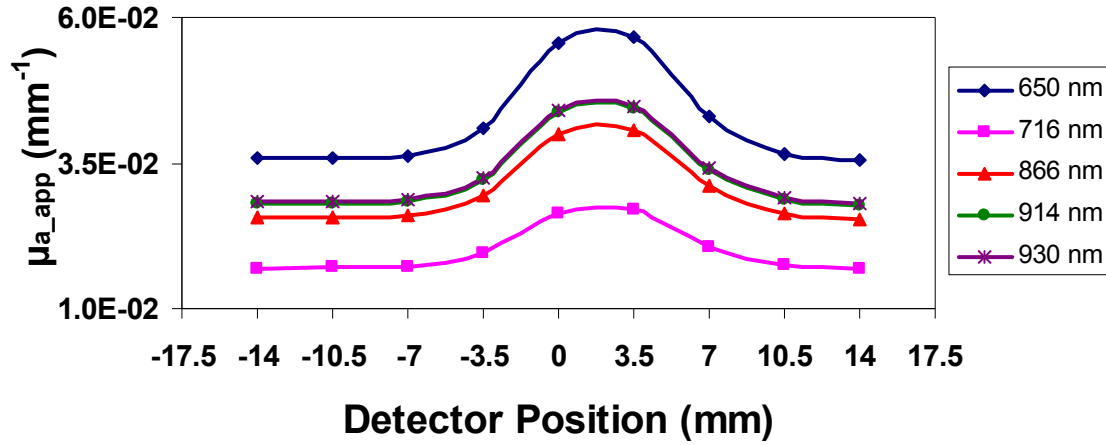


Figure 29: Plot of spectrally resolved arterial  $\mu_{a\_app}$  for fatty tissue containing two absorbing heterogeneities (artery and bile duct) placed adjacent to each other. The reflectance contribution from only one source-detector pair at 3.5 mm separation was considered and the fit used absolute reflectance data. Both the arterial and bile absorption coefficients were varied in each fit simultaneously.



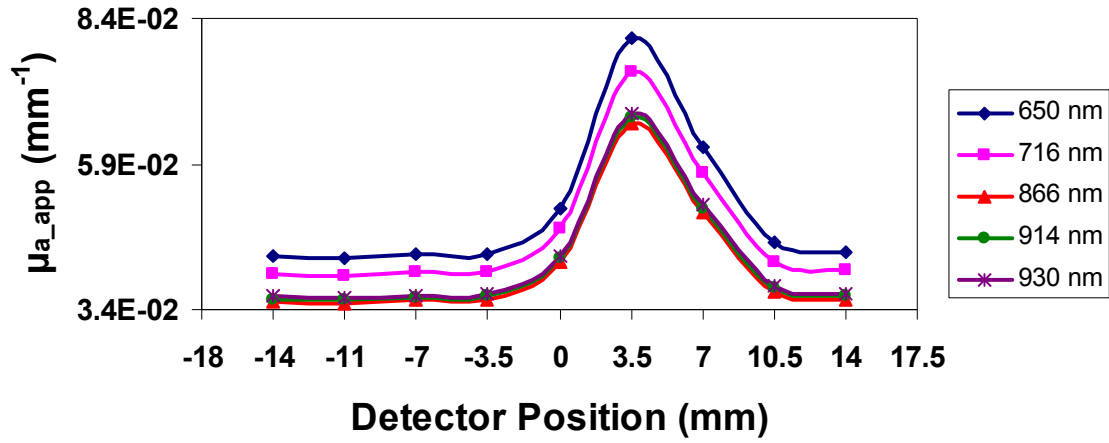


Figure 30: Plot of spectrally resolved bile  $\mu_{a\_app}$  for fatty tissue containing two absorbing heterogeneities (artery and bile duct) placed adjacent to each other. The reflectance contribution from only one source-detector pair at 3.5 mm separation was considered and the fit used absolute reflectance data. Both the arterial and bile absorption coefficients were varied in each fit simultaneously.

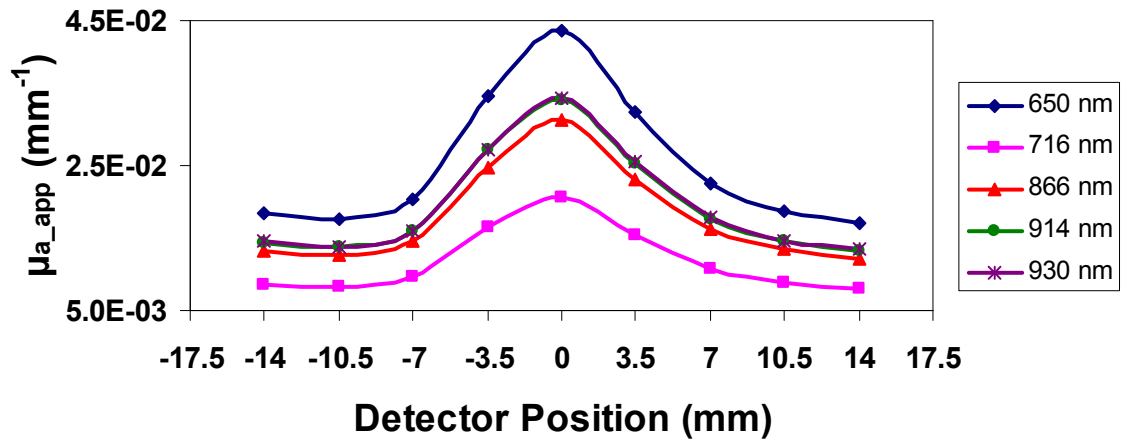


Figure 31: Plot of spectrally resolved arterial  $\mu_{a\_app}$  for fatty tissue containing two absorbing heterogeneities (artery and bile duct) placed adjacent to each other. The reflectance contribution from only one source-detector pair of 7 mm separation was considered and the fit used absolute reflectance data. Both the arterial and bile absorption coefficients were varied in each fit simultaneously.

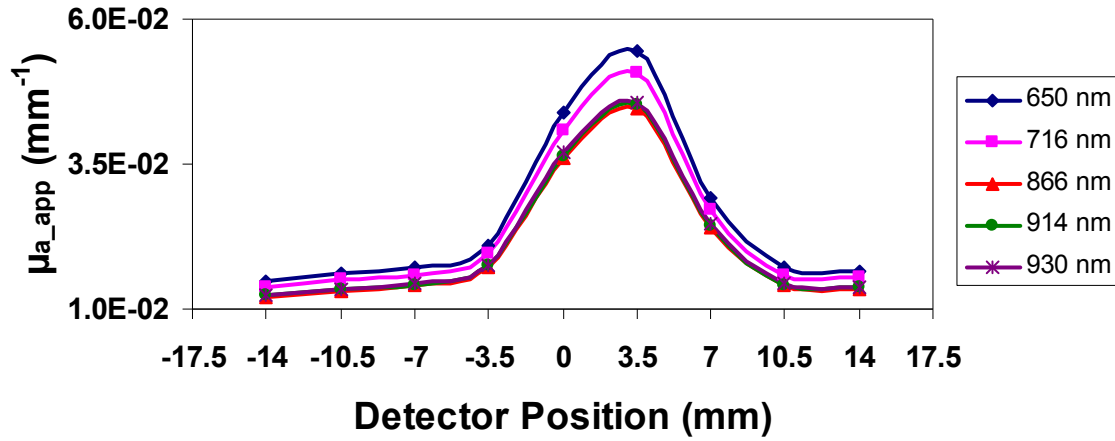


Figure 32: Plot of spectrally resolved bile  $\mu_{a\_app}$  for fatty tissue containing two absorbing heterogeneities (artery and bile duct) placed adjacent to each other. The reflectance contribution from only one source-detector pair at a 7 mm separation was considered and the fit used absolute reflectance data. Both the arterial and bile absorption coefficients were varied in each fit simultaneously.

Figures 31 and 32 show  $\mu_{a\_app}$  for spectrally resolved reflectance measurements performed at a source-detector separation of 7 mm on fatty tissue containing two absorbing heterogeneities (artery and bile duct). The point of maximum absorption is shifted from the true location of the absorbing heterogeneities in both Figures. In the case of Figure 31, the absorption heterogeneity is located at -1 mm and the point of maximum absorption is seen at 0 mm. In case of Figure 32, the absorption heterogeneity is located at 2 mm and the point of maximum absorption is seen at 3.5 mm.

### 3.1.5 Lateral Localization of Two Absorbing Heterogeneities Adjacent to Each Other (Artery and Bile Duct) in the Presence of an Underlying Vein

In Figure 34 the spectrally resolved MC reflectance from fatty tissue containing three absorbing heterogeneities is shown (see Figure 33 for their relative placement)

having optical properties of arterial and venous blood and bile. The artery and bile duct were laterally located at -1 mm and 2 mm, respectively, and were thus exactly adjacent to each other. The vein is laterally centered at 2 mm and at depth of 11 mm from the surface. The artery, bile duct and vein have diameters of 2 mm, 4 mm and 10 mm, respectively.

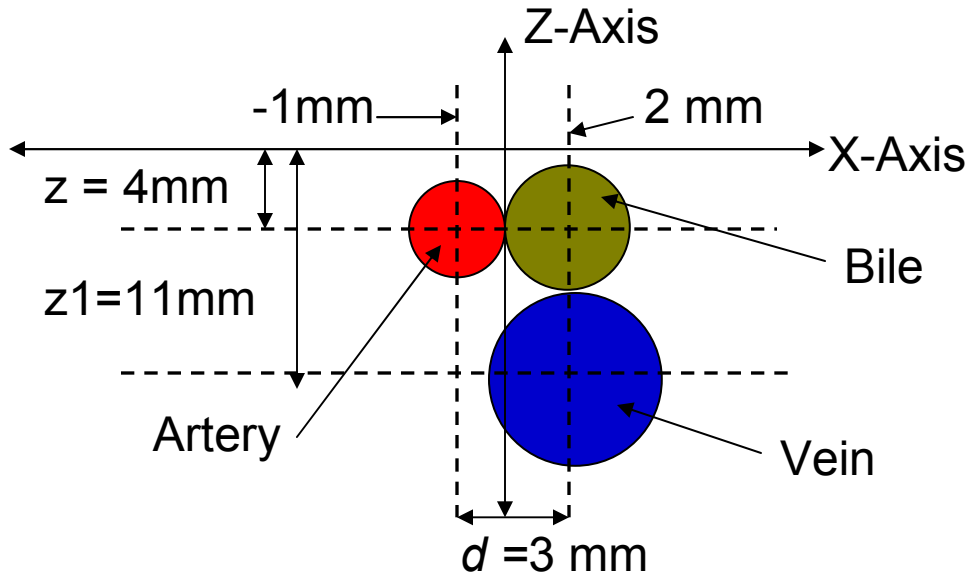


Figure 33: Location of three absorbing heterogeneities in the simulated tissue geometry.

In the simulated measurements the reflectance contributions from all the sources were added to each detector. As seen in Figure 34 the point of minimum reflectance occurs between 0 mm and 3.5 mm and the reflectance spectra contributions from the heterogeneities are highly overlapped, making it difficult to deduce their actual locations.

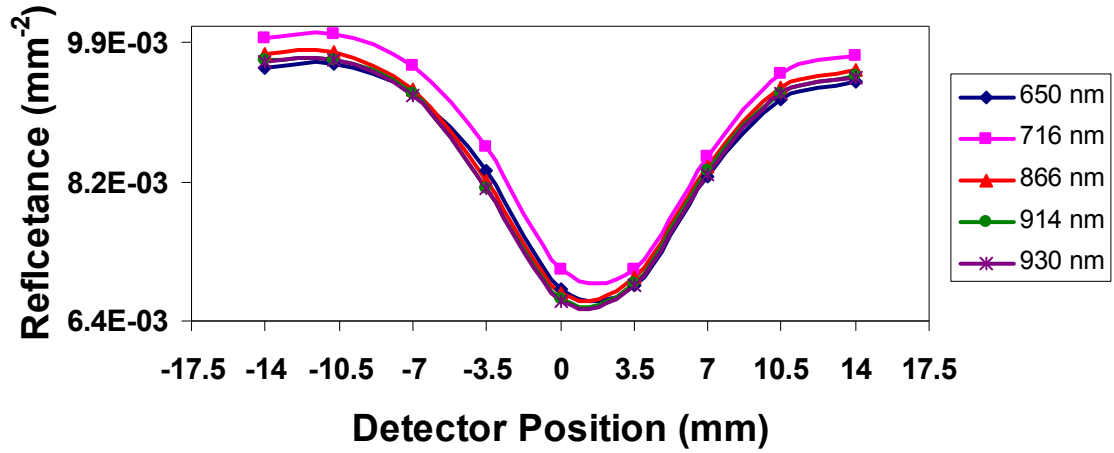


Figure 34: Spectrally resolved reflectance from fatty tissue containing three absorbing heterogeneities with optical properties of arterial blood, human bile venous blood. Tissue optical properties are plotted in Figures 6 and 7.

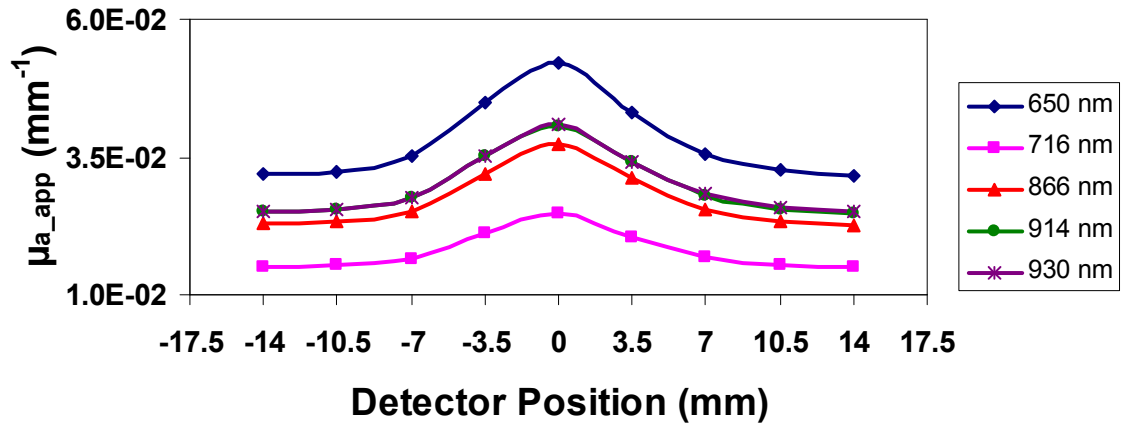


Figure 35: Plot of spectrally resolved arterial  $\mu_{a\_app}$  for fatty tissue containing three absorbing heterogeneities. Two absorbing heterogeneities (artery and bile duct) are adjacent to each other and the third one (vein) was placed immediately beneath the bile duct. The reflectance contributions from all 13 sources were added to each detector and the fit used absolute reflectance data. Both the arterial and bile absorption coefficients were varied in each fit simultaneously.

Figures 35 and 36 show the spatial variation of  $\mu_{a\_app}$  for fatty tissue containing three absorbing heterogeneities (artery, bile duct and vein). In Figure 35 the arterial  $\mu_{a\_app}$  is plotted for each detector position. As seen in Figure 35 the point of maximum absorption is at 0 mm, which is slightly shifted from the true location of the artery (-1 mm). In Figure 36 the bile  $\mu_{a\_app}$  is plotted for each detector position. In that case, the point of maximum absorption is at 3.5 mm which is slightly shifted from the true location of the bile duct (2 mm).

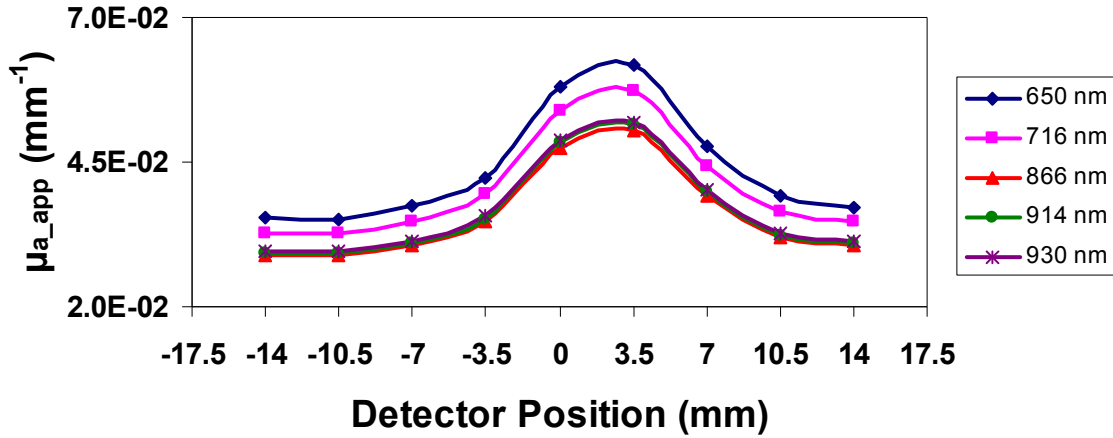


Figure 36: Plot of spectrally resolved bile  $\mu_{a\_app}$  for fatty tissue containing three absorbing heterogeneities. Two absorbing heterogeneities (artery and bile duct) are adjacent to each other and the third one (vein) was placed immediately beneath the bile duct. The reflectance contributions from all 13 sources were added to each detector and the fit used absolute reflectance data. Both the arterial and bile absorption coefficients were varied in each fit simultaneously.

Figures 37 and 38 show the spatial variation of  $\mu_{a\_app}$  for fatty tissue containing three absorbing heterogeneities. A single source-detector pair at 3.5 mm separation was moved along the tissue surface. Figures 37 and 38 show the arterial and bile  $\mu_{a\_app}$ ,

respectively. In both the figures the point of maximum absorption is shifted from the true location of the corresponding absorbing heterogeneity.

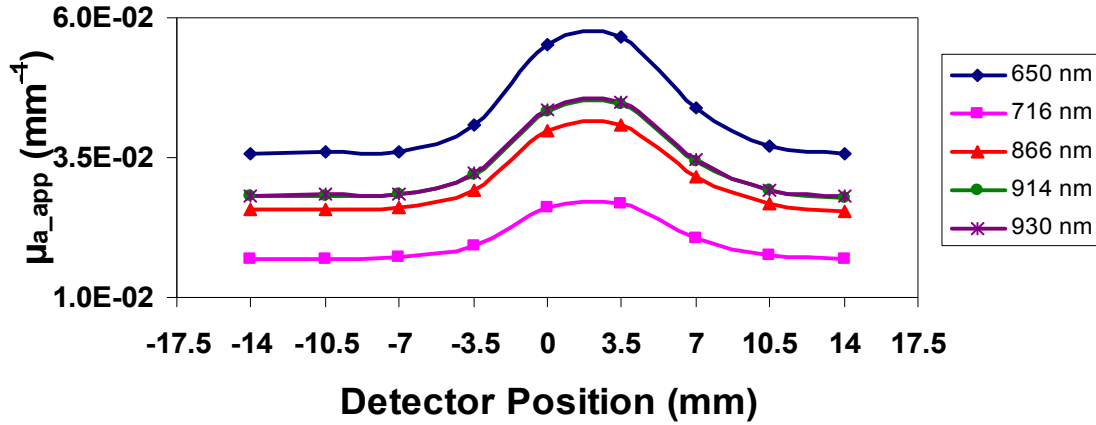


Figure 37: Plot of spectrally resolved arterial  $\mu_{a\_app}$  for fatty tissue containing three absorbing heterogeneities. Two absorbing heterogeneities (artery and bile duct) are adjacent to each other and the third one (vein) was placed immediately beneath the bile duct. The reflectance contribution from only one source-detector pair at 3.5 mm separation was considered and the fit used absolute reflectance data. Both the arterial and bile absorption coefficients were varied in each fit simultaneously.

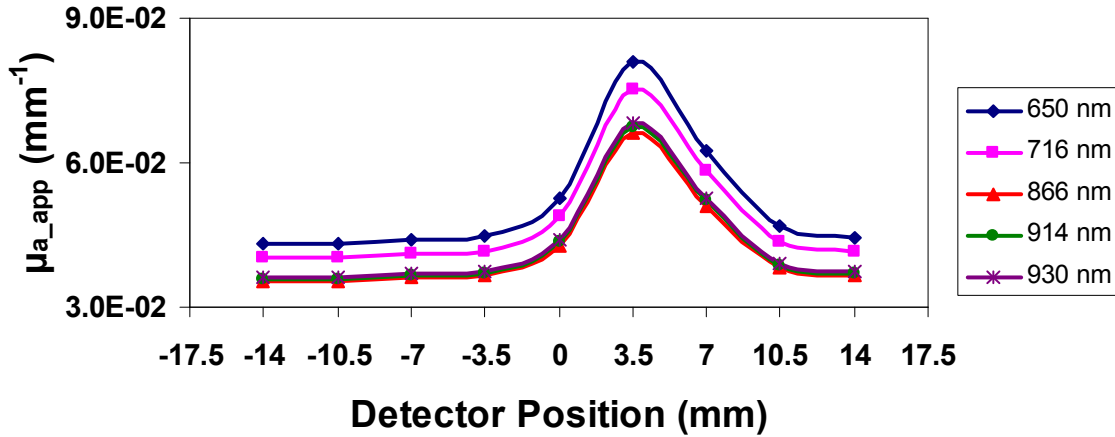


Figure 38: Plot of spectrally resolved bile  $\mu_{a\_app}$  for fatty tissue containing three absorbing heterogeneities. Two absorbing heterogeneities (artery and bile duct) are adjacent to each other and the third one (vein) was placed immediately beneath the bile duct. The reflectance contribution from only one source-detector pair at 3.5 mm separation was considered and the fit used absolute reflectance data. Both the arterial and bile absorption coefficients were varied in each fit simultaneously.

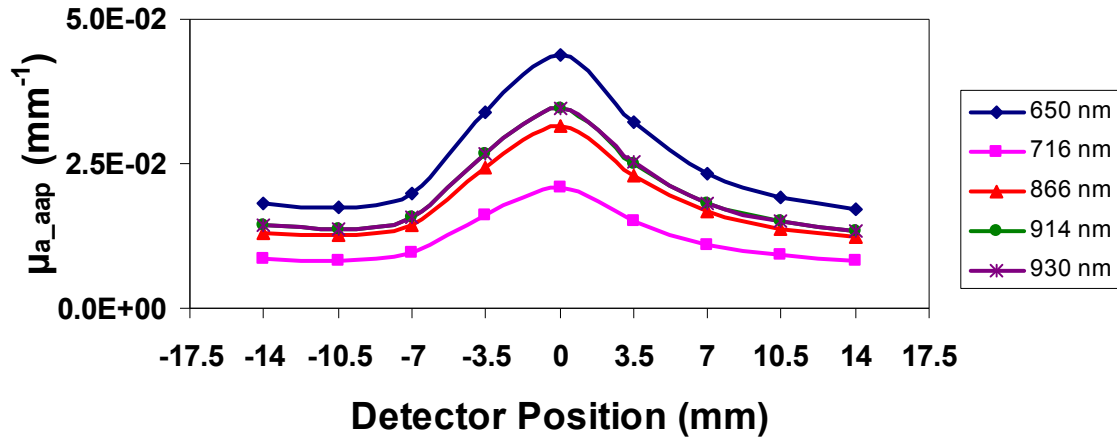


Figure 39: Plot of spectrally resolved arterial  $\mu_{a\_app}$  for fatty tissue containing three absorbing heterogeneities. Two absorbing heterogeneities (artery and bile duct) are adjacent to each other and the third one (vein) was placed immediately beneath the bile duct. The reflectance contribution from only one source-detector pair at 7 mm separation was considered and the fit used absolute reflectance data.

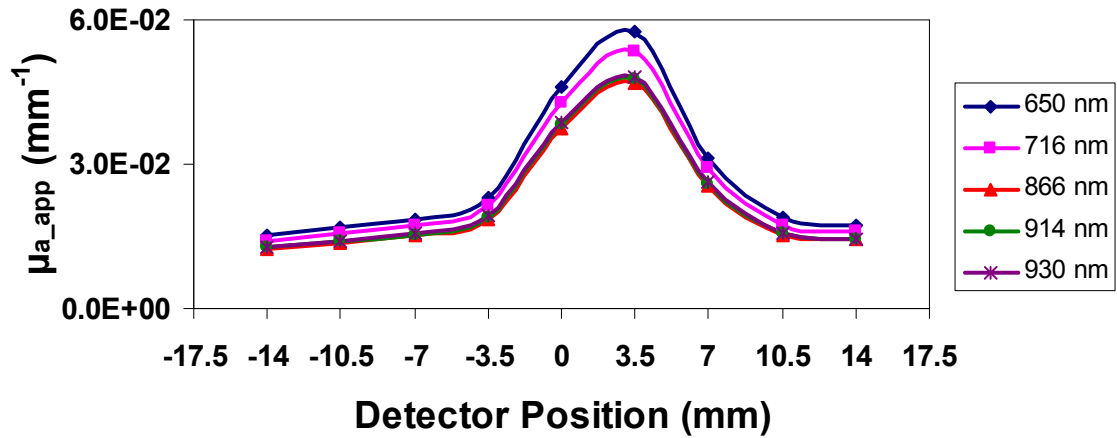


Figure 40: Plot of spectrally resolved bile  $\mu_{a\_app}$  for fatty tissue containing three absorbing heterogeneities. Two absorbing heterogeneities (artery and bile duct) are adjacent to each other and the third one (vein) was placed immediately beneath the bile duct. The reflectance contribution from only one source-detector pair at 7 mm separation was considered and the fit used absolute reflectance data.

Figures 39 and 40 show the spectrally resolved  $\mu_{a\_app}$  for fatty tissue containing three absorbing heterogeneities (artery and bile duct) for a source-detector separation of 7 mm. The point of maximum absorption is shifted from the true location of the absorbing heterogeneities in both Figures. In case of Figure 39, the absorption heterogeneity is located at -1 mm and the point of maximum absorption is seen at 0 mm. In case of Figure 40, the absorption heterogeneity is located at 2 mm and the point of maximum absorption is seen at 3.5 mm.

### 3.2 Depth Localization of Absorbing Heterogeneities

#### 3.2.1 Depth Localization of a Single Absorbing Heterogeneity (Artery)

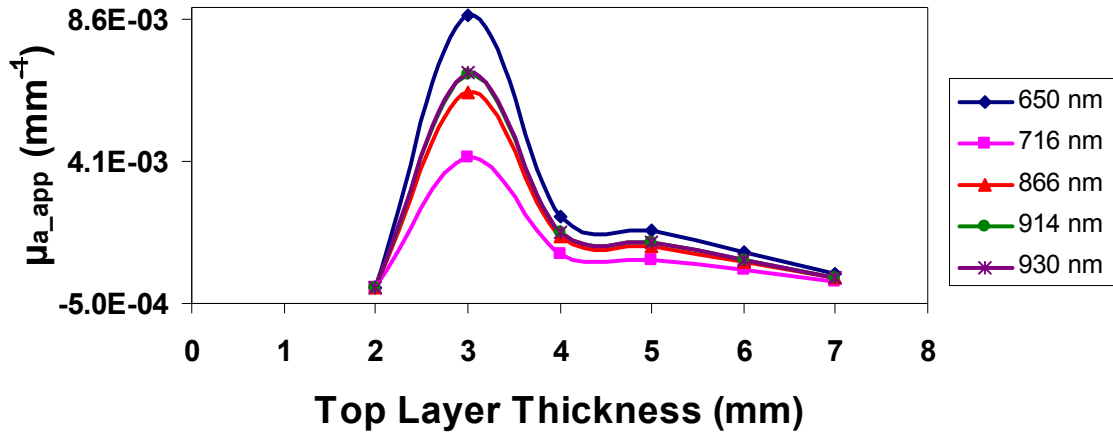


Figure 41: Depth-wise arterial  $\mu_{a\_app}$  for a detector placed on the peak absorption surface location. Tissue geometry consisted of a single absorbing heterogeneity (artery centered at 4 mm depth); all sources were added to a single detector, reflectance data fitting was relative; only the arterial absorption of the top and bottom layers was varied in each fit.

Figure 41 shows the depth-wise arterial  $\mu_{a\_app}$  for tissue containing an absorbing heterogeneity (artery) of 2mm diameter centered at depth of 4 mm (please refer to artery position in Figure 8 for relative placement). Depth-wise scanning was done for the



detector placed on the peak absorption surface location and  $\mu_{a\_app}$  is plotted for increasing top layer thicknesses. As seen from the figure the point of maximum absorption is at a top layer thickness of 3 mm indicating the presence of an absorbing heterogeneity at that thickness. The peak observed for a top layer thickness of 3 mm provides an estimate for the top surface of the artery. A top layer thickness of 1 mm is not taken into consideration as the diffusion approximation does not hold true for such a small layer thickness. Moreover, probing such a less thickness is not of significance in our application as very superficial heterogeneities can be seen with unaided eye.

### 3.2.2 Depth Localization of a Single Absorbing Heterogeneity (Bile Duct)

Figure 42 shows the depth-wise bile  $\mu_{a\_app}$  for tissue containing an absorbing heterogeneity (bile duct) of 2 mm diameter centered at depth of 4 mm (please refer to bile duct position in Figure 8 for relative placements). Depth-wise scanning was done for the detector placed on the peak absorption surface location and  $\mu_{a\_app}$  is plotted for increasing top layer thicknesses. As seen from the Figure the point of maximum absorption is attained for a top layer thickness of 2 mm indicating the presence of an absorbing heterogeneity at that thickness. Therefore the top layer thickness of 2 mm provides a depth estimate for the top surface of the bile duct.

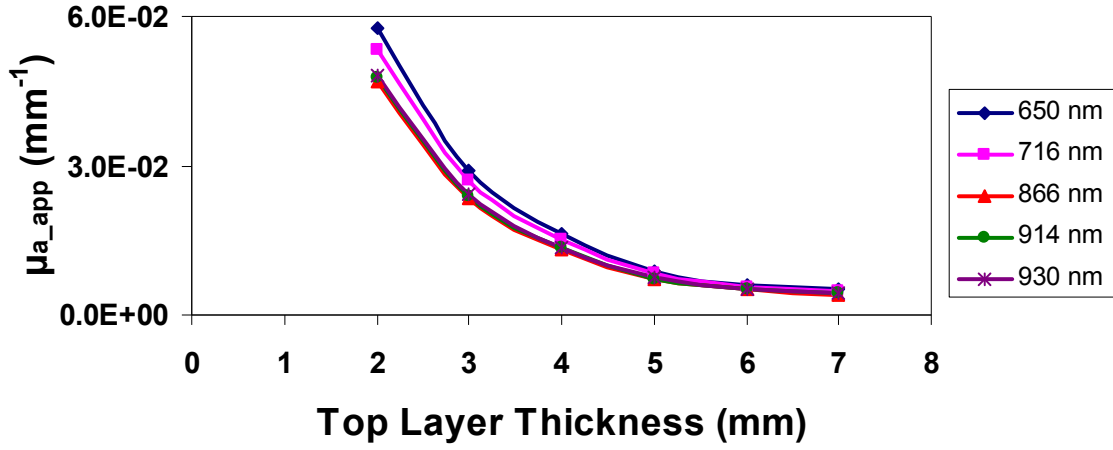


Figure 42: Depth-wise bile  $\mu_{a\_app}$  for a detector placed on the peak absorption surface location. Tissue geometry consisted of two absorbing heterogeneities (bile duct centered at 4 mm depth); all sources were added to a single detector, reflectance data fitting was relative; only the arterial absorption of the top and bottom layers was varied in each fit.

### 3.2.3 Depth Localization of Two Absorbing Heterogeneities (Artery and Bile Duct) Separated by 7 mm (Center -to -Center)

Figure 43 shows the depth-wise arterial  $\mu_{a\_app}$  for tissue containing two absorbing heterogeneities (artery and bile duct) centered at depth of 4 mm having diameters of 2 mm and 4 mm, respectively (please refer to Figure 8 for their relative placement). The spectrally - resolved reflectance data was fitted independently for each absorbing heterogeneity. While localizing artery in depth the bile absorption was set to zero. As seen from the Figure the point of maximum absorption is at a top layer thickness of 4 mm indicating the presence of absorbing heterogeneity at that thickness. Comparing the deduced artery location in Figure 41 (point of maximum absorption at 3 mm) versus Figure 43 (point of maximum absorption at 4 mm) we see that the presence of an

additional absorption heterogeneity (bile duct) in the vicinity of the artery has affected its localization by a few mm.

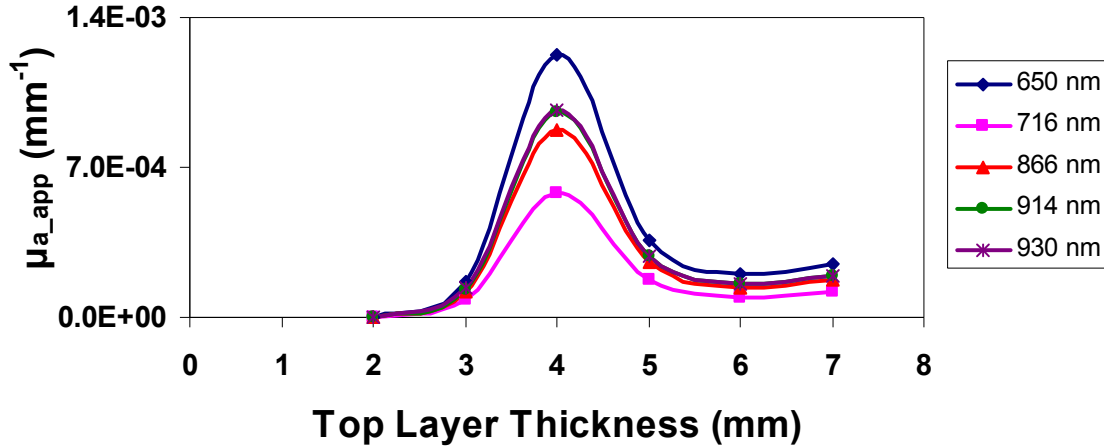


Figure 43: Depth-wise arterial  $\mu_{a\_app}$  for a detector placed on the peak absorption surface location. Tissue geometry consisted of two absorbing heterogeneities (artery and bile duct both centered at 4 mm depth, center-to-center distance 7 mm); all sources were added to a single detector, reflectance data fitting was relative; only the arterial absorption of the top and bottom layers was varied in each fit.

Depth-wise bile  $\mu_{a\_app}$  is plotted in Figure 44. The tissue geometry consists of two absorbing heterogeneities (artery and bile duct) of dimensions and positions shown in Figure 8. The spectrally resolved reflectance data was fitted independently for each absorbing heterogeneity. While localizing the bile duct depth-wise, the arterial absorption was set to fatty tissue. As seen from the Figure 44 bile  $\mu_{a\_app}$  follows the same pattern as in Figure 42.

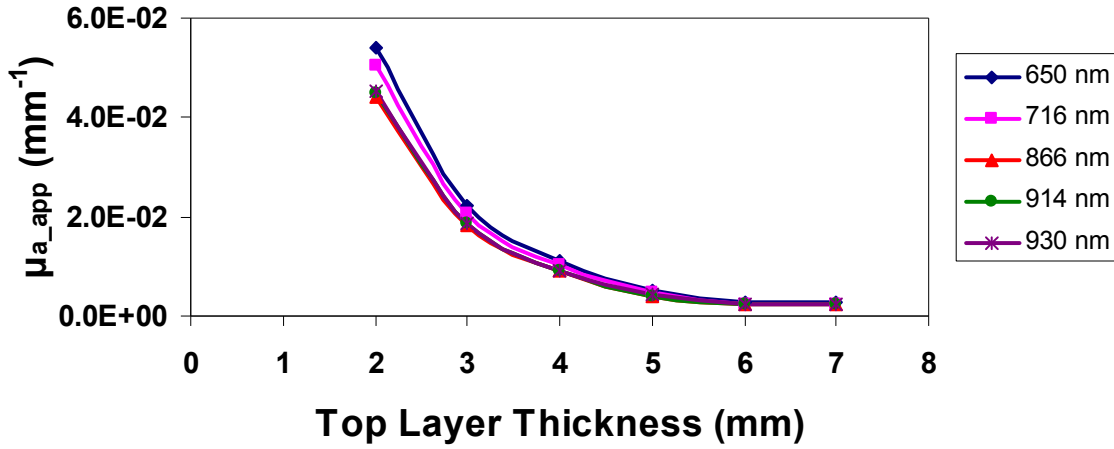


Figure 44: Depth-wise bile  $\mu_{a\_app}$  for a detector placed on the peak absorption surface location. Tissue geometry consisted of two absorbing heterogeneities (artery and bile duct both centered at 4 mm depth, center-to-center distance 7 mm); all sources were added to a single detector, reflectance data fitting was relative; only the arterial absorption of the top and bottom layers was varied in each fit.

#### 3.2.4 Depth Localization of Two Absorbing Heterogeneities (Artery and Bile Duct) Adjacent to Each Other

Figures 45 and 46 show the depth-wise arterial and bile  $\mu_{a\_app}$  for tissue containing two absorbing heterogeneities (artery and bile duct) centered at depth of 4 mm having diameter of 2 mm and 4 mm respectively (please refer to artery position in Figure 33 for relative placement). The  $\mu_{a\_app}$  for each absorbing heterogeneity was obtained by same method described in Section 3.2.3. As seen from Figure 45 the point of maximum absorption is at a top layer thickness of 4 mm indicating the presence of absorbing heterogeneity at that thickness. Comparing Figure 45 and 43 it can be seen that the point of maximum absorption is observed at same top layer thickness i.e. tissue depth.

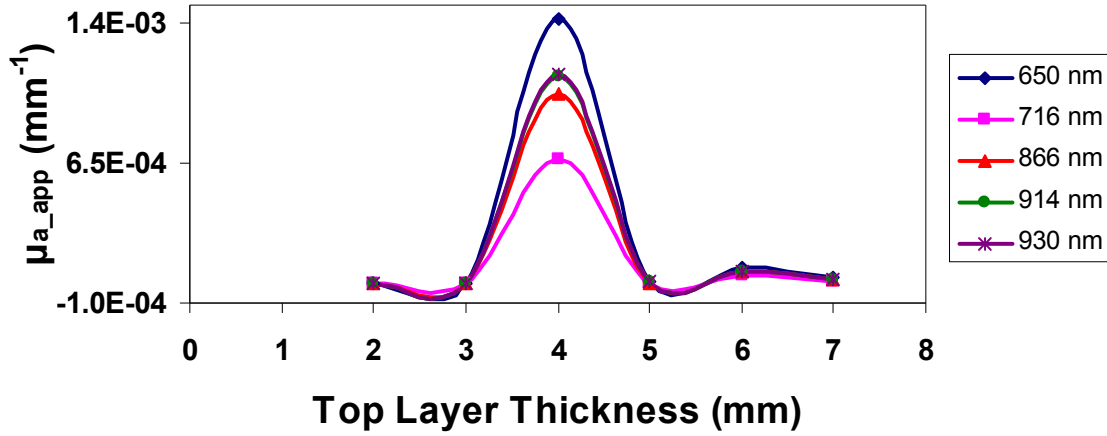


Figure 45: Depth-wise arterial  $\mu_{a\_app}$  for a detector placed on the peak absorption surface location. Tissue geometry consisted of two absorbing heterogeneities (artery and bile duct both centered at 4 mm depth, adjacent to each other, center-to-center distance 3 mm); all sources were added to a single detector, reflectance data fitting was relative; only the arterial absorption of the top and bottom layers was varied in each fit.

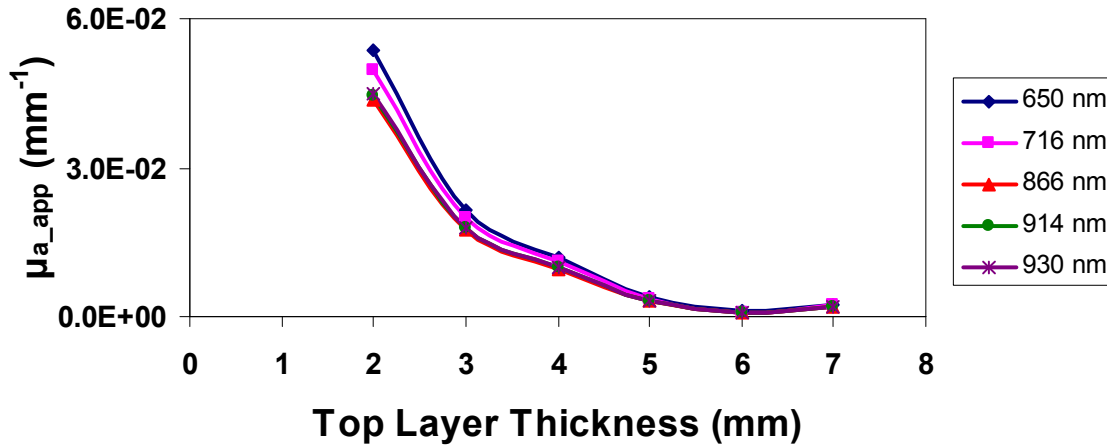


Figure 46: Depth-wise bile  $\mu_{a\_app}$  for a detector placed on the peak absorption surface location. Tissue geometry consisted of two absorbing heterogeneities (artery and bile duct both centered at 4 mm depth, adjacent to each other); all sources were added to a single detector, reflectance data fitting was relative; only the arterial absorption of the top and bottom layers was varied in each fit.

Depth-wise bile  $\mu_{a\_app}$  is plotted in Figure 46. The tissue geometry consists of two absorbing heterogeneities (artery and bile duct) of dimensions and positions shown in Figure 33. The spectrally resolved reflectance data was fitted independently for each absorbing heterogeneity. While localizing the bile duct depth-wise the arterial absorption was set to that of fatty tissue. As seen from the Figure 46 bile  $\mu_{a\_app}$  follows the same pattern as in Figures 42 and 44.

### 3.2.5 Depth Localization of Two Absorbing Heterogeneities Adjacent to Each Other (Artery and Bile Duct) in the presence of an Underlying Vein

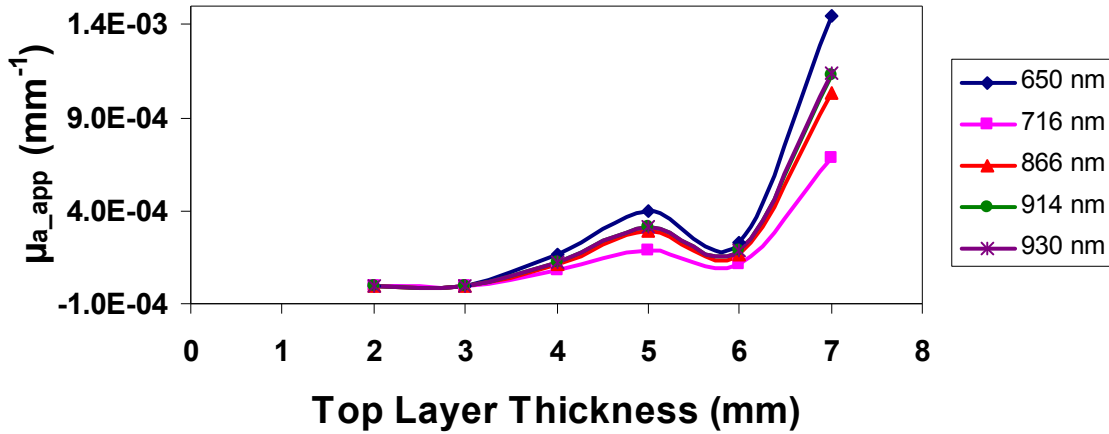


Figure 47: Depth-wise arterial  $\mu_{a\_app}$  for a detector placed on the peak absorption surface location. Tissue geometry consisted of three absorbing heterogeneities (artery and bile duct both centered at 4 mm depth, adjacent to each other. The vein is centered at 8 mm and placed beneath the bile duct); all sources were added to a single detector, reflectance data fitting was relative; only the arterial absorption of the top and bottom layers was varied in each fit.

Figure 47 shows the depth-wise  $\mu_{a\_app}$  for tissue containing three absorbing heterogeneity (artery, bile duct and vein) of diameter 2 mm, 4 mm and 10 mm respectively, centered at depth of 4 mm (please refer to artery position in Figure 33 for relative placement). The  $\mu_{a\_app}$  for each absorbing heterogeneity was obtained by same

method described in Section 3.2.3. Comparing the deduced artery location in Figure 41 (point of maximum absorption at 3 mm), Figure 43 (point of maximum absorption at 4 mm) and Figure 47 (point of maximum absorption at 5 mm) we see the presence of an additional absorption heterogeneity (vein) in the vicinity of the artery has affected its localization by a few mm. In case of Figure 47 the presence of venous blood shows up at top layer thickness of 7 mm.

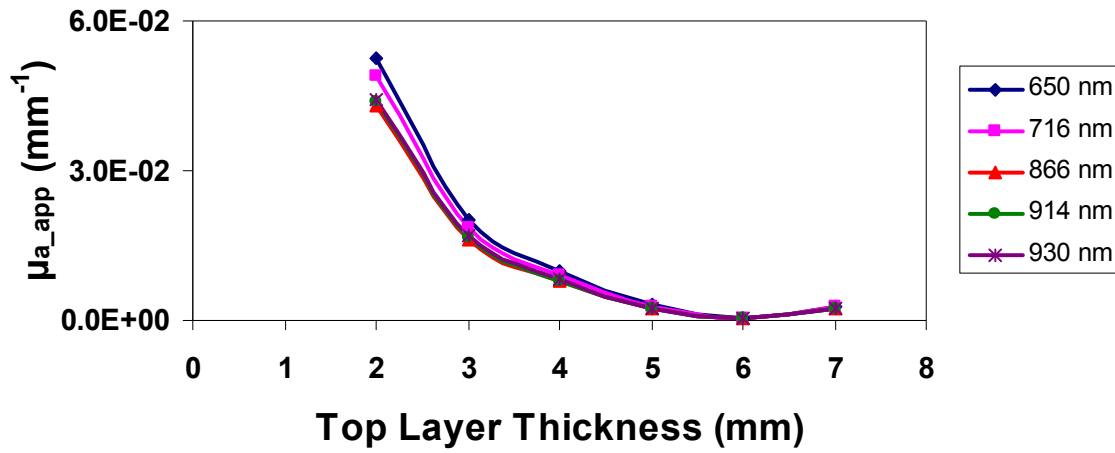


Figure 48: Depth-wise bile  $\mu_{a\_app}$  for a detector placed on the peak absorption surface location. Tissue geometry consisted of three absorbing heterogeneities (artery and bile duct both centered at 4 mm depth, adjacent to each other. The vein is centered at 8 mm and placed beneath bile duct); all sources were added to a single detector, reflectance data fitting was relative; only the arterial absorption of the top and bottom layers was varied in each fit.

The Figure 48 shows depth-wise bile  $\mu_{a\_app}$  for tissue geometry shown in Figure 33. The spectrally resolved reflectance data was fitted independently for each absorbing heterogeneity. While localizing the bile duct depth-wise the arterial absorption was set to fatty tissue. As seen from the Figure 48, bile  $\mu_{a\_app}$  follows the same pattern as in Figures 42, 44, and 46.

### 3.2.6 Comparison of Depth-Wise Apparent Absorption of Heterogeneities (Artery and Bile Duct)

Figure 49 shows the comparison of depth-wise arterial and bile  $\mu_{a\_app}$ . The  $\mu_{a\_app}$  was obtained by fitting spectrally resolved reflectance data for each absorbing heterogeneity (artery and bile duct) independently.

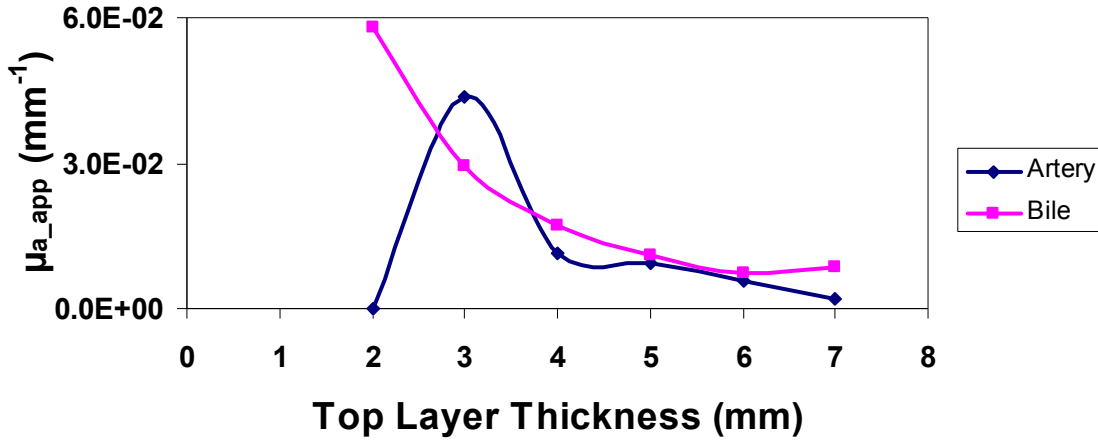


Figure 49: Comparison of dept-wise arterial and bile  $\mu_{a\_app}$ . In contrast to all other simulations artery and bile duct had the same size (2 mm diameter) so that the only difference is the absorption spectrum of the heterogeneity. Arterial  $\mu_{a\_app}$  was scaled by factor of 5 for easier comparison.

In each case, the absorbing heterogeneity was placed at the same location and has the same dimensions (please refer to artery position in Figure 8). In each case, the scattering coefficient was set to that of adipose and the only difference between the two absorbing heterogeneities was their absorption spectrum (please refer Figure 4 and 5). As seen from the figure the point of maximum absorption for artery is at 3 mm and that of bile is at 2 mm. Comparing bile  $\mu_{a\_app}$  profile for all depth localization (Figures 42, 44, 46 and 48) we see that irrespective of the depth and the lateral location of bile duct in tissue geometry, bile  $\mu_{a\_app}$  follows the same decaying pattern.



### 3.3 Analysis of Depth versus Change in Apparent Absorption

#### 3.3.1 Lateral Localization

Figures 50 and 51 show  $\mu_{a\_app}$  for tissue containing two absorbing heterogeneities (artery and bile duct) placed adjacent to each other at depth of 4 mm in fatty tissue. The  $\mu_{a\_app}$  was obtained using the same methods as described in Section 3.1.4. The point of maximum absorption is observed at 0 mm (artery) and 3.5 mm (bile duct) in Figures 50 and 51, respectively.

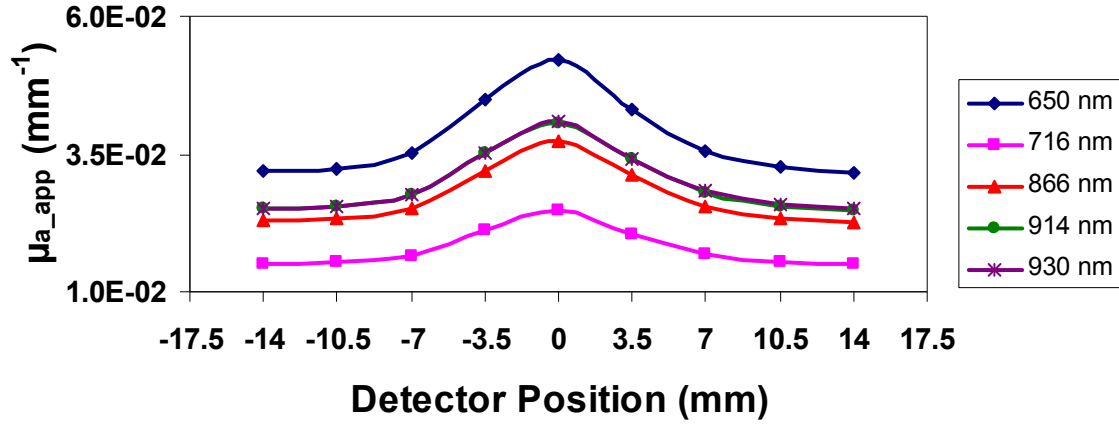


Figure 50: Plot of spectrally resolved arterial  $\mu_{a\_app}$  for fatty tissue containing two absorbing heterogeneities (artery and bile duct) adjacent to each other at depth of 4 mm. The reflectance contributions from all 13 sources were added to each detector and the fit used absolute reflectance data. Both the arterial and bile absorption coefficients were varied in each fit simultaneously.

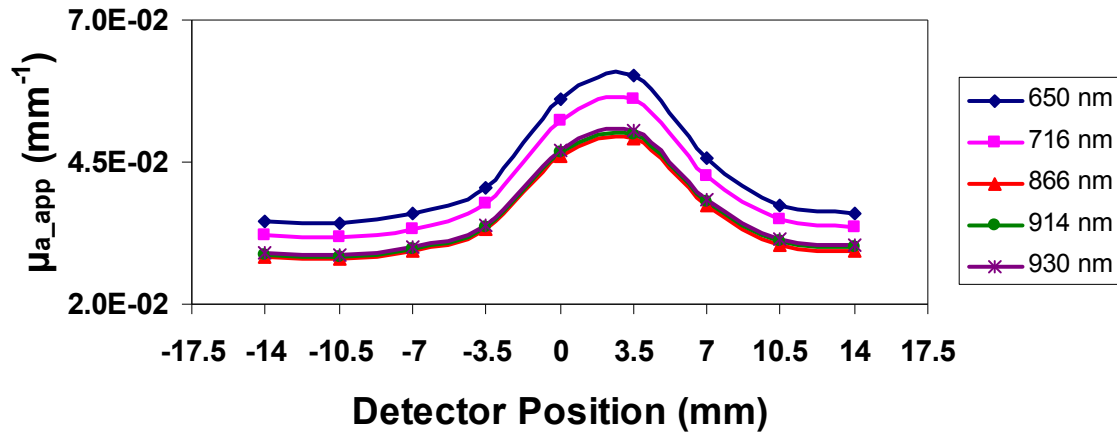


Figure 51: Plot of spectrally resolved bile  $\mu_{a\_app}$  for fatty tissue containing two absorbing heterogeneities (artery and bile duct) adjacent to each other at depth of 4 mm. The reflectance contributions from all 13 sources were added to each detector and the fit used absolute reflectance data. Both the arterial and bile absorption coefficients were varied in each fit simultaneously.

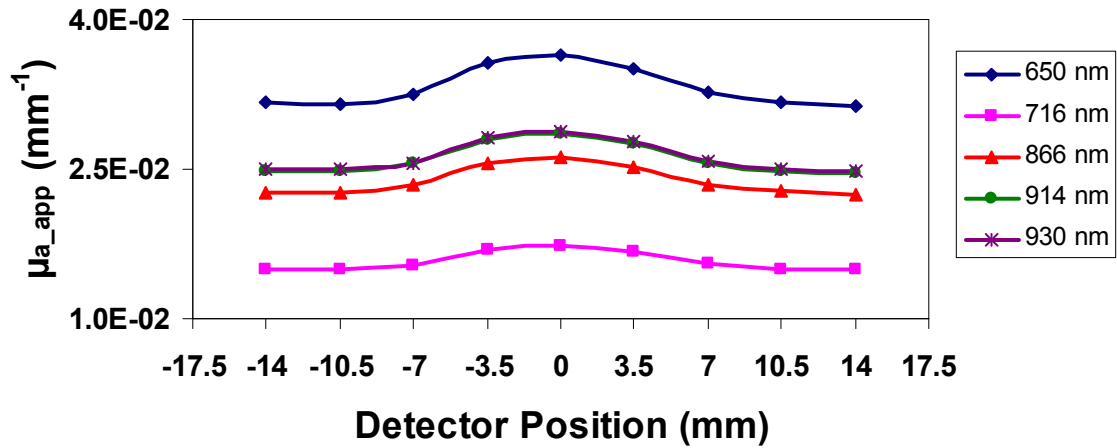


Figure 52: Plot of spectrally resolved arterial  $\mu_{a\_app}$  for fatty tissue containing two absorbing heterogeneities (artery and bile duct) adjacent to each other at depth of 6 mm. The reflectance contributions from all 13 sources were added to each detector and the fit used absolute reflectance data. Both the arterial and bile absorption coefficients were varied in each fit simultaneously.

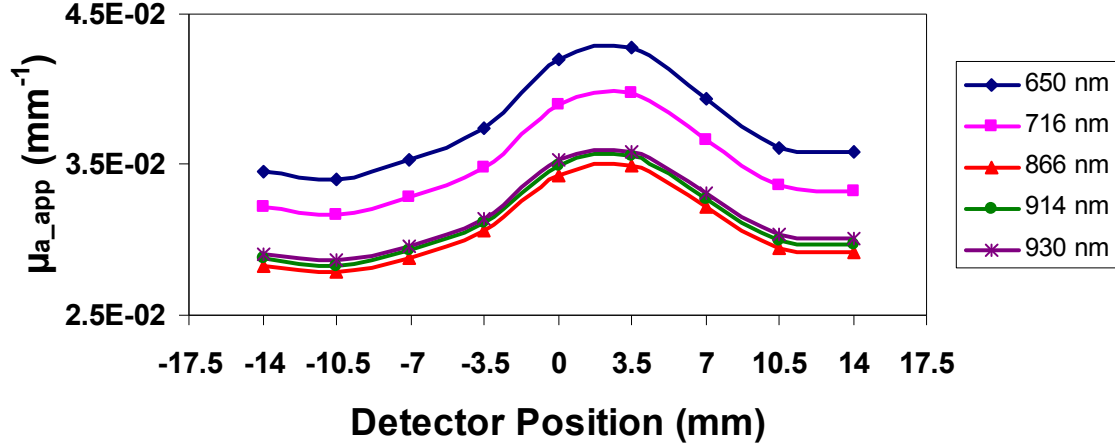


Figure 53: Plot of spectrally resolved bile  $\mu_{a\_app}$  for fatty tissue containing two absorbing heterogeneities (artery and bile duct) adjacent to each other at depth of 6 mm. The reflectance contributions from all 13 sources were added to each detector and the fit used absolute reflectance data. Both the arterial and bile absorption coefficients were varied in each fit simultaneously.

Figures 52 and 53 show the  $\mu_{a\_app}$  for tissue containing two absorbing heterogeneities (artery and bile duct) placed adjacent to each other at depth of 6 mm in fatty tissue. The  $\mu_{a\_app}$  was obtained using same methods as described in Section 3.1.4. The point of maximum absorption is observed at 0 mm (artery) and 3.5 mm (bile duct) in Figures 52 and 53, respectively.

Figures 54 and 55 show the  $\mu_{a\_app}$  for tissue containing two absorbing heterogeneities (artery and bile duct) placed adjacent to each other at depth of 8 mm in fatty tissue. The  $\mu_{a\_app}$  was obtained using the same methods as described in Section 3.1.4. The point of maximum absorption is observed at 0 mm (artery) and 3.5 mm (bile duct) in Figures 54 and 55, respectively.

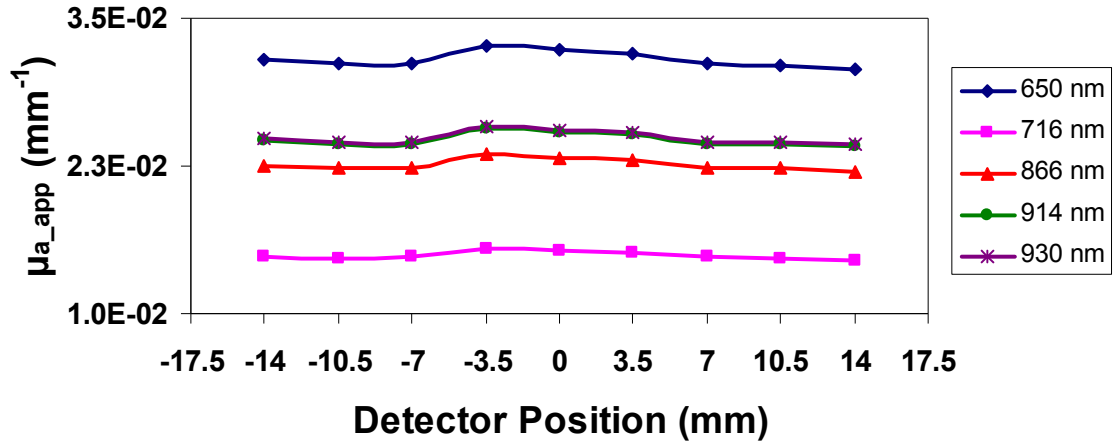


Figure 54: Plot of spectrally resolved arterial  $\mu_{a\_app}$  for fatty tissue containing two absorbing heterogeneities (artery and bile duct) adjacent to each other at depth of 8 mm. The reflectance contributions from all 13 sources were added to each detector and the fit used absolute reflectance data. Both the arterial and bile absorption coefficients were varied in each fit simultaneously.

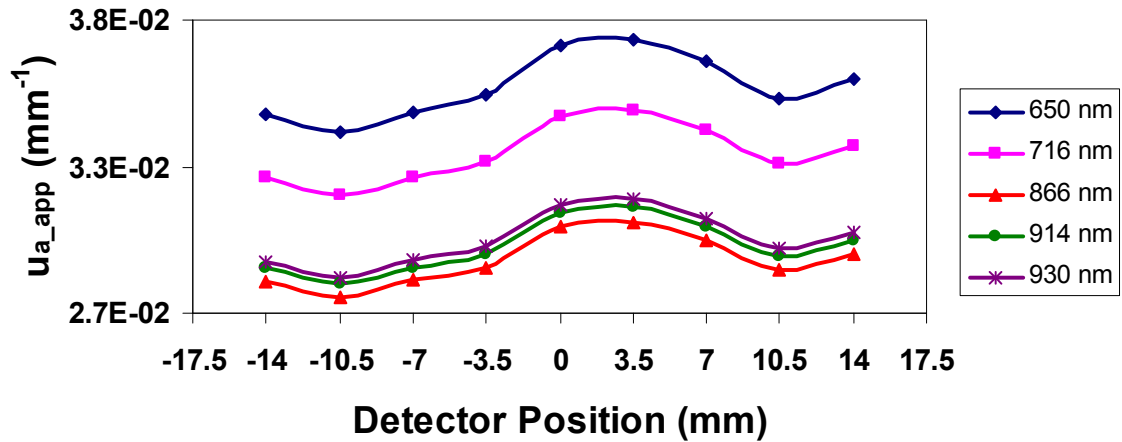


Figure 55: Plot of spectrally resolved bile  $\mu_{a\_app}$  for fatty tissue containing two absorbing heterogeneities (artery and bile duct) adjacent to each other at depth of 8 mm. The reflectance contributions from all 13 sources were added to each detector and the fit used absolute reflectance data. Both the arterial and bile absorption coefficients were varied in each fit simultaneously.

Figure 56 shows the variation of arterial  $\mu_{a\_app}$  for tissue containing two absorbing heterogeneities placed adjacent to each other at a depth of 4 mm, 6 mm, and 8 mm respectively in fatty tissue. For better comparison  $\mu_{a\_app}$  is plotted for a single wavelength (650 nm). The comparison shows that at a depth of 4 mm the point of maximum absorption has the highest value (5.19e-02), which decreases as depth increases. The  $\mu_{a\_app}$  at the point of maximum absorption for a depth of 6 mm has the value of 3.64e-02 (~43% decrease) and at depth of 8 mm it further reduces to 3.24e-02 (~60% decrease). From Figure 56 it can also be inferred that as the absorbing heterogeneity moves deeper the sensitivity of localization reduces. Sensitivity of localization at 4 mm is ~63% and goes down to ~15 % at 6 mm and to ~5.5% at 8 mm.

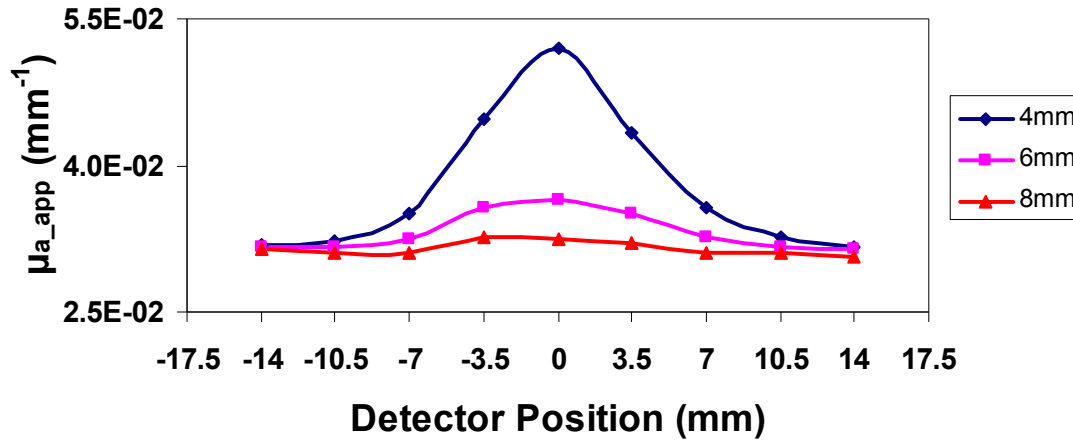


Figure 56: Comparison of arterial  $\mu_{a\_app}$  at 650 nm for tissue containing two absorbing heterogeneities (artery and bile duct) placed adjacent to each other at depths of 4 mm, 6 mm and 8 mm.

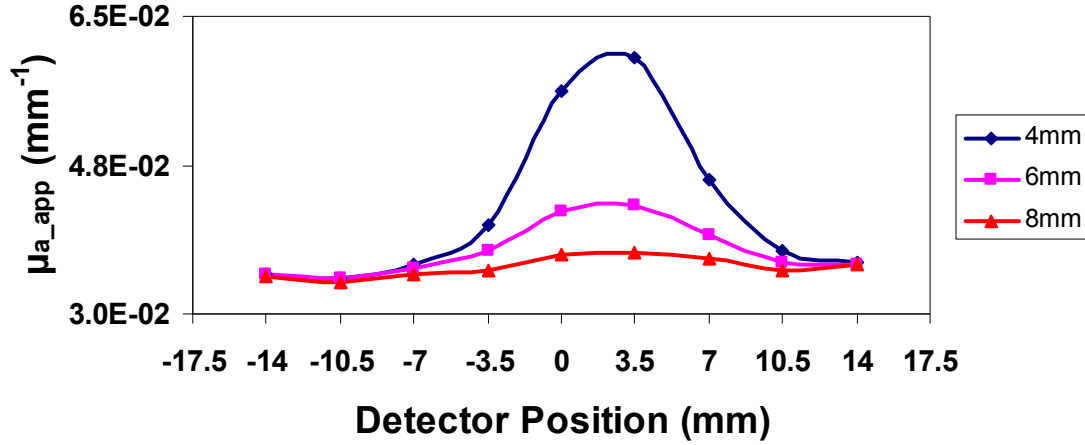


Figure 57: Comparison of bile  $\mu_{a\_app}$  at 650 nm for tissue containing two absorbing heterogeneities (artery and bile duct) placed adjacent to each other at depths of 4 mm, 6 mm and 8 mm.

Figure 57 shows the variation of bile  $\mu_{a\_app}$  for tissue containing two absorbing heterogeneities placed adjacent to each other at depth of 4 mm, 6 mm, and 8 mm respectively in fatty tissue. For better comparison  $\mu_{a\_app}$  is plotted for a single wavelength (650 nm). The comparison shows that at a depth of 4 mm the point of maximum absorption has the highest value 6.01e-02 and it decreases as depth increases. The  $\mu_{a\_app}$  at point of maximum absorption for depth of 6 mm has the value of 4.28e-02 (~40% decrease) and at depth of 8 mm it further reduces to 3.73e-02 (~61% decrease). From Figure 57 it can also be inferred that as absorbing heterogeneity moves deeper, the sensitivity of localization reduces. Sensitivity of localization at 4 mm is ~67%, it goes down to ~20 % at 6 mm and to ~5% at 8 mm.

### 3.3.2 Depth Localization

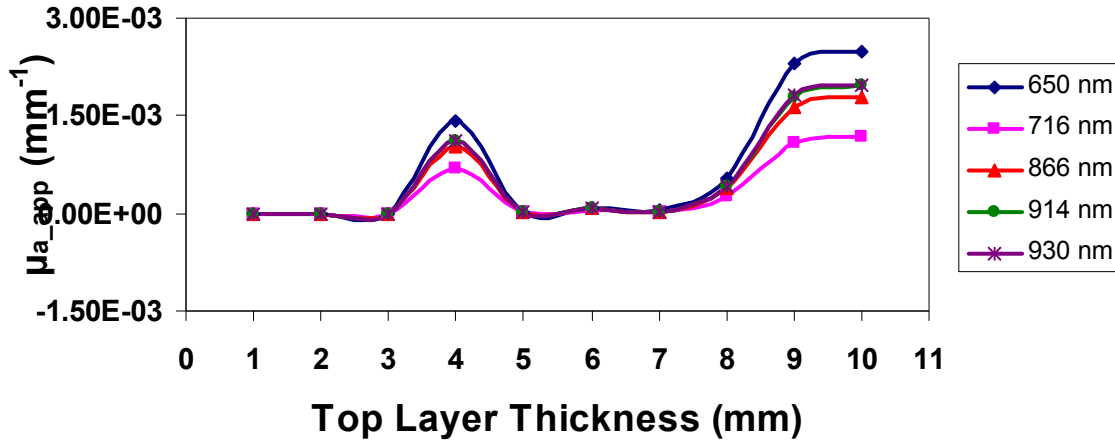


Figure 58: Depth-wise arterial  $\mu_{a\_app}$  for a detector placed on the peak absorption surface location. Tissue geometry consisted of two absorbing heterogeneities (artery and bile duct both centered at 4 mm depth, adjacent to each other); all sources were added to a single detector, reflectance data fitting was relative; only the arterial absorption of the top and bottom layers was varied in each fit.

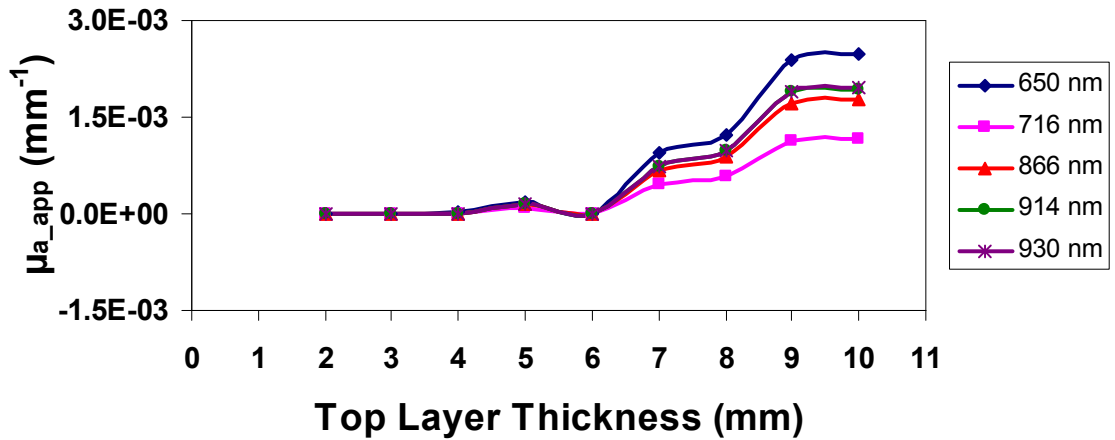


Figure 59: Depth-wise arterial  $\mu_{a\_app}$  for a detector placed on the peak absorption surface location. Tissue geometry consisted of two absorbing heterogeneities (artery and bile duct both centered at 6 mm depth, adjacent to each other); all sources were added to a single detector, reflectance data fitting was relative; only the arterial absorption of the top and bottom layers was varied in each fit.

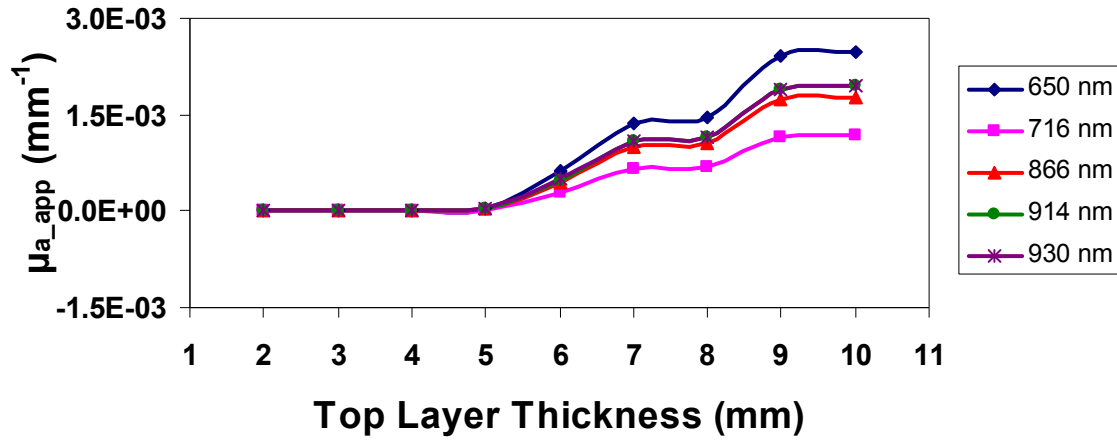


Figure 60: Depth-wise arterial  $\mu_{a\_app}$  for a detector placed on the peak absorption surface location. Tissue geometry consisted of two absorbing heterogeneities (artery and bile duct both centered at 8 mm depth, adjacent to each other); all sources were added to a single detector, reflectance data fitting was relative; only the arterial absorption of the top and bottom layers was varied in each fit.

Figures 58, 59, and 60 show the arterial  $\mu_{a\_app}$  for a detector placed on the peak absorption surface location. Tissue geometry consisted of two absorbing heterogeneities (artery and bile duct) placed adjacent to each other and both centered at 4 mm, 6 mm and 8 mm depth respectively. Comparison of depth-wise arterial  $\mu_{a\_app}$  (650 nm) for 4 mm, 6 mm, and 8 mm depths is shown in Figure 61. In the case where the absorbing heterogeneities were placed at 4 mm depth, the point of maximum absorption is observed at 4 mm. We also see the rise in  $\mu_{a\_app}$  at higher top layer thickness (7 mm - 10 mm). The rise in  $\mu_{a\_app}$  at higher top layer thickness can be attributed to the less amount of light reaching at that depth as majority of photons get absorbed at depth of 4 mm. When absorbing heterogeneities were placed at 6 mm and 8 mm depth, the point of maximum absorption is observed at 5 mm and 7 mm. There is rise in  $\mu_{a\_app}$  for top layer thickness of 7 mm onwards.



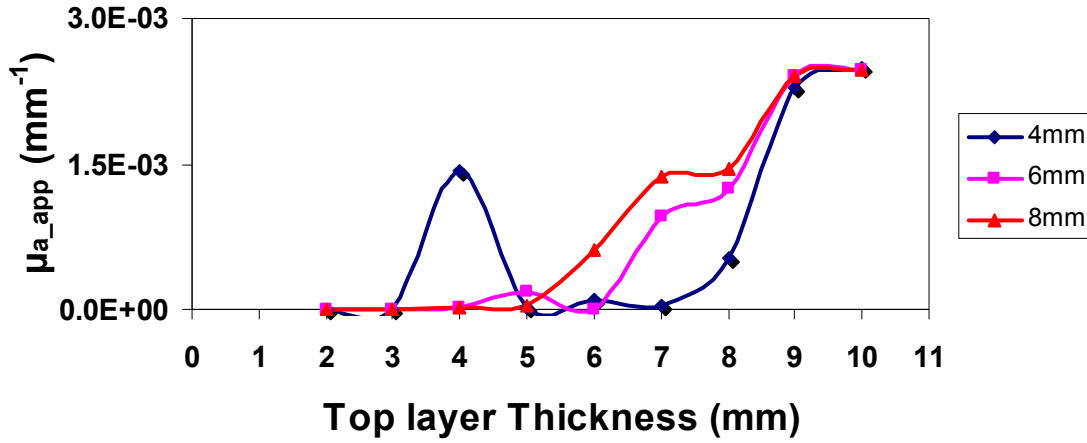


Figure 61: Comparison of depth-wise arterial  $\mu_{a\_app}$  of 650 nm for tissue containing two absorbing heterogeneities (artery and bile duct) placed adjacent to each other at depths of 4 mm, 6 mm and 8 mm.

### 3.4 Effect of Background Scattering Value Errors on Apparent Absorption

Figure 62 shows the arterial  $\mu_{a\_app}$  for tissue containing a single absorbing heterogeneity. The  $\mu_{a\_app}$  is plotted for  $\pm 25\%$  of background scattering. As seen from the Figure for  $-25\%$  of scattering the point of maximum absorption has the value of  $1.36\text{e-}01$ , for  $+25\%$  of scattering the point of maximum absorption has the value of  $5.47\text{e-}02$ . Though the change in  $\mu_{a\_app}$  was observed for change in scattering, the localization of absorbing heterogeneity was unaffected.

Figure 63 shows the depth-wise arterial  $\mu_{a\_app}$  for tissue containing a single absorbing heterogeneity. The  $\mu_{a\_app}$  is plotted for  $\pm 25\%$  of background scattering. As seen from the Figure for  $+25\%$  of scattering the point of maximum absorption has the value of  $6.09\text{e-}03$ . Though the change in  $\mu_{a\_app}$  was observed for change in scattering, the localization of absorbing heterogeneity was unaffected. In case of  $-25\%$  of scattering the

point of maximum absorption has the value of  $2.44 \times 10^{-3}$ . The change in  $\mu_{a\_app}$  was observed for change in scattering, also the localization of absorbing heterogeneity was affected by few mm.

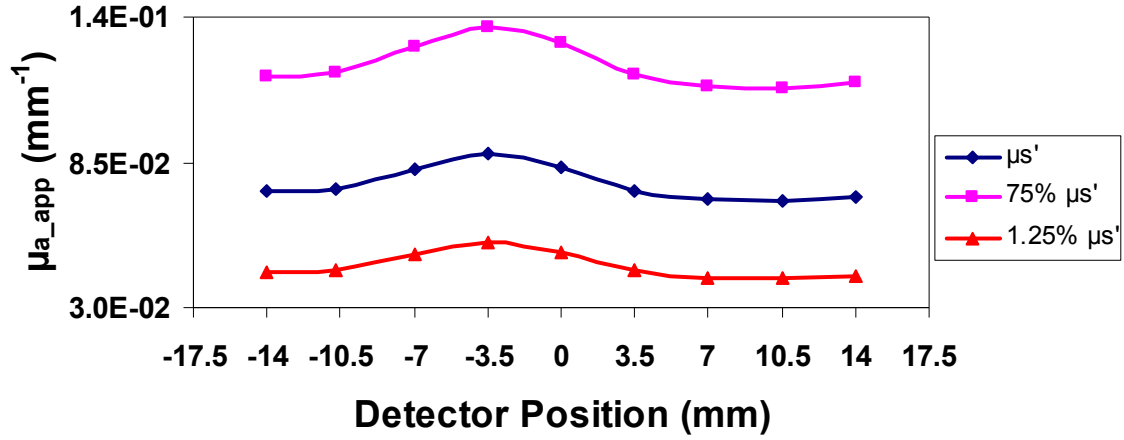


Figure 62: Plot of arterial  $\mu_{a\_app}$  comparing the effect of change in the background scattering coefficient on the apparent absorption of tissue containing a heterogeneity.

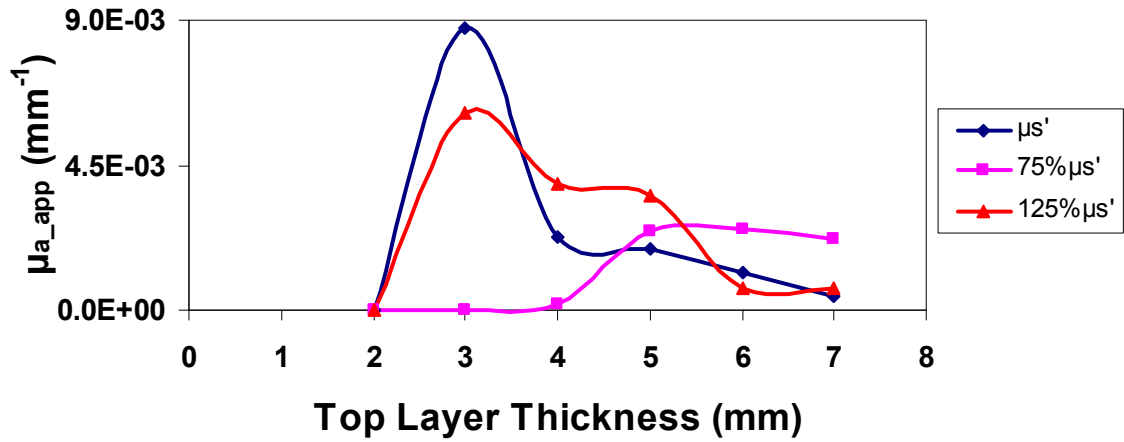


Figure 63: Plot of depth-wise arterial  $\mu_{a\_app}$  comparing the effect of change in the assumed background scattering coefficient on the apparent absorption of tissue containing a heterogeneity.

## CHAPTER 4

### DISCUSSION AND CONCLUSIONS

In this work five wavelengths spanning from red to NIR wavelengths (650-930 nm) were used to probe tissue. The method is easily applicable to any number of wavelengths but these were limited to five in this work due to the time-consuming nature of Monte Carlo simulations that were used to generate these simulated reflectance measurement data. In future experimental measurements on tissue-simulating phantoms and on humans we expect to be processing spectrally resolved reflectance data at a much larger number of wavelengths.

When the spectrally resolved MC data is input to inverse model, the fitting parameter output (apparent absorption,  $\mu_{a\_app}$ ) can be described as qualitative mirror image of the input reflectance data. The point of least reflectance becomes the point of maximum absorption. For the lateral localization (semi-infinite diffusion model) of absorbing heterogeneities, absolute fitting of the reflectance data gives higher  $\mu_{a\_app}$  than that for relative fitting. The lower apparent absorption translates to a loss of detection sensitivity; relative reflectance fitting introduces an extra degree of freedom in the fitting procedure (Figure 12), which makes the inverse problem less well-posed.

Moving a source-detector pair along the tissue surface localizes the heterogeneity with some spatial shift relative to its true location. This shift is due to the parabolic ('banana') shape of the photon density function, which projects the photon

absorption experienced by light injected into tissue from the source onto the detector (e.g. Figure 6b). As source-detector separation increases the point of maximum absorption shifts with detector location – one can approximately correct for that by assuming that the point of maximum absorption was at the source-detector separation midpoint.

Adding reflectance contributions from many sources to one detector and moving that detector along the tissue surface determines the true location of the heterogeneity. Adding reflectance contributions from many sources sum up parabolic (‘banana’) shape of the photon density function as making them a planer illumination. The planer illumination eliminates the shift which is due to the parabolic (‘banana’) shape of the photon density function and therefore it determines the true location of the absorbing heterogeneity. In this case the reduction in apparent absorption ( $\mu_{a\_app}$ ) is because of loss of detection sensitivity due to signal averaging from source detector separations that sample mostly background fat tissues.

When there are more than one heterogeneities within the tissue volume being probed, it is challenging to localize and identify them individually by visually inspecting the reflectance data. The multiple scattering smears the absorption profile of a single heterogeneity and creates a broad shadow at the surface. Therefore when two heterogeneities exist at close proximity their shadows overlap and it is difficult to identify them individually. Even though we cannot distinguish the two heterogeneities from direct observation of the spectrally resolved reflectance data, fitting of the latter to the semi-infinite medium model enables their individual identification. In one test example we could distinguish between two absorption heterogeneities separated by some distance (7

mm center-to-center) and fitting (absolute fit) the apparent absorption of each one simultaneously. We could localize two absorption heterogeneities that were exactly adjacent to each other (3 mm center-to-center) and fitting (absolute fit) for the apparent absorption of each one simultaneously.

When fitting (absolute fit) simultaneously for two heterogeneities a shift in artery location is observed because of fitting cross talk. In contrast, bile duct localization was not influenced by the presence of the artery.

By using a two-layer diffusion model to fit the spectrally resolved reflectance data at a detector position near the point of maximum absorption on the tissue surface, that location having being previously deduced for each heterogeneity type by the semi-infinite model, we can estimate the tissue depth for each one of these heterogeneities. Fitting of the two-layer model for a single detector directly above the artery or the bile duct, with all sources simultaneously contributing to that detector, could correctly estimate the true depth of each of these heterogeneities. In case of absorbing heterogeneities (bile duct) having less variation in their absorption spectrum for the selected range of wavelengths, it becomes challenging to determine their location depth-wise. As light propagates depth-wise in tissue, each wavelength gets attenuated differently at different depth. In case of flat spectrum (having similar attenuation), each wavelength gets attenuated equally at certain depth which makes detection of heterogeneity in depth difficult.

If the absorption heterogeneity is very close to the surface, i.e. less than approximately two mean free paths (2 mm), depth localization can be difficult as the diffusion approximation does not hold true for the top layer. This is of little practical

importance however, as at these superficial depths a surgeon could directly visualize these absorbing heterogeneities.

When fitting spectrally resolved reflectance data from a single source-detector pair for both relative and absolute fitting, the depth estimates are not as accurate as when contributions from several sources to a single detector are being considered.

Change in scattering ( $\pm 25\%$ ) does not affect the lateral localization of an absorbing heterogeneity but an increase in scattering decreases the apparent absorption and vice versa. Both increased and decreased background scattering ( $\pm 25\%$ ) affect the depth-wise localization of an absorbing heterogeneity by  $\sim 1$  mm.

In summary, we have proposed a non-invasive methodology based on the detection of near-infrared reflectance to address the clinically important problem of localizing the human biliary tree intraoperatively. This work describes how the proposed methods have been tested and validated in simulation and the next step is to further test them in the laboratory and in the operating theater. A successful clinical implementation of a biliary tree imaging system would reduce surgical time, improve patient safety, and minimize the risk of complications and expenses attributable to the current standard practice of intraoperative cholangiography. It is hoped that the work presented here will contribute towards the attainment of that important clinical goal.

APPENDIX A.  
THE LEVENBERG –MARQUARDT FITTING ALGORITHM

## A.The Levenberg –Marquardt Fitting Algorithm

Mrqmin.c

```
/* note #undef's at end of file */
#define NRANSI
#include "nrutil.h"

void mrqmin(float x[], float y[], float sig[], int ndata, float a[], int ia[],
            int ma, float **covar, float **alpha, float *chisq,
            void (*funcs)(float, float [], float *, float [], int), float *alamda)
{
    void covsrt(float **covar, int ma, int ia[], int mfit);
    void gaussj(float **a, int n, float **b, int m);
    void mrqcof(float x[], float y[], float sig[], int ndata, float a[],
                int ia[], int ma, float **alpha, float beta[], float *chisq,
                void (*funcs)(float, float [], float *, float [], int));
    int j,k,l;
    static int mfit;
    static float ochisq,*atry,*beta,*da,**oneda;

    if (*alamda < 0.0) {
        atry=vector(1,ma);
        beta=vector(1,ma);
        da=vector(1,ma);
        for (mfit=0;j=1;j<=ma;j++)
            if (ia[j]) mfit++;
        oneda=matrix(1,mfit,1,1);
        *alamda=0.001;
        mrqcof(x,y,sig,ndata,a,ia,ma,alpha,beta,chisq,funcs);
        ochisq=(*chisq);

        for (j=1;j<=ma;j++) atry[j]=a[j];
    }
    for (j=1;j<=mfit;j++) {
        for (k=1;k<=mfit;k++) covar[j][k]=alpha[j][k];
        covar[j][j]=alpha[j][j]*(1.0+(*alamda));
        oneda[j][1]=beta[j];
    }
    gaussj(covar,mfit,oneda,1);
}
```



```

for (j=1;j<=mfit;j++) da[j]=oneda[j][1];
if (*alamda == 0.0) {
    covsrt(covar,ma,ia,mfit);
    covsrt(alpha,ma,ia,mfit);
    free_matrix(oneda,1,mfit,1,1);
    free_vector(da,1,ma);
    free_vector(beta,1,ma);
    free_vector(atry,1,ma);
    return;
}
for (j=0,l=1;l<=ma;l++)
    if (ia[l]) atry[l]=a[l]+da[++j];
mrqcof(x,y,sig,ndata,atry,ia,ma,covar,da,chisq,funcs);

if (*chisq < ochisq) {
    *alamda *= 0.1;
    ochisq=(*chisq);
    for (j=1;j<=mfit;j++) {
        for (k=1;k<=mfit;k++) alpha[j][k]=covar[j][k];
        beta[j]=da[j];
    }
    for (l=1;l<=ma;l++) a[l]=atry[l];
} else {
    *alamda *= 10.0;
    *chisq=ochisq;
}
}
#endif NRANSI

```

### Mrqcof.c

```

/* note #undef's at end of file */
#define NRANSI
#include "nrutil.h"

void mrqcof(float x[], float y[], float sig[], int ndata, float a[], int ia[],
    int ma, float **alpha, float beta[], float *chisq,
    void (*funcs)(float, float [], float *, float [], int))
{
    int i,j,k,l,m,mfit=0;

```

```

float ymod,wt,sig2i,dy,*dyda;

dyda=vector(1,ma);
for (j=1;j<=ma;j++)
    if (ia[j]) mfit++;
for (j=1;j<=mfit;j++) {
    for (k=1;k<=j;k++) alpha[j][k]=0.0;
    beta[j]=0.0;
}
*chisq=0.0;
for (i=1;i<=ndata;i++) {
    (*funcs)(x[i],a,&ymod,dyda,ma);
    sig2i=1.0/(sig[i]*sig[i]);
    dy=y[i]-ymod;
    for (j=0,l=1;l<=ma;l++) {
        if (ia[l]) {
            wt=dyda[l]*sig2i;
            for (j++,k=0,m=1;m<=l;m++)
                if (ia[m]) alpha[j][++k] += wt*dyda[m];

            beta[j] += dy*wt;
        }
    }
    *chisq += dy*dy*sig2i;
}
for (j=2;j<=mfit;j++)
    for (k=1;k<=j;k++) alpha[k][j]=alpha[j][k];
free_vector(dyda,1,ma);
}
#undef NRANSI

```

## REFERENCES

- [1] [www.barcnetwork.org/i/biliarytract.png](http://www.barcnetwork.org/i/biliarytract.png).
- [2] [http://mse.mef.hr/msedb/slike/p06030101\\_1/dir388/pdf0.pdf](http://mse.mef.hr/msedb/slike/p06030101_1/dir388/pdf0.pdf).
- [3] R. S. B. Chamberlain, L. H., "Hepatobiliary surgery, CHAPTER 1 :Essential Hepatic and Biliary Anatomy for the Surgeon " p. 287, 2003.
- [4] E. H. Livingston, J. A. Miller, B. Coan, and R. V. Rege, "Costs and Utilization of Intraoperative Cholangiography," *J Gastrointest Surg*, Jun 30 2007.
- [5] L. W. Way, L. Stewart, W. Gantert, K. Liu, C. M. Lee, K. Whang, and J. G. Hunter, "Causes and prevention of laparoscopic bile duct injuries: analysis of 252 cases from a human factors and cognitive psychology perspective," *Ann Surg*, vol. 237, pp. 460-9, Apr 2003.
- [6] M. Shaun McKenzie, Richard Schwartz, MD, "The Management of Bile Duct Injuries Occurring During Laparoscopic Cholecystectomy," *Current Surgery*, vol. 63, pp. 20-23, 1/2006 2006.
- [7] A. Waage and M. Nilsson, "Iatrogenic bile duct injury: a population-based study of 152 776 cholecystectomies in the Swedish Inpatient Registry," *Arch Surg*, vol. 141, pp. 1207-13, Dec 2006.
- [8] J. F. Buell, D. C. Cronin, B. Funaki, A. Koffron, A. Yoshida, A. Lo, J. Leef, and J. M. Millis, "Devastating and fatal complications associated with combined vascular and bile duct injuries during cholecystectomy," *Arch Surg*, vol. 137, pp. 703-8; discussion 708-10, Jun 2002.
- [9] N. Gupta, H. Solomon, R. Fairchild, and D. L. Kaminski, "Management and outcome of patients with combined bile duct and hepatic artery injuries," *Arch Surg*, vol. 133, pp. 176-81, Feb 1998.
- [10] T. B. Hugh, "New strategies to prevent laparoscopic bile duct injury--surgeons can learn from pilots.," *Surgery*, vol. 132, pp. 826-35, May 25 2002.
- [11] D. R. Flum, E. P. Dellinger, A. Cheadle, L. Chan, and T. Koepsell, "Intraoperative cholangiography and risk of common bile duct injury during cholecystectomy," *Jama*, vol. 289, pp. 1639-44, Apr 2 2003.
- [12] A. Csendes, P. Burdiles, J. C. Diaz, F. Maluenda, O. Korn, E. Vallejo, and P. Csendes, "Prevalence of common bile duct stones according to the increasing number of risk factors present. A prospective study employing routinely intraoperative cholangiography in 477 cases," *Hepatogastroenterology*, vol. 45, pp. 1415-21, Sep-Oct 1998.
- [13] J. J. Jakimowicz, "Intraoperative ultrasonography in open and laparoscopic abdominal surgery: an overview," *Surg Endosc*, vol. 20 Suppl 2, pp. S425-35, Apr 2006.

- [14] T. Tomonaga, C. J. Filipi, A. Lowham, and T. Martinez, "Laparoscopic intracorporeal ultrasound cystic duct length measurement: a new technique to prevent common bile duct injuries," *Surg Endosc*, vol. 13, pp. 183-5, Feb 1999.
- [15] K. J. Zuzak, S. C. Naik, G. Alexandrakis, D. Hawkins, K. Behbehani, and E. H. Livingston, "Characterization of a near-infrared laparoscopic hyperspectral imaging system for minimally invasive surgery," *Analytical Chemistry*, vol. 79, pp. 4709-4715, Jun 15 2007.
- [16] B. P. Subhadra Srinivasan, Colin Carpenter, Shudong Jiang, Wendy Wells, Steven Poplack, Peter Kaufman, and Keith Paulsen,, "Developments in Quantitative Oxygen Saturation Imaging of Breast Tissue In-vivo using Multispectral Near-Infrared Tomography," *Antiox. & Redox Sig.*, vol. 9, pp. 1-14 2007.
- [17] S. Fantini, E. L. Heffer, V. E. Pera, A. Sassaroli, and N. Liu, "Spatial and spectral information in optical mammography," *Technology in Cancer Research & Treatment*, vol. 4, pp. 471-482, Oct 2005.
- [18] D. J. Maitland, J. T. Walsh, and J. B. Prystowsky, "Optical-Properties of Human Gallbladder Tissue and Bile," *Applied Optics*, vol. 32, pp. 586-591, Feb 1 1993.
- [19] G. Zonios and A. Dimou, "Modeling diffuse reflectance from semi-infinite turbid media: application to the study of skin optical properties," *Optics Express*, vol. 14, pp. 8661-8674, Sep 18 2006.
- [20] A. Kienle and T. Glanzmann, "In vivo determination of the optical properties of muscle with time-resolved reflectance using a layered model," *Phys Med Biol*, vol. 44, pp. 2689-702, Nov 1999.
- [21] S. R. Arridge, "Photon-Measurement Density-Functions .1. Analytical Forms," *Applied Optics*, vol. 34, pp. 7395-7409, Nov 1 1995.
- [22] G. Alexandrakis, D. R. Busch, G. W. Faris, and M. S. Patterson, "Determination of the optical properties of two-layer turbid media by use of a frequency-domain hybrid Monte Carlo diffusion model," *Applied Optics*, vol. 40, pp. 3810-3821, Aug 1 2001.
- [23] G. Alexandrakis, T. J. Farrell, and M. S. Patterson, "Accuracy of the diffusion approximation in determining the optical properties of a two-layer turbid medium," *Applied Optics*, vol. 37, pp. 7401-7409, Nov 1 1998.
- [24] W. F. Cheong, S. A. Prahl, and A. J. Welch, "A Review of the Optical-Properties of Biological Tissues," *Ieee Journal of Quantum Electronics*, vol. 26, pp. 2166-2185, Dec 1990.
- [25] P. S. A. h. o. o. e. s. i. h. O. M. L. Clinic).
- [26] G. Alexandrakis, F. R. Rannou, and A. F. Chatziioannou, "Tomographic bioluminescence imaging by use of a combined optical-PET (OPET) system: a computer simulation feasibility study," *Phys Med Biol*, vol. 50, pp. 4225-41, Sep 7 2005.

- [27] S. L. J. Lihong Wang, Liqiong Zheng, "MCML-Monte Carlo modeling of light transport in multi-layered tissues," *Computer Methods and Programs in Biomedicine*, vol. 47, pp. 131-146, 1995.
- [28] D. A. Boas, J. P. Culver, J. J. Stott, and A. K. Dunn, "Three dimensional Monte Carlo code for photon migration through complex heterogeneous media including the adult human head," *Optics Express*, vol. 10, pp. 159-170, Feb 11 2002.
- [29] M. K. S. A. Prahl, S. L. Jacques, A. J. Welch, "A Monte Carlo Model of Light Propagation in Tissue," *SPIE Institute Series*, vol. 1S pp. 102-111, 19195.
- [30] L. O. S. Richard C. Haskell, Tsong-Tseh Tsay, Ti-Chen Feng and Matthew S. McAdams, "Boundary conditions for the diffusion equation in radiative transfer," *Optical Society of America*, vol. 11, pp. 2727-2741, 1994.
- [31] A. Kienle, M. S. Patterson, N. Dognitz, R. Bays, G. Wagnieres, and H. van den Bergh, "Noninvasive determination of the optical properties of two-layered turbid media," *Applied Optics*, vol. 37, pp. 779-791, Feb 1 1998.
- [32] M. S. P. T.J.Farrell, and M. Essenpreis, "Influence of layered tissue architecture on estimates of tissue optical properties obtained from spatially resolved diffuse reflectometry," *Appl. Opt.* , vol. 37, pp. 1958-1972, 1998.
- [33] M. S. P. A. Kienle, N. Utke, R. Bays, G. Wagnieres, and H. Van Den Bergh, "Determination of the optical properties of two-layer turbid media " *Appl. Opt.* , vol. 37, pp. 779-791, 1998.
- [34] B. P. F. W. H. Press, S. A. Teukolsky, and W. T. Vetterling,, "Numerical Recipes - The art of scientific computing," *Cambridge U. Press, London*, 1990.
- [35] R. C. Alper Corlu, Turgut Durduran, Kijoon Lee, Martin Schweiger, Simon R. Arridge, Elizabeth M. C. Hillman, and Arjun G. Yodh, "Diffuse optical tomography with spectral constraints and wavelength optimization," *APPLIED OPTICS*, vol. 44, pp. 2082-2093, 10 April 2005 2005.

#### BIOGRAPHICAL INFORMATION

Dharmendra Nadkar was born on 25<sup>th</sup> June, 1982 in Raigad, Maharashtra, India. He completed his Bachelor of Engineering in Biomedical Engineering from Mumbai (Bombay) University, India in May 2004. He joined University of Texas at Arlington in Spring 2006 to pursue Masters of Science in Biomedical Engineering. His current research area is optical imaging.